Numerical prediction and characterization of shock-buffet in transport aircraft

Razvan M. Apetrei

Department of Mechanical Engineering
University of Sheffield

This dissertation is submitted for the degree of
Doctor of Philosophy

December 2019

To my parents, grandparents, and dear sister.

Atinge steaua de neatins si nu ii uita pe cei care au crezut in tine.
-Octavian Paler

Acknowledgements

I would like to express my deepest gratitude to my PhD advisors: Dr. Jose Luis Curiel-Sosa and Professor Ning Qin - for dedicating part of their precious time towards providing me with the guidance I needed.

I would like to show my appreciation to Dr.-Ing Vlad Ciobaca of German Aerospace Centre (DLR) who agreed on collaborating with me for part of this project and welcomed me in their company as a Guest Scientist.

I would also like to thank The University of Sheffield, an institution that sculpted my character, and provided me with financial support via a PhD scholarship.

I reached here thanks to the sacrifices and hard work of my parents, Aurelian and Maria Apetrei, who, ever since I was in my youths, encouraged my curiosity, provided the emotional and financial support, and stood by my decisions with pride.

Finally, I would like to sincerely thank to my loved ones, dear friends, and peers who contributed towards my morale, emotional support, and challenging debates.

Thank you!
Razvan Apetrei, 2019

Abstract

Computational Fluid Dynamics (CFD) simulations are frequently used in the aerospace industry to help reduce development times by cutting down on the need of extensive wind-tunnel campaigns. However, although design-point aerodynamics are well predicted, edge of the envelope scenarios dominated by non-linear fluid phenomena can lead to uncertainties in the accuracy of the results produced.

This work addresses the use of Reynolds-averaged Navier-Stokes (RANS) based simulations in the prediction of unsteady shock-buffet phenomenon. Three studies are conducted: a 2D validation study, a 3D validation study, and the pinnacle of this work which presents a novel shock-buffet prediction on an industrially-relevant aircraft configuration.

Two dimensional shock-buffet predictions are presented as a confirmation of previous available knowledge. The dependency on turbulence modelling approaches is evident, with new results showing that the full Reynolds Stress Model (RSM) is a more appropriate closure to the RANS equations than other typically used eddy-viscosity-based models. However, this implies additional computational costs (due to increased number of equations solved), and inherited challenges associated with solver stability.

RANS-based simulations are then applied to a 3D configuration: the NASA Common Research Model (CRM) wing-body test case. Complementary results to the AIAA CFD Drag Prediction Workshop are produced. Novel results, outside the Drag Prediction Workshop envelope, investigate the development and expansion of the shock-induced boundary layer separation on the NASA CRM wing, however the steady RANS approach fails to accurately predict this due to unsteady effects which are not accounted for.

Unsteady simulations in the shock-buffet regime of the wing-body NASA CRM are then presented as the main novel contribution of this work. The complexity of the phenomenon is revealed by unsteady shock oscillations coupled with shock-induced separation and vortex shedding. The presence of shock-buffet cells is detected and helps understand shock dynamics. A frequency analysis reveals the presence of multiple peak frequencies. A qualitative comparison with experimental observation show similarity in the physics produced. Finally, to further investigate the shock-buffet phenomenon, the effects of changing the Reynolds number are presented.

Through industrial relevance, the current work can lead to decision making in the development of the future generation of aircraft.

List of Publications

Journal articles:

Apetrei, R. M., Ciobaca, V., Curiel-Sosa, J. L., and Qin, N., "Unsteady Shock Front Waviness in Shock-Buffet of the Common Research Model", **under review**

Apetrei, R. M., Curiel-Sosa, J. L., and Qin, N., "Using the Reynolds Stress Model to Predict Shock-Induced Separation on Transport Aircraft", *Journal of Aircraft*, vol. 56, no. 2, 583-590, 2019

Conference Presentations:

Apetrei R. M., Ciobaca, V., Curiel-Sosa, J. L., and Qin, N., "Shock-Buffet prediction on a wing-body aircraft using URANS and a Second-Moment Closure", *DiPaRT Symposium*, Airbus, Bristol, UK, 2018

Apetrei R. M., Curiel-Sosa, J. L., and Qin, N., "Prediction of Transonic Buffeting using the SU2 Open-Source Code", *7th European Computational Fluid Dynamics Conference*, ECCOMAS, Glasgow, UK, 2018

Apetrei R. M., Curiel-Sosa, J. L., and Qin, N., "Prediction of Shock-Induced Boundary Layer Separation using the RSM", *DiPaRT Symposium*, Airbus, Bristol, UK, 2017

Table of contents

List of figures xv

List of tables xxiii

1 Introduction **1**

1.1 Problem statement 1

1.2 Objectives and proposed outcome 3

2 Background **5**

2.1 Transonic flight 5

2.2 Edge of the envelope scenarios 7

2.3 Shock wave/boundary layer interaction 9

2.4 The shock-buffet phenomenon 10

2.4.1 Early experiments on symmetrical aerofoils 11

2.4.2 Experiments on conventional and supercritical aerofoils 16

2.4.3 Experiments on 3D configurations 22

2.4.4 Numerical predictions of shock-buffet 28

2.4.5 3D numerical predictions of shock-buffet 34

2.5 Conclusions 37

3 Computational strategy 39

3.1 Introduction 39

3.2 Governing equations of fluid flow 40

3.3 The RANS problem 42

3.3.1 What are the RANS equations 42

3.3.2 Turbulence modelling as a solution to the RANS problem 43

3.3.3 The k-ω Shear Stress Transport turbulence model 44

3.3.4 Second-order closures: the full Reynolds Stress Model 45

3.4 Discretization approach 51

3.4.1 Finite Volume Method 51

3.5 Choice of Solvers 52

3.6 Hardware 52

4 Numerical prediction of 2D shock-buffet 53

4.1 Introduction 53

4.2 Numerical approach 54

4.2.1 Numerical grids 54

4.2.2 Solver 56

4.3 Results 58

4.3.1 Mesh sensitivity 58

4.3.2 Effect of turbulence modelling at $\alpha = 3.5°$ 60
4.3.3 Prediction of shock-buffet envelope at $M_\infty = 0.73$ and $Re_c = 3$ million 63
4.4 Conclusions 66

5 Off-design transonic aerodynamics of NASA CRM 69
5.1 The NASA CRM aircraft 69
5.2 Numerical approach 71
5.2.1 Numerical grids 73
5.2.2 Solver 76
5.2.3 Computational test matrix 78
5.3 Results 78
5.3.1 Verification and Validation 78
5.3.2 Turbulence model study 83
5.3.3 Development of shock-induced boundary-layer separation 88
5.4 Lessons learnt and conclusions 91

6 Characterisation of shock-buffet on NASA CRM 95
6.1 Numerical Approach 96
6.1.1 Geometry 96
6.1.2 Numerical grids 96
6.1.3 Solver 96
6.1.4 Computational test matrix 97
6.1.5 Numerical probing of unsteady pressure data 98

6.2 Results 100

6.2.1 Verification and validation 100

6.2.2 Prediction of shock-buffet at $Re_{mac} = 5$ million 103

6.2.3 Reynolds number effects on shock-buffet 116

6.3 Lessons learnt and conclusions 120

7 Conclusions 123

7.1 Performance of the RSM closures in 2D shock-buffet prediction 124

7.2 Prediction of design point aerodynamics and shock-induced separation on the NASA CRM wing-body aircraft 126

7.3 Characterisation of shock-buffet on the NASA CRM 128

7.4 Further work 129

7.5 General lessons learnt 130

References 133

List of figures

1.1 A sketch of a typical transport aircraft flight envelope with gradient from black to white showing the decrease in confidence in CFD results (reproduced from [1]) 2

1.2 Histogram of lift coefficient predictions at design point ($\alpha = 2.5°$) and off design ($\alpha = 4.0°$) from 6th AIAA Drag Prediction Workshop [2] 3

2.1 Evolution of maximum Mach number of transport aircraft 6

2.2 Visualisation of transonic aerodynamics past an aircraft wing 6

2.3 Sketch of a *V-n* flight envelope 7

2.4 U-2 Speed vs Altitude flight envelope from U-2 Flight Manual [6] 8

2.5 Types of shock wave/boundary layer interactions from Mundell and Mabey [7] 9

2.6 Types of shock wave oscillations observed by Tijdeman [9] 11

2.7 Experimental setup from [11] 12

2.8 Buffet envelope obtained in [11] 12

2.9 Buffet cycle visualised through shadowgraph pictures in [13] 13

2.10 Buffet cycle visualised through: a) position of shockwave and development of the separation zone; b) value of Mach number immediately upstream of the shock (reproduced from [14]) 14

2.11 First shock-buffet mechanism produced for a symmetrical circular arc airfoil in [17] 15

2.12 Fluctuation of C_P as a function of lift (Whitcomb) and Mach number (NACA0012) in relationship with shock wave position (dark regions) [18] 17

2.13 Relationship between pressure oscillation magnitude, shock oscillation magnitude, and trailing-edge pressure divergence on the Whitcomb supercritical aerofoil [18] 17

2.14 Buffet envelope comparison for two aerofoils of different thickness [20] . . 18

2.15 Acoustic wave propagation buffet mechanism proposed by Lee in [21] . . . 19

2.16 Pressure coefficient distributions obtained by Jacquin *et. al.* [23] 21

2.17 Velocity fields measured with LDV in [23] 21

2.18 Buffet-onset envelopes as predicted by the 6 indicators investigated in [28] . 23

2.19 Root strain gauges recorded at $M_\infty = 0.70$ and 0.85, and $Re_{mac} = 5.0$ million in [30] 24

2.20 Mean and RMS values of C_P as measured using fast-response pressure sensitive paint in [34] 26

2.21 Buffet-cells observed in [34] 27

2.22 Sketches of the two main modes of shock oscillations observed in the experiments of Sugioka *et. al.* [34] 27

2.23 Comparison of C_P on the upper side of the aerofoil. Numerical results are given by the solid line (C_{Pmean}) and shaded area (time-accurate C_P). Experimental mean and time-accurate values are given through symbols and error bars respectively 29

2.24 The free flight (a); and wind tunnel condition (b) grids and geometries used in [41] 30

2.25 The effect of wind tunnel walls on computed shock-buffet oscillation amplitude in [41]. "2D inf." - free flight; "2D conf." - top and bottom walls accounted for; "3D conf." - full 3D wind tunnel geometry 31

2.26 Velocity divergence fields computed by ZDES in [45] 32

2.27 Comparison of mean and RMS pressures observed in experiments of [23] and numerical studies of [37], [45], [41], [47], [51], [49], [50], and [52]. Figure compiled by the author using data readily available in the aforementioned publications. 33

2.28 Numerical Schlieren and Q-criterion isosurfaces computed in [53] 34

2.29 Effect of sweep angle on three-dimensionality of shock buffet observed via C_P contours and streamlines [35] 35

2.30 Effect of Aspect Ratio on fluctuation levels ($C_{P_{rms}}$) in shock-buffet regime [35] 36

2.31 Surface C_P contours and slices of instantaneous eddy-viscosity (μ_t) computed in [57] via URANS and DDES 37

4.1 The OAT15A aerofoil geometry 53

4.2 Fluid domain around the OAT15A aerofoil 54

4.3 L3 grid around OAT15A generated using Pointwise 55

4.4 Mesh sensitivity analysis on the computed time-accurate C_L of the OAT15A aerofoil at $M_\infty = 0.73$, $Re_c = 3$ million and $\alpha = 3.5°$ 58

4.5 Power spectral distributions of the C_L signals computed on the 3 grids . . . 59

4.6 Last 0.1 seconds of computed C_L by using the three turbulence models on the L3 grid 60

4.7 Comparison between computed (with Linear Pressure-Strain RSM) and experimental C_P at $M_\infty = 0.73$, $Re_c = 3$ million, and $\alpha = 3.5°$ 61

4.8 Comparison between computed (with Stress-Omega RSM) and experimental C_P at $M_\infty = 0.73$, $Re_c = 3$ million, and $\alpha = 3.5°$ 62

4.9 Comparison between computed and experimental PSD of C_P at x/c = 0.45. Freestream $M_\infty = 0.73$, $Re_c = 3$ million, and $\alpha = 3.5°$ 63

4.10 Comparison between Experimental and Linear Pressure-Strain (LPS) RSM computed pressure on the OAT15A at various incidences 64

4.11 Comparison between Experimental and Stress-Omega (SO) RSM computed pressure on the OAT15A at various incidences 65

5.1 The full NASA CRM configuration:wing-body, nacelle-pylon andhorizontal tail 70

5.2 The 2D wing sections of the CRM at different spanwise locations 70

5.3 Measured wing tip deflection (ω_{tip}) and twist (ε_{tip}) in the ETW wind tunnel [85] 72

5.4 Effect of wing deformation on the original NASA CRM 72

5.5 Fluid domain around the NASA CRM 74

5.6 Example of grid types around a square geometry 74

5.7 Blocking structure in ICEM CFD 75

5.8 Surface element distribution on the medium grid 76

5.9 Residuals 79

5.10 Process of determining the α at which $C_L = 0.5$ in the grid sensitivity study 80

5.11 Grid sensitivity evaluated through: a) C_D, b) C_{D-PR}, and c) C_{D-V} at $C_L = 0.5$ 81

5.12 Grid sensitivity evaluated through C_M, and α at $C_L = 0.5$ 81

5.13 Pressure coefficient slices at $C_L = 0.5$ 82

5.14 Pressure coefficient slices at $C_L = 0.5$ 83

5.15 Aerodynamic coefficients obtained with the two turbulence models 84

5.16 Increase in the SOB as computed using the SST turbulence model. Isosurfaces of negative u shown in red. 85

5.17 C_P contours at different incidences 86

5.18 Zoom in view of C_P contours at $\alpha = 2.5 - 3.5°$, to highlight the shock-induced separation present in the SST results 86

5.19 C_P distributions as computed by *SST* and *RSM* at α=3.5° 87

5.20 C_P distributions as computed by *SST* and *RSM* at α=4.0° 88

5.21 Aerodynamic coefficients obtained with the two turbulence models 89

5.22 Computed C_P distributions at α = 4.5 - 6.0° and comparison with experimental data 91

5.23 Development of shock-induced separation visualised through shearlines and isosurfaces of negative streamwise velocity, u 92

6.1 Location of numerical surface probes where unsteady pressures are sampled based on location of unsteady pressure transducers in the experiments of: NASA (●); JAXA (●); and additional ones (●). The shaded gray area shows the location where shock-induced separation occurred in experiments . . . 99

6.2 Example analysis of unsteady C_P signals, data recorded for $M_\infty = 0.85$, $Re_{mac} = 5$ million, and $\alpha = 6.5°$ 100

6.3 Monitoring the residuals to determine the numerical accuracy of the simulations 101

6.4 Comparison of computed C_P at 6 η locations with experimental data from NASA AMES 102

6.5 The effect of Δt on the surface C_P signals 103

6.6 Evolution of NASA CRM C_L with incidence at $M_\infty = 0.85$, $Re_{mac} = 5$ million 104

6.7 Evolution of NASA CRM C_M with incidence at $M_\infty = 0.85$, $Re_{mac} = 5$ million 105

6.8 Evolution of NASA CRM C_M with incidence at $M_\infty = 0.85$, $Re_{mac} = 5$ million 106

6.9 Surface C_P response at η = 0.6, and various incidences 108

6.10 Surface C_P response at η = 0.6, and various incidences 109

6.11 Comparison between computed C'_{Prms} and an early epxerimental observation 109

6.12 Time-accurate computed surface C_P at M = 0.85, Re_{mac} = 5m, α = 6.0 ° . . 111

6.13 Computed buffet cells ($C'_P = C_P - C_{Pmean}$) at M = 0.85, Re_{mac} = 5m, α = 6.0 ° 112

6.14 Computed time-accurate and mean C_P at M = 0.85, Re_{mac} = 5m, α = 6.0° in comparison with mean experimental values from [88] 113

6.15 Computed isosurface of $M_{normal} = 1$ shock detection criterion coloured by Mach number magnitude, freestream conditions of M = 0.85, Re_{mac} = 5m, α = 6.0° 114

6.16 Spanwise slices of the shock isosurface at two points in time 115

6.17 Isosurfaces of $Q = 10,000$ coloured by M. Computed for $M = 0.85$, $Re_{mac} =$ 5 million and $\alpha = 6°$; $t = 1.2$s 116

6.18 Evolution of NASA CRM C_L with change in Re_{mac} at $M_\infty = 0.85$ and $\alpha = 6°$ 117

6.19 Reynolds number effect on computed mean C_P 118

6.20 Reynolds number effect on computed C'_{Prms} 118

6.21 Position of shock-front at different Re 119

6.22 Reynolds number effect on buffet frequency 120

7.1 The OAT15A aerofoil geometry 124

7.2 Comparison of current predictions, literature numerical predictions and experimental pressure coefficients on the OAT15A aerofoil at $M_\infty = 0.73$, $Re_c = 3$ million, and $\alpha = 3.5°$. 125

7.3 The NASA CRM aircraft configuration: WBNPT 126

7.4 Computed instantaneous flow field around the NASA CRM during shock-buffet. The surface contours give pressure coefficient; volume slices show density gradient values to highlight shock and boundary layer separation locations 129

List of tables

2.1 Comparison of results obtained for the OAT15A in shock-buffet regime . . 33

3.1 Values of the coefficients in the SSG and LLR models that are used in the SSG/LRR pressure-strain term; $C_2^{(LRR)} = 0.52$ 48

3.2 Values for the coefficients in the g transport equation. 50

4.1 Characteristics of the three grids generated for the OAT15A aerofoil 55

4.2 Computed C_L statistics across all three grids, results obtained by closing the URANS equations with the Linear Pressure-Strain RSM 59

4.3 Comparison between current, literature computed, and experimental fluctuation characteristics at different incidences. 65

5.1 The dimensions of the NASA CRM wing 71

5.2 Mesh generation guidelines provided by the AIAA CFD DPW organising committee 73

5.3 Characteristics of the three grids generated for this study 77

5.4 Computational run matrix 78

6.1 Computational run matrix shock-buffet 98

Chapter 1

Introduction

> "No one trusts a model except the man who wrote it; everyone trusts an observation, except the man who made it."
>
> - Harlow Shapley

1.1 Problem statement

Technological advancements resulted in an increased number of numerical methods and tools which can be used for aircraft design. In particular, the flexibility of high fidelity Computational Fluid Dynamics (CFD) is slowly replacing the need for extensive wind-tunnel testing, thus reducing cost and time during the development cycle. Nowadays, Reynolds-averaged Navier-Stokes (RANS) based simulations are significantly used in industry [1], and are known to produce accurate representations of aircraft aerodynamics at cruise design point.

Figure 1.1 is a sketch of a load vs. speed (n-V) envelope within which a transport aircraft is certified to sustain safe flight. The cruise point (yellow star) coincides with the design point of aircraft and gives the reference flight conditions at which the aircraft is optimised for maximum aerodynamic efficiency. Towards the *edges of the envelope* (or off-design flight conditions), fluid phenomena characterised by boundary layer separation and/or presence of shock waves are highlighted. For example, in a high speed/low load factor combination (*dive*) boundary layer separation on the lower surface of the wing might develop due to negative angles of attack. The gradient from black to white in Fig. 1.1 indicates that reliability in CFD results decreases as we move far away from the cruise point flight condition. The example below will provide an argument towards the questionable accuracy of RANS-based simulations in flight regimes dominated by shock-induced separation.

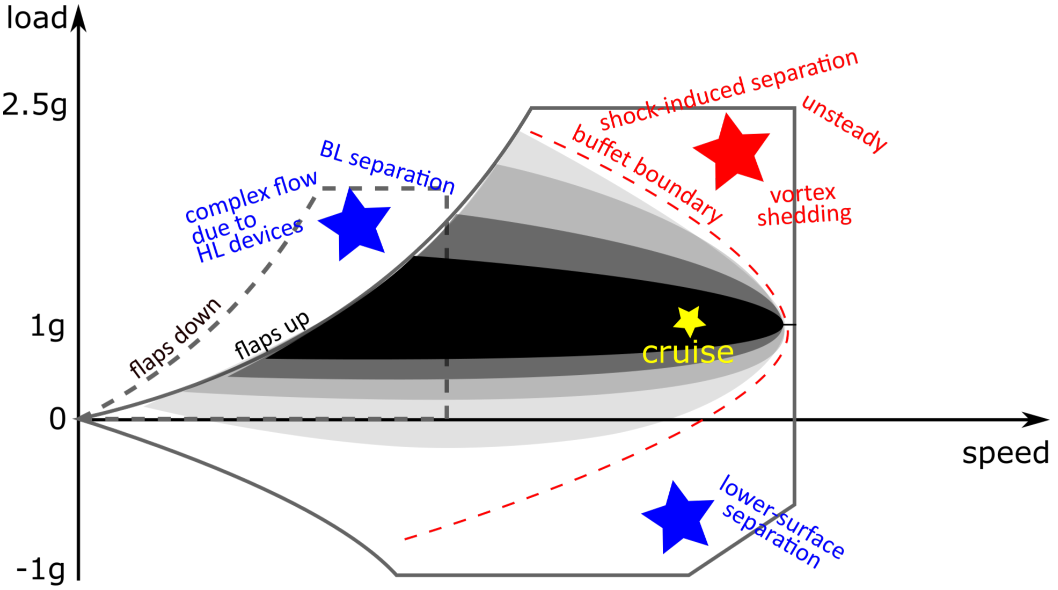

Fig. 1.1 A sketch of a typical transport aircraft flight envelope with gradient from black to white showing the decrease in confidence in CFD results (reproduced from [1])

The phenomena exemplified are difficult to be accurately predicted by RANS-based simulations. An argument is brought in Fig. 1.2, which summarises the participant data from the 6^{th} AIAA CFD Drag Prediction Workshop[1] (AIAA CFD DPW). The computed lift coefficients, C_L, of a representative aircraft configuration, by various RANS-based methodologies, are given. Design point ($\alpha = 2.5°$) predictions of C_L are clustered, with $2/3$ of participants' predictions being within $\Delta C_L = 0.02$; note that 0.01 in C_L is representative and typically called a *lift count*. In comparison, off design flight ($\alpha = 4.0°$, coincident with presence of shock-induced separation) predictions show a larger data spread and a significant number of outliers. This is due to poorly predicted non-linear flow interactions. In particular, RANS simulations closed with linear eddy-viscosity based turbulence models fail to robustly and accurately predict the flow field around an aircraft configuration in such flight scenarios.

---

[1] AIAA CFD DPW website: https://aiaa-dpw.larc.nasa.gov/

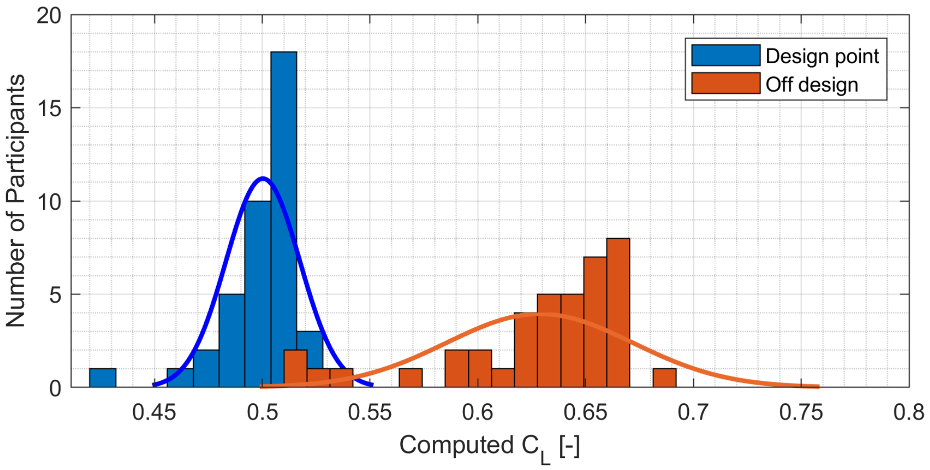

Fig. 1.2 Histogram of lift coefficient predictions at design point ($\alpha = 2.5°$) and off design ($\alpha = 4.0°$) from 6th AIAA Drag Prediction Workshop [2]

1.2 Objectives and proposed outcome

The purpose of this PhD research project is therefore to assess the ability to predict off-design flight aerodynamics by means of a special type of RANS-based CFD simulations. In particular, this research project will compare predictions obtained with a *second-order moment* closure with experimental and other numerical results. The second-order moment closures, also known as the full *Reynolds Stress Model* (RSM) are an advanced turbulence closure class which do not suffer from the linear nature of eddy-viscosity based closures.

To narrow down the problem, high Mach & high incidence flight scenarios (top right-hand corner in Fig. 1.1) are considered, where complex shock wave boundary layer interactions shock-induced separation and/or shock-buffet. The objectives are the following:

1. To develop an appreciation of the knowledge already available with regards to transonic aerodynamics and shock-buffet.
2. To assess the ability to predict edge-of-the-envelope aircraft aerodynamics by means of steady / unsteady RANS closed with eddy-viscosity and second order turbulence closures.
3. To produce industrially relevant observations with regards to possible approaches for shock-buffet prediction

The outcome of this project should then provide guidelines in favour/against applying RANS-based simulations for shock-buffet prediction.

This manuscript is structured to present the reader with a story. Chapter 2 contains a comprehensive description of the shock-buffet phenomenon, along with any relevant experimental and numerical efforts that have been already been made. All numerical aspects of this project will be described in Chapter 3, to avoid excessive use of equations and symbols in the results/discussion chapters. From Chapter 4 onwards, three test cases are presented: a 2D shock-buffet prediction (Chapter 4), followed by an extension to the 6^{th} AIAA CFD DPW (Chapter 5), and finally novel computed predictions of 3D shock-buffet (Chapter 6). Lessons learnt and conclusions are presented at the end of each chapter, as well as the end of this manuscript, in Chapter 7.

Chapter 2

Background

The goal of this research project is to verify the ability to produce numerical predictions of the shock-buffet phenomenon present in transport aircraft by means of industrially relevant Computational Fluid Dynamics (CFD) simulations. This chapter introduces the reader to shock-buffet and presents a comprehensive review of published literature.

To facilitate the understanding of shock-buffet, the concepts of *transonic flight, edge of envelope scenarios*, and types of *shock wave/boundary layer interactions* are presented first. The following sections give a thorough survey of early and recent experimental observations to reveal shock-buffet dynamics, dependence on geometry, and sensitivity to freestream parameters. The last part of this chapter contains a selection of efforts made to produce numerical predictions of shock-buffet.

2.1 Transonic flight

The *transonic flight* regime of modern aircraft is characterised by flight at a subsonic freestream Mach number, M_∞, during which, simultaneous subsonic and supersonic air-flow is present in the immediate vicinity of the aircraft's structure. Typically, the transonic flight occurs within the range $0.6 < M_\infty < 1.2$, the exact value of M_{crit} at which it is first present being particular to each geometry [3]. Since, flying at transonic M_∞ is known to be the most efficient way of travel for long range flights, the majority of modern aircraft have their design point (cruise) within this range (see Fig.2.1) [4].

Supersonic flow is present in transonic flight at $M_\infty > M_{crit}$ when air molecules, displaced by the aircraft structure, are carried over and accelerated to velocities higher than the local speed of sound. Most prominent, supersonic flow pockets develop on the upper surface of the wing (also referred to *suction* side). The supersonic flow pockets terminate in shock waves across which air is decelerated back to subsonic M. If the shock strength, measured through the amount of deceleration across the shock, is substantial, complex shock wave/boundary layer interactions (SWBLI) can result in *shock-induced separation, shock-buffet,* or complete *stall* of the aircraft. Figure 2.2 is a sketched visualisation of key flow features present in transonic flight with emphasis on the supersonic pocket of air present on aircraft wings.

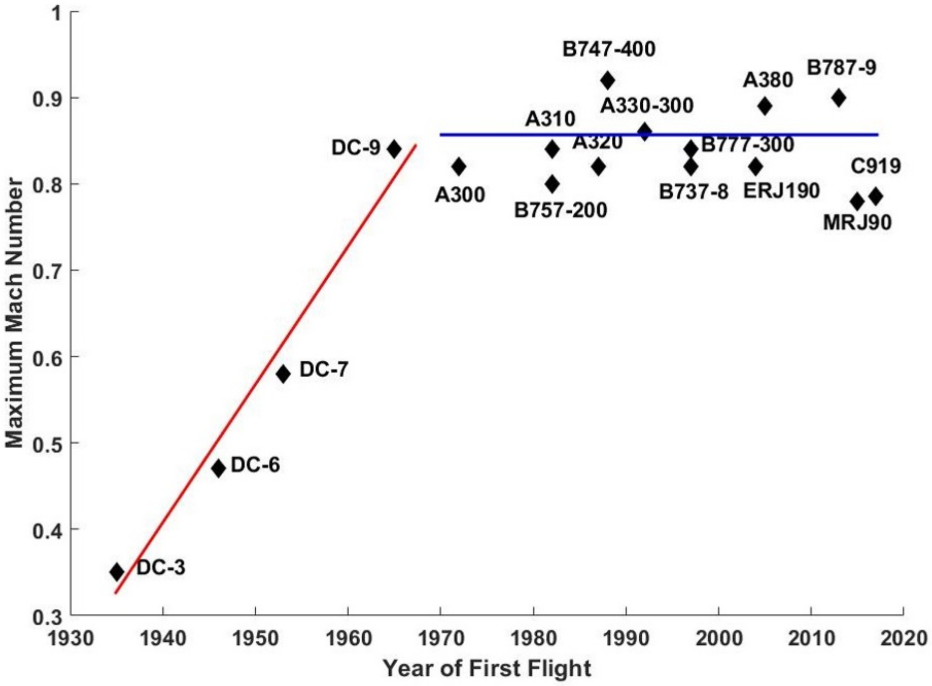

Fig. 2.1 Evolution of maximum Mach number of transport aircraft

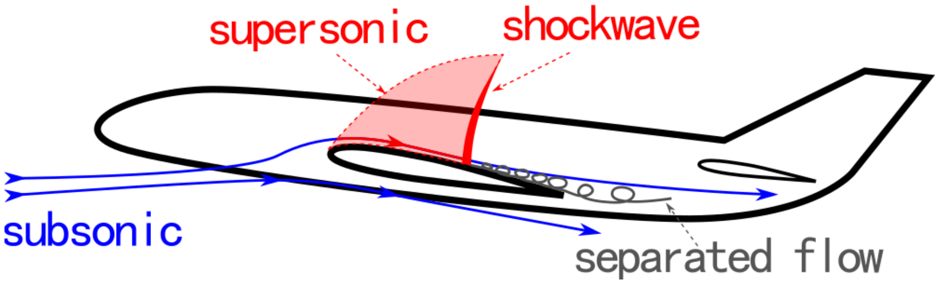

Fig. 2.2 Visualisation of transonic aerodynamics past an aircraft wing

2.2 Edge of the envelope scenarios

A flight envelope contains information with regards to the operating conditions in which the aircraft is designed to fly safely. A sketch of a typical *V-n* (velocity - load factor) flight envelope is given in Fig. 2.3. It highlights the combinations of speed and load factors $n = load/weight$ under which the aircraft is designed to sustain safe flight (inside green and blue contours). The design point is highlighted at $n = 1$ and $V = V_C$.

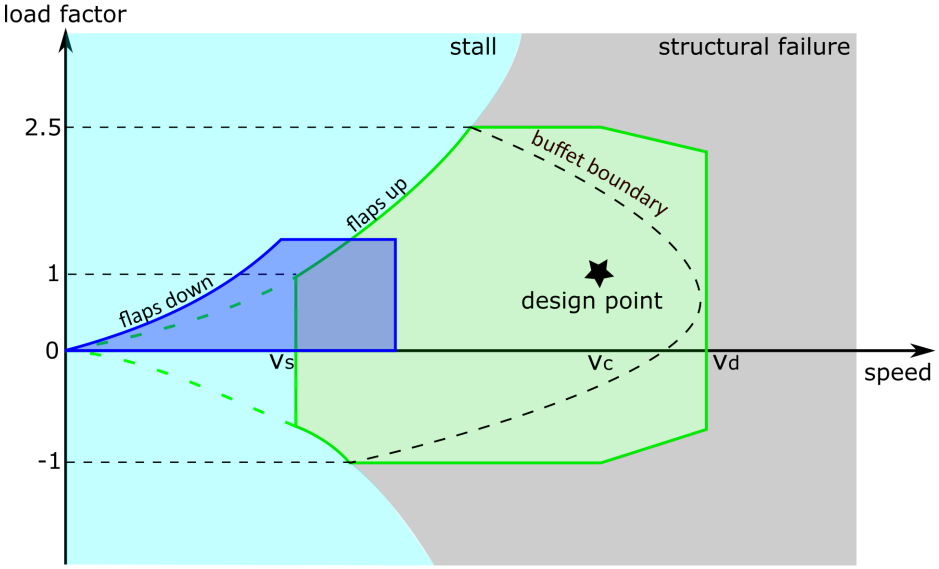

Fig. 2.3 Sketch of a *V-n* flight envelope

As per EASA's CS 25.251 paragraph (a): *"The aeroplane must be demonstrated in flight to be free from any vibration and buffeting that would prevent continued safe flight in any likely operating condition"* [5]. As a result, manufacturers must prove compliance by testing their aircraft. Shock-buffet onset limits may be within the safe operation margins as long as a $\Delta n = 0.3$ from cruise point to shock-buffet onset at maximum altitude, and safe flight within the manoeuvring envelope are demonstrated.

The potential scenarios outside of the flight envelope are shown in Fig. 2.3: stall of the aircraft or structural failure. The V-n flight envelope presented in Fig. 2.3 is an example, many other flight envelopes are made available to pilots. An extreme example is the $altitude - V$ flight envelope of the U-2 bomber which prescribes the velocity profile pilots should follow when ascending to altitude. Figure 2.4 shows that, starting with 65,000 feet altitude, the margins within which the aircraft can safely fly become as narrow as 5 knots, with a limit of 4 knots penetration into shock-buffet is allowed before safe flight cannot be sustained any longer. As mentioned, the U-2 bomber is an extreme example of a narrow buffet envelope. With regards to civil aircraft, manufacturers are unlikely to publish such flight envelopes and the reader is advised to consider the EASA certification standards given above.

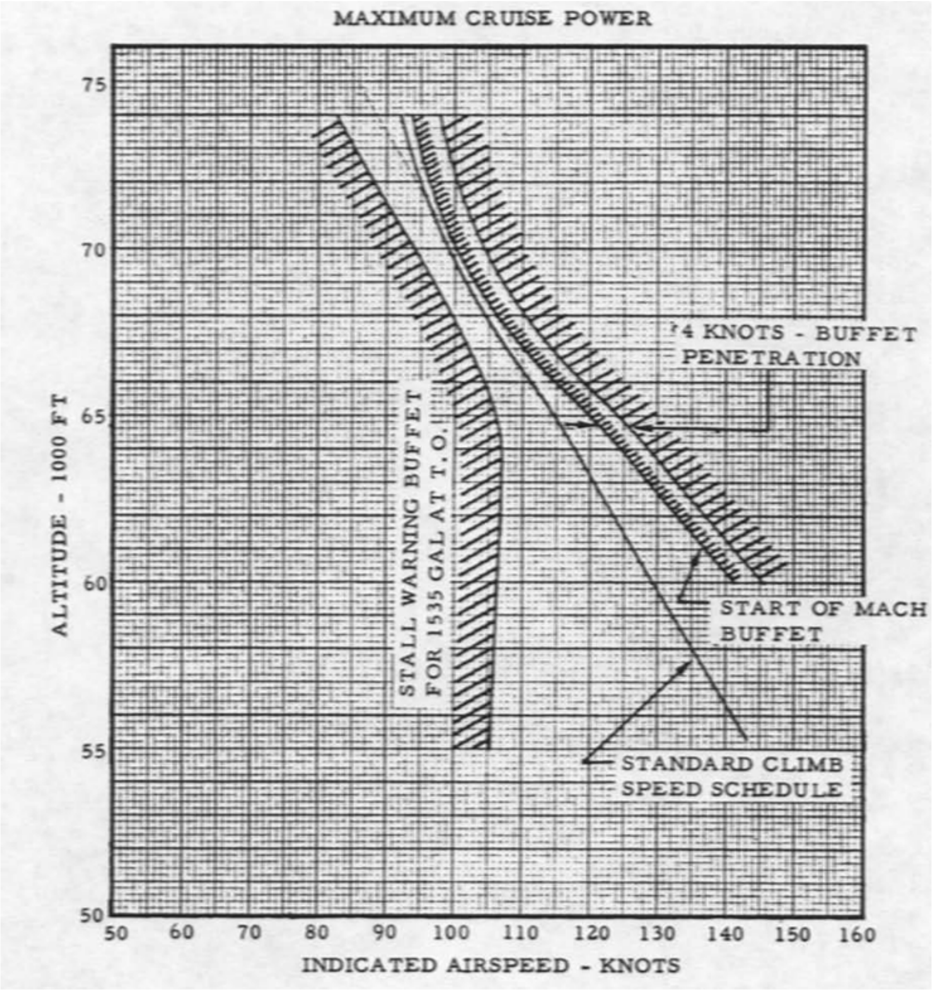

Fig. 2.4 U-2 Speed vs Altitude flight envelope from U-2 Flight Manual [6]

We can then define an edge of the envelope scenario as a flight condition close to the margins within which the aircraft was designed to sustain safe flight. Shock-buffet is one such flight condition. The aircraft is likely to be flying either at high velocity close to V_D (never exceed speed), or high n values.

2.3 Shock wave/boundary layer interaction

The presence of the shock wave in the transonic flight regime gives birth to complex SWBLI. Three types of SWBLI, displayed in Fig. 2.5 were found to occur by Mundell and Mabey [7].

Type 1 SWBLI (Fig. 2.5a) is characterised by a weak shock across which the boundary layer is facing adverse pressure gradients. It results in a thickening of the boundary layer downstream of the shock and no separation is present. Mundell and Mabey collected unsteady pressure data to characterise any type of unsteadiness present in the flow. For type 1 SWBLI only small fluctuations are present at the foot of the shock (location 2), the pressure remaining more or less constant upstream of the shock and in the thickened boundary layer.

With increase in M, α or both, the shock present in transonic flow becomes stronger. Shock-induced separation can appear at the foot of the shock (and/or at the trailing edge of the wing according to Pearcey *et. al.* [8]). This coincides with a type 2 SWBLI (Fig. 2.5b).Mundell and Mabey meausured low frequency fluctuations near the shock (location 2) and high frequency fluctuations in the separation bubble (location 3).

Total shock-induced boundary layer separation can arise from a further increase in M and/or α due to very strong shocks, resulting in type 3 SWBLI (Fig. 2.5c). This SWBLI regime was characterised by Mundell and Mabey as being unsteady with high amplitude, low frequency fluctuations being measured in the separated boundary layer (location 2). Some high frequency fluctuations can be present near the trailing-edge (location 2A).

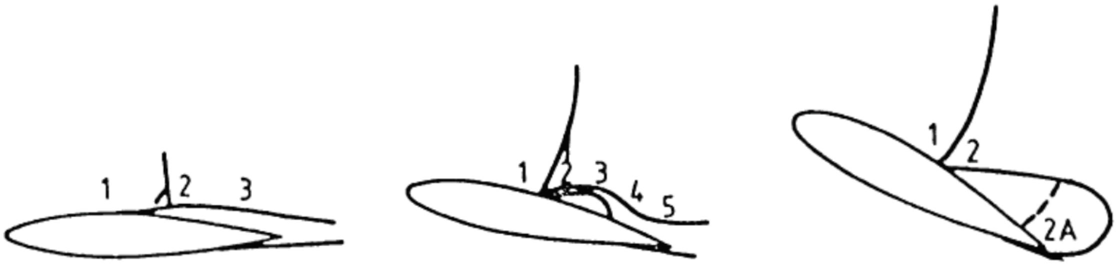

(a) Type 1 (weak shock) **(b)** Type 2 (stronger shock) **(c)** Type 3 (very strong shock)

Fig. 2.5 Types of shock wave/boundary layer interactions from Mundell and Mabey [7]

2.4 The shock-buffet phenomenon

The shock-buffet phenomenon is the result of unsteady SWBLI (type 3 in Fig. 2.5c) and is characterized by self-sustained, periodic, shock oscillations present in the off-design transonic flight regimes of aircraft. The onset of the phenomenon is likely to be in geometry-specific combinations of M, α and lift coefficient (C_L). The oscillation can be of single or multiple frequencies, typically within the range of non-dimensional Strouhal numbers, $St = fc/U_\infty = 0.1 - 0.6$, where f is the frequency in Hz, c is the mean aerodynamic chord (MAC), and U_∞ is the freestream velocity in m/s. In a shock-buffet cycle the shock can travel a significant distance and the dynamics of SWBLI may be accompanied by boundary layer separation/attachment.

Onset M_{onset} and α_{onset} ($C_{L,onset}$) can be within the flight envelope of aircraft as authorities only require a safety margin from cruise point (see Section 2.2). Although shock-buffet is a purely aerodynamic phenomenon, it can lead to structural vibration (buffeting) - affecting the comfort of the passengers and the structural integrity of the aircraft. As a phenomenon it is important for manufacturers from two perspectives. First, the onset must be well predicted to produce evidence that it is far away from the design point to comply with regulations. Secondly, characterisation past onset should be produced to identify the limits past which shock-buffet can impact the integrity of an aircraft during flight.

Three types of shock oscillations are known to occur during shock-buffet. They are similar to the types A, B and C of shock oscillations observed by Tijdeman on an aerofoil with a trailing edge flap. Tijdeman [9] produced experiments of a NACA 64A006 aerofoil equipped with an oscillating trailing-edge flap at various transonic M_∞. The frequency of the flap oscillation was in the range of typical buffet frequencies, the amplitude was maintained at 1° around the non-deflected position. Tijdeman's experiments revealed three types of shock-oscillations which can be visualised in Fig. 2.6.

- *Type A*, found at $M_\infty = 0.9$, is characterised by an almost sinusoidal shock-oscillation. Upper and lower-surface shocks oscillate in anti-phase. In addition, there was a phase shift between flap deflection and shock oscillations. The shock was found to be strongest while moving upstream and weakest whilst moving downstream.
- *Type B* was found at $M_\infty = 0.875$ and occurred in phase with the flap deflection. The shock motion was an interrupted sinusoidal. Just after reaching the most upstream loca-

tion, the shock broke down into wavelets before reappearing at the furthest downstream position.

- *Type C* shock motion occurred at $M_\infty = 0.85$. Wavelets appeared when the flap was deflected the most downward. They coalesced into one shock which then moved upstream past the leading-edge of the aerofoil then the cycle repeated.

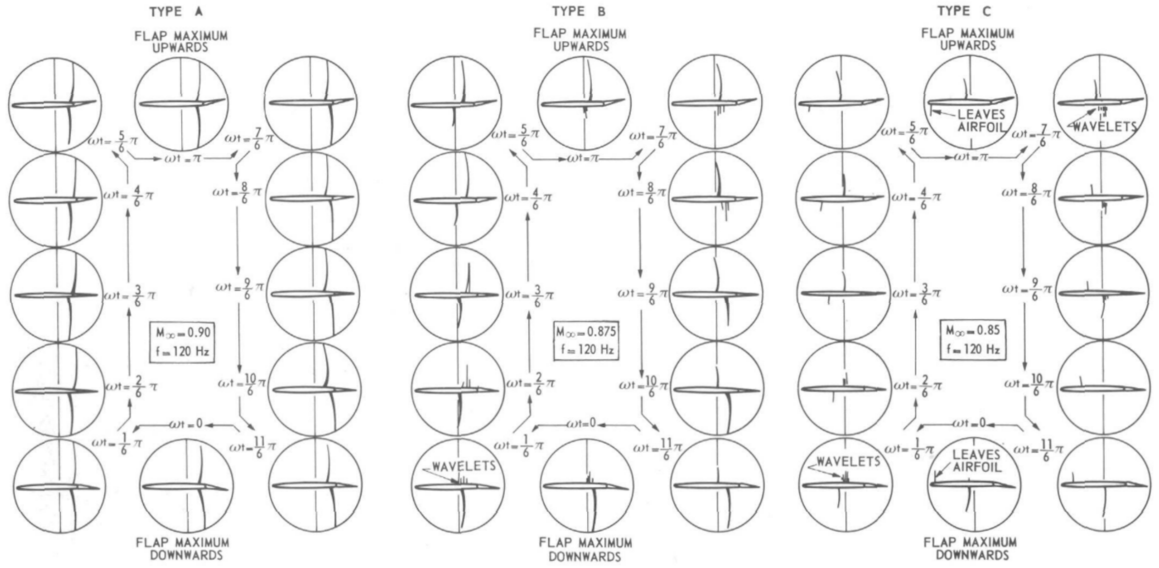

Fig. 2.6 Types of shock wave oscillations observed by Tijdeman [9]

2.4.1 Early experiments on symmetrical aerofoils

The first observation of something similar to what is now known as shock-buffet dates from 1940s. Hilton and Fowler have documented in [10] an aperiodic shock oscillation coupled with unsteady boundary layer separation.

Three decades later, McDevitt *et. al.* were the first ones to produce a detailed study on the shock-buffet regimes. An 18% thick symmetric circular arc aerofoil was experimentally tested at a range of $M_\infty = 0.71 - 1.4$, and chord $Re = \rho U_\infty c/\mu = 1 - 17$ million [11]. The experimental setup used is shown in Fig. 2.7.

The study revealed unsteady, period shock oscillations present in the region of $M_\infty = 0.76 - 0.78$ at all Re. As a general observation, at the lower end of the Re range, a higher M_∞ was needed to produce the unsteady shock-buffet. Increasing the value of M_∞ past 0.78

resulted again in a steady flow with significant shock-induced separation that spanned from the shock-foot to the trailing edge of the aerofoil. Interestingly, decreasing the M_∞ back to lower values resulted in a hysteresis effect which can also be observed in the shock-buffet envelope given in Fig. 2.8.The authors measured the frequency of oscillation via pressure transducers and determined it had a value of 188 Hz (or equivalent *St* of 0.16).

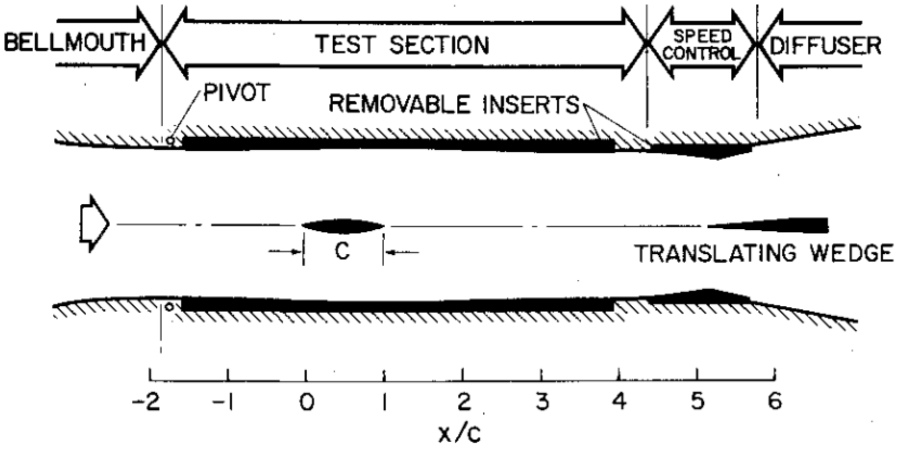

Fig. 2.7 Experimental setup from [11]

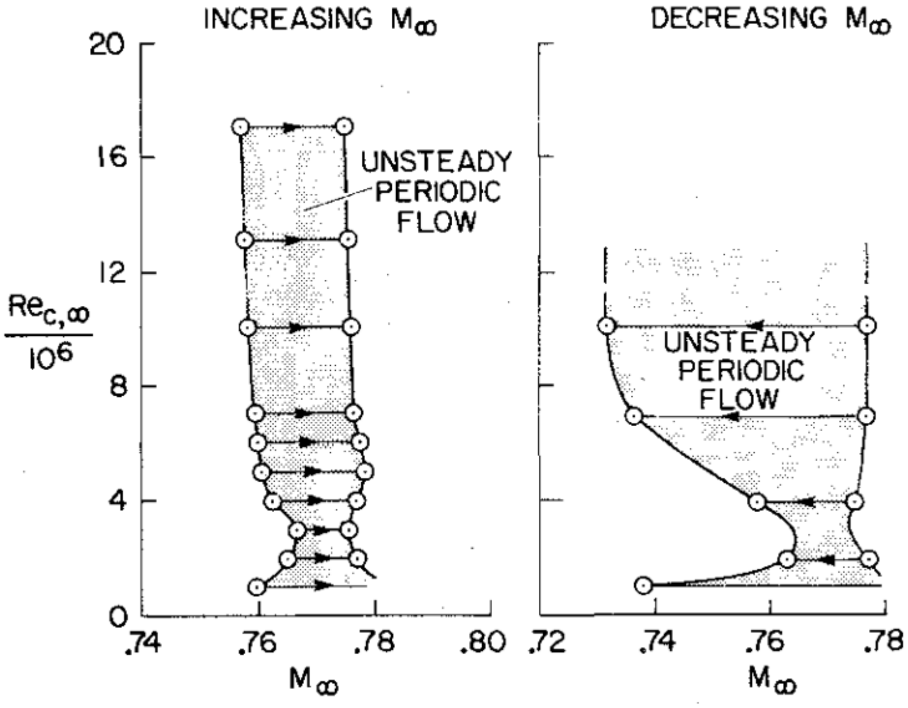

Fig. 2.8 Buffet envelope obtained in [11]

Subsequent experiments using the same approach were conducted in [12], [13], and [14].

In [13], the same experimental setup was used at freestream condition of $M_\infty = 0.76 - 0.79$, and chord $Re = 11$ million. Laser velocimetry was used to measure field quantities downstream of the shock location: mean velocity, shear stresses, turbulent kinetic energy. At the higher M_∞, the authors found the flow to be steady, with a fully separated boundary layer, spanning from the foot of the shock and past the trailing edge of the aerofoil. This observation was in good agreement with the shock-buffet envelope given in Fig. 2.8.

Surface pressure measured through a transducer at lower M_∞ conditions, revealed a periodic oscillation with a frequency of 188 Hz. Since the flow was incoming at an incidence, α of 0°, and the aerofoil being symmetrical, this periodic oscillation was also captured on the lower surface, but out of phase by 180°. The mechanism of this oscillation was visualised using shadowgraph images. Weak shock waves were observed to merge near the trailing edge, resulting in a stronger shock which then travelled upstream towards the middle of the chord where it disappeared before the cycle starting all over again. [13] (see Fig. 2.9).

The cycle described above is discontinuous in nature. It describes a Tijdeman shock motion of type B (see Fig. 2.6): the shock forms at the furthest downstream position through coalescing of multiple weak shock waves. As it travels upstream, it becomes weaker and disappears at the most upstream position of the oscillation. The cycle repeats as the shock re-appears near the trailing edge. [9].

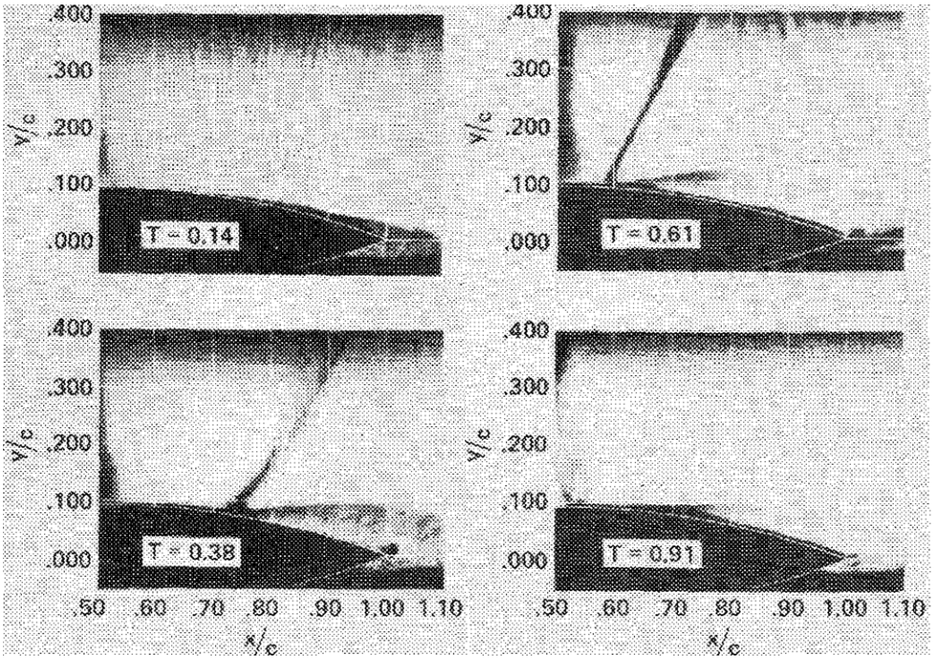

Fig. 2.9 Buffet cycle visualised through shadowgraph pictures in [13]

Further analysis of this experimental setup at $M_\infty = 0.76$ and chord $Re = 11$ million was performed by Marvin *et. al.* in [14] with focus on understanding the evolution of turbulent structures during one shock-buffet cycle. Figure 2.10 shows that during one shock-buffet cycle, two types of boundary layer separation are present. At the beginning of the buffet cycle, when the compression waves coalesce near the trailing edge, the flow is dominated by a trailing edge separation. As the shock moves upstream, shock-induced separation forms immediately behind it, which grows significantly in size. As the bottom of Fig. 2.10 shows, the Mach number immediately upstream of the shock, M_s, decreases, indicating a decrease in shock strength. This is coupled with the sudden collapse of the shock-induced separation before the cycle repeats.

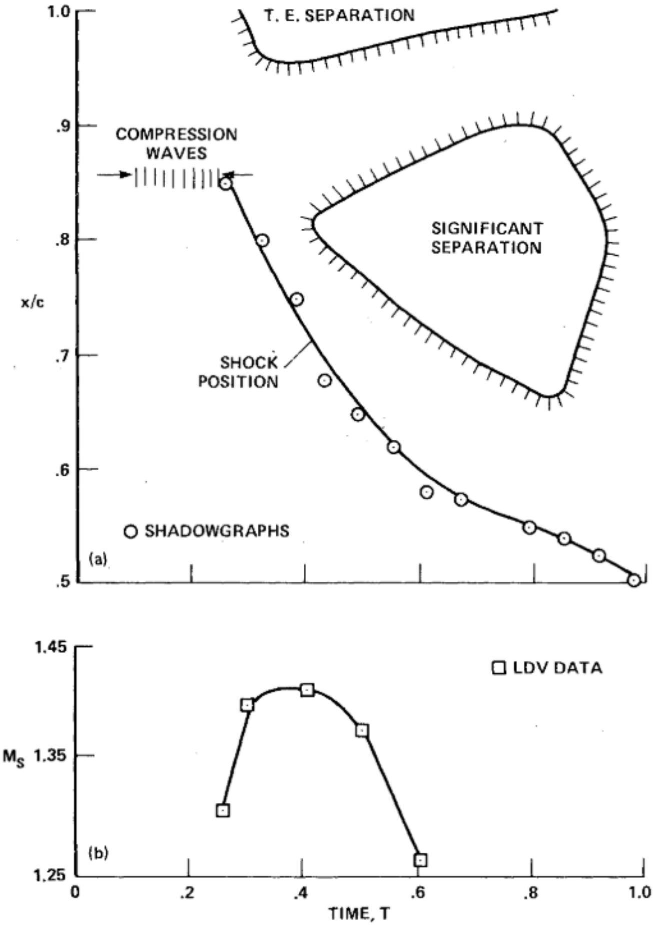

Fig. 2.10 Buffet cycle visualised through: a) position of shockwave and development of the separation zone; b) value of Mach number immediately upstream of the shock (reproduced from [14])

All the experiments described above also had their contribution towards producing a comparison between the experimental observations and the numerical capabilities available at the time. One remarkable observation, made in [14] is that linear eddy-viscosity models available at the time would not be appropriate for modelling the complex interactions developed in the separated shear layer.

Two other noteworthy studies were conducted in [15] and [16] on circular arc aerofoils but of varying thicknesses. Similar observations were found which led to the first publication of a shock-buffet mechanism by Gibb in 1988 [17]. Gibb's shock-buffet mechanism is presented in Fig. 2.11. It describes out of phase shock oscillations on both sides of a symmetrical aerofoil coupled with boundary layer separation.

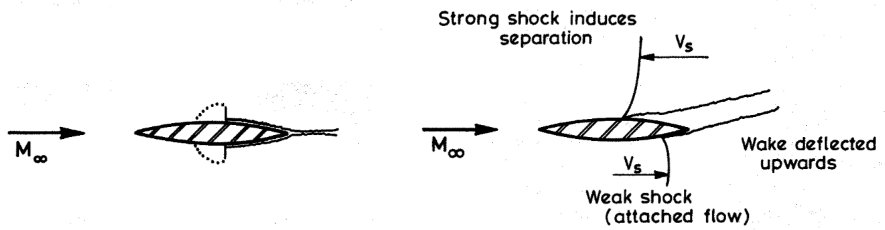

(a) M_∞ slightly greater than M_{crit}

(c) Periodic flow starts.

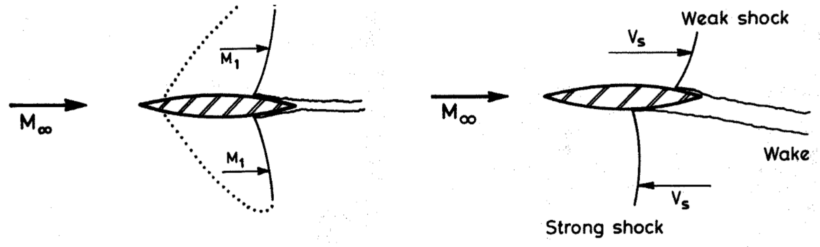

(b) High subsonic Mach number but shock strength M_1<1.2 (no seperation)

(d) 1/2 cycle after (c)

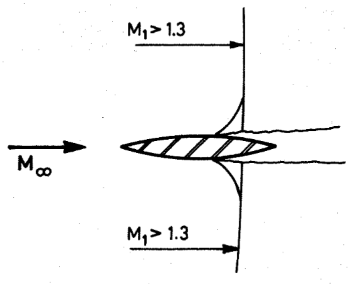

(e) Shock waves now too strong for re-attachment to take place during periodic flow cycle, oscillation stops.

Fig. 2.11 First shock-buffet mechanism produced for a symmetrical circular arc airfoil in [17]

2.4.2 Experiments on conventional and supercritical aerofoils

More relevant to today's commercial flight are the observations made on conventional and supercritical aerofoils or wings. Roos is one of the first to perform such experiments on the Whitcomb and NACA0012 aerofoils in [18]. The aerofoils were tested at various M_∞ and C_L. Design point conditions of $M_\infty = 0.82$ and $C_L = 0.53$ for the Whitcomb; and $M_\infty = 0.68$ and $C_L = 0.42$ for NACA0012 were selected as a starting point. Then, while maintaining a fixed freestream Mach number or C_L, the other variable was increased until penetration into the heavy shock-buffet regime.

Roos found that shock-buffet developed on the Whitcomb aerofoil when M_∞ was maintained at 0.82 and C_L increased from design point value (0.53) up to 0.91. In comparison, the NACA0012 aerofoil presented shock-buffet at design point C_L when the value for M_∞ was increased from 0.68 to 0.77.

The two profiles exhibited similar shock-buffet dynamics. Figure 2.12 quantifies shock-buffet through fluctuation of pressure coefficient, C_P', over the upper side of the aerofoils. C_P' is given for increasing C_L or M_∞ for Whitcomb and NACA0012 aerofoils respectively. At design point C_L or M_∞, neither of the two aerofoils showcase large amplitude fluctuation, although a peak C_P' is present at shock location in compliance with type 1 weak SWBLI [7] discussed in Section 2.3. As C_L or M_∞ is increased, the amplitude of C_P' at shock location increases significantly and the chordwise location of the shock moves downstream. Before penetration into shock-buffet, Fig. 2.12 shows type 2 SWBLI [7] with fluctuations present at the trailing edge / separation bubble at shock foot are present. At highest values of C_L or M_∞ high amplitude of pressure fluctuation were captured across the shock and in the downstream region dominated by separated flow.

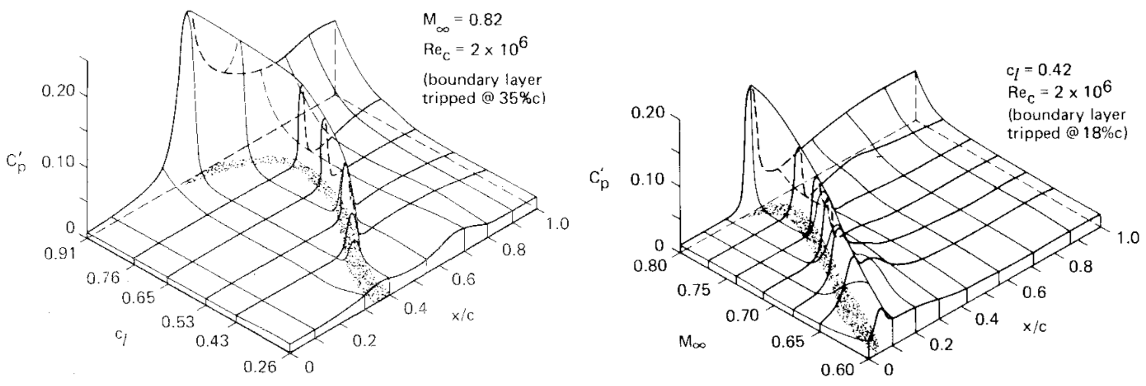

(**a**) Whitcomb supercritical (**b**) NACA0012

Fig. 2.12 Fluctuation of C_P as a function of lift (Whitcomb) and Mach number (NACA0012) in relationship with shock wave position (dark regions) [18]

Figure 2.13 adapted from [18] correlates the increase in amplitude of lift coefficient fluctuation (c_l') with the divergence of trailing edge (TE) pressure coefficient ($C_{P,te}$) on the Whitcomb aerofoil. Roos discovered that a strong correlation exists when increasing C_L (via a corresponding increase in incidence α) and maintaining M_∞ fixed, indicating that divergence of $C_{P,te}$ is a good indicator of shock-buffet. However,if C_L is maintained at design point value and M_∞ is increased, the experiments showed that $C_{P,te}$ divergence can occur also when steady shock-induced separation is present. This observation shows the unreliability of $C_{P,te}$ divergence condition as a shock-buffet onset indicator.

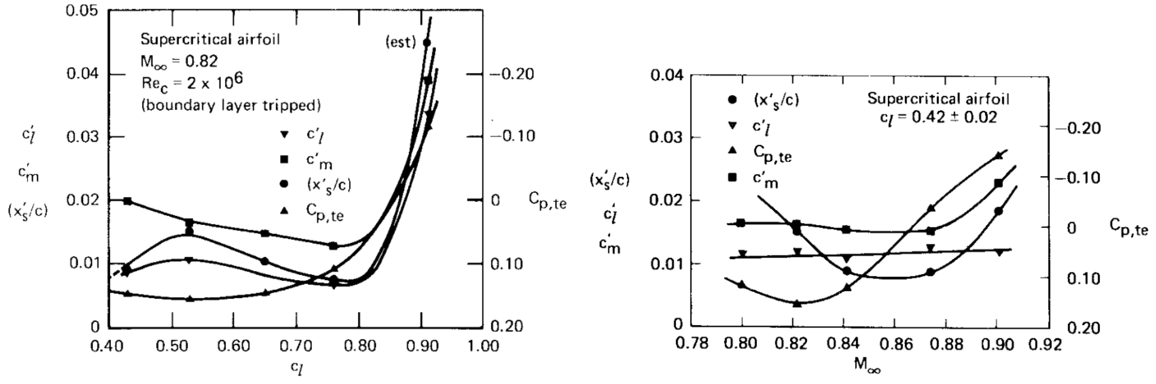

(**a**) with increasing c_l (**b**) with increasing M_∞

Fig. 2.13 Relationship between pressure oscillation magnitude, shock oscillation magnitude, and trailing-edge pressure divergence on the Whitcomb supercritical aerofoil [18]

Lee and Ohman [19] performed experiments on the BGK No. 1 aerofoil at $0.5 < M_\infty < 0.8$, and $15m < Re_c < 21m$. Shock-buffet was present at testing conditions of $M_\infty > 0.7$ and $0.8 < C_L < 1.1$. The frequency which was measured was found to increase with an increase in M_∞. The fluctuations in C_L and C_P were similar to those found by Roos in [18]. The BGK No. 1 aerofoil was later compared with the WHEA II by Lee *et. al.* in [20]. The aim was to assess the effect of the thickness to chord ratio (t/c) on buffet onset. The WHEA II aerofoil had a $t/c_{max} = 16\%$, whereas the BGK No. 1 was thinner at $t/c_{max} = 11.8\%$ only. The two aerofoils were experimentally tested at M_∞ of 0.612-0.792 and 0.5-0.818 for the WHEA II and BGK No. 1 aerofoil respectively. The Re_c was maintained at 20 million throughout. Lee *et. al.* found that at M_∞ lower than 0.7, the buffet onset envelope (see Fig. 2.14) for the two aerofoils were identical, but at higher M_∞, the thicker, WHEA II aerofoil entered the shock-buffet regime at lower C_L values. At design point M_∞, the BGK No. 1 aerofoil had a lower C_L margin to buffet onset than the WHEA II profile which is undesirable from an industrial perspective.

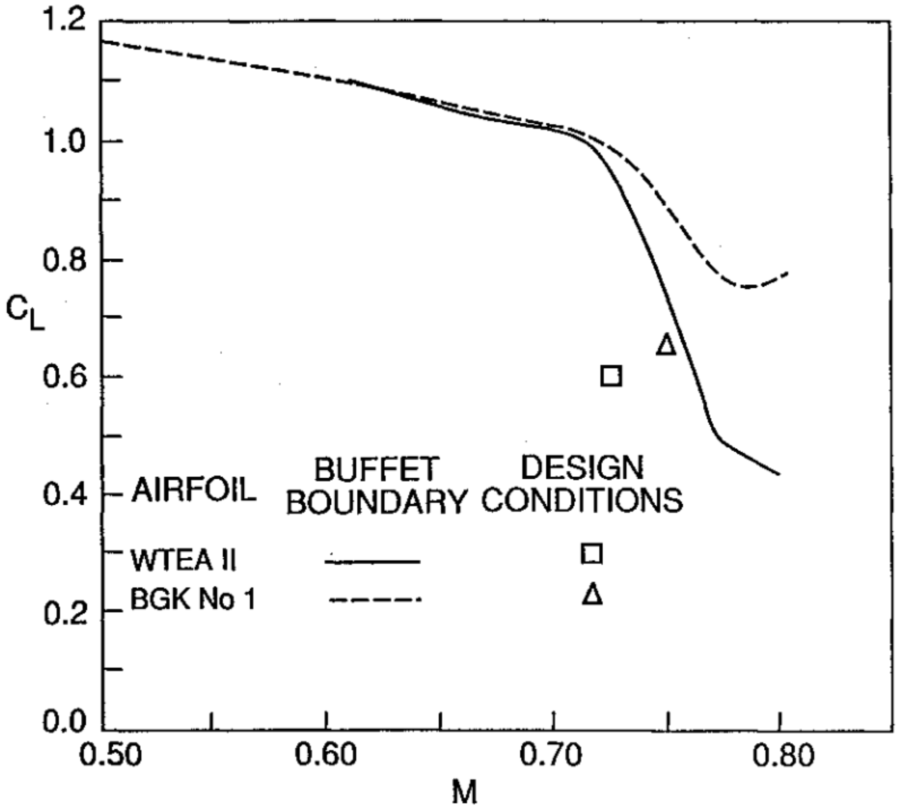

Fig. 2.14 Buffet envelope comparison for two aerofoils of different thickness [20]

Lee's work resulted in him proposing one of the two most well known mechanisms explaining the cause of the self-sustained, periodic nature or shock-buffet. The acoustic wave propagation mechanism is shown in Fig. 2.15. Lee found that small shock oscillations resulted in pressure disturbances which propagate downstream in the separated flow region with a velocity a_p. As they reached the trailing edge, they reflect in all directions, generating upstream moving waves at velocities a_u. These upstream travelling waves would then interact with the main shock on the wing, transferring energy which maintains the oscillation. The cycle is then completed and repeats itself. Lee also found that if this mechanism is true, then the shock-buffet period should be equal to the time it takes a disturbance to propagate from the shock to the trailing edge and then reflect back upstream to reach the shock again. [21].

Lee produced initial experimental observations which confirmed his shock-buffet mechanism. This development was critical towards understanding the buffet phenomenon.

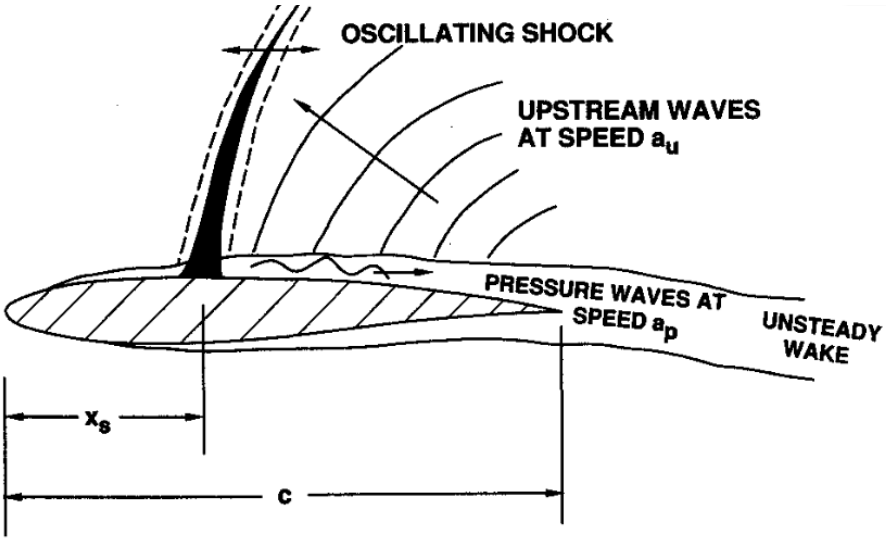

Fig. 2.15 Acoustic wave propagation buffet mechanism proposed by Lee in [21]

Over the years, Lee's shock-buffet acoustic wave propagation mechanism has received ample support from the scientific community. The most recent contribution was by Feldhusen-Hoffmann *et. al.* [22]. In their experimental investigations, the DRA 2303 supercritical aerofoil was tested at $M_\infty = 0.73$, Re_c = 1.6 million, and $\alpha = 3.5°$. The flow surrounding the profile was determined to be dominated by the shock-buffet phenomenon. The authors stimulated the flow using a loudspeaker which was emitting acoustic waves at the buffet frequency. The experiments revealed an increased level in the power spectra distributions (and thus amplitude of fluctuation) recorded due to the acoustic stimulation.

With advancing technology and use of CFD in transonic aerodynamics regimes, the lack of comprehensive validation data needed to be addressed. Jacquin *et. al.* [23] put together a detailed test campaign with the primary aim to generate shock-buffet validation data.

The OAT15A supercritical profile was experimentally tested in the S3Ch ONERA facility. The freestream M_∞ was varied between 0.7 and 0.75, Re_c was maintained at 3 million, and incidence α was set between 2.5 and 3.91°. The model was fitted with 68 static pressure orifices and 36 unsteady pressure Kulite transducers. Data collection included steady and unsteady pressures, oil flows, and Schlieren films.

The focus of Ref. [23] was on the experiments run at $M_\infty = 0.73$. At this freestream condition, shock-buffet onset was determined to be at $\alpha = 3.1°$. Large shock displacements in the chordwise direction were then captured by the Schlieren films at an incidence of $\alpha = 3.5°$. The mean C_P distributions and C_{Prms} from the Kulite sensors are given in Fig. 2.16 for various values of α. Figure 2.16a show a typical C_P distribution for a supercritical profile. The supersonic plateau and the sharp increase in pressure across the shock are evident. Up to an incidence of 3.0° the shock remains steady. For higher incidences, shock-buffet is present. The C_{Pmean} distributions reveal that through a spreading in the chordwise direction of what was initially a sharp pressure increase across the shock.

These observations are backed by the C_{Prms} values in Fig. 2.16b. The level of fluctuation in the pressure increased with incidence. Higher levels of pressure fluctuation were captured in the vicinity of the shock location than in the separated boundary layer immediately downstream of it. At $\alpha = 3.9°$ the fluctuations of the shock cover as much as x/c = 0.2. The amplitudes and trends found by Jacquin *et. al.* are consistent with previous observations by Roos [18]. Frequency analysis of unsteady pressure signals revealed a 2D buffet frequency $f_b = 69$ Hz ($St = 0.065$). In terms of buffet frequency, the authors mentioned that varying the value for M_∞ resulted in a change in frequency too, revealing the impact of M_∞ on shock-buffet.

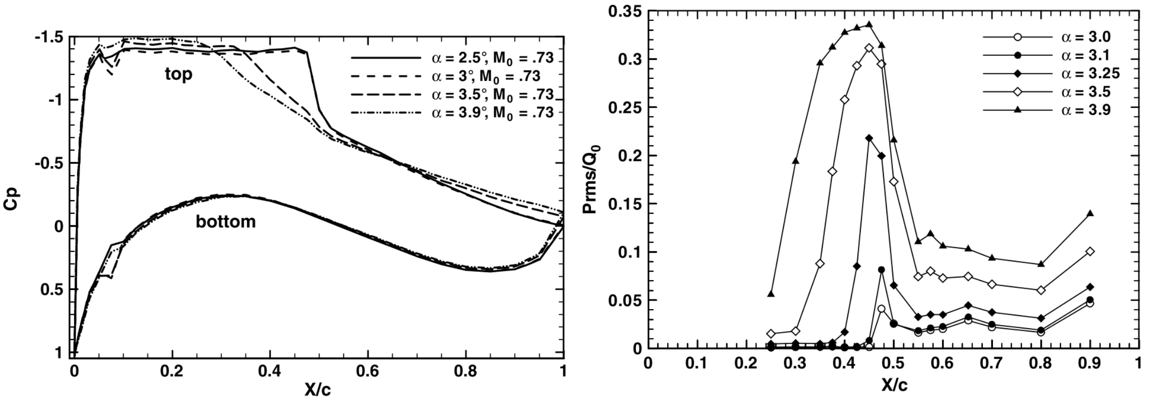

(a) C_{Pmean} **(b)** C_{Prms}

Fig. 2.16 Pressure coefficient distributions obtained by Jacquin *et. al.* [23]

Laser Doppler Velocimetry (LDV) was used to sample the velocity flow field at $M_\infty = 0.73$ and $\alpha = 3.5°$. The phase averaged velocity fields at 4 instances during a shock-buffet period are shown in Fig. 2.17. The velocity fields show a periodic detachment and reattachment of the boundary layer coupled with the shock oscillation.

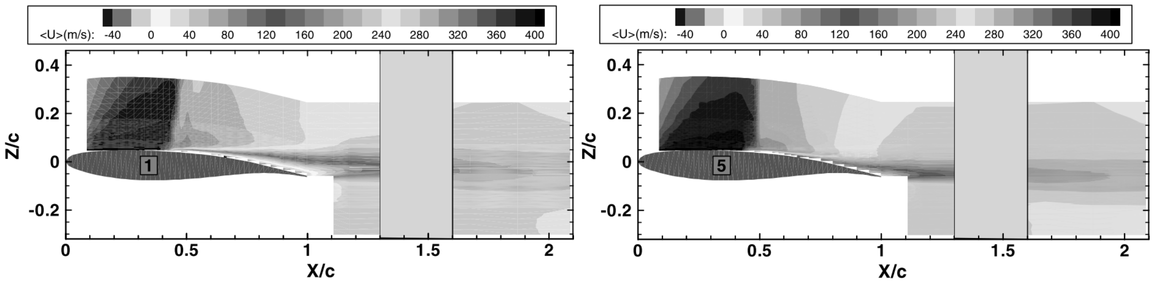

(a) shock most upstream **(b)** shock travelling downstream

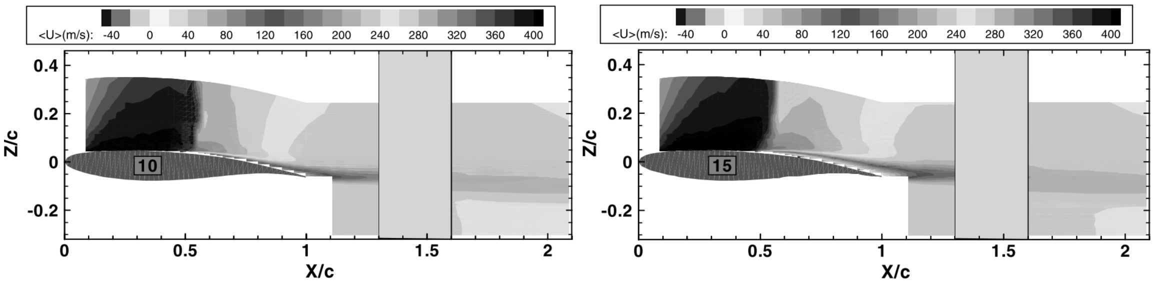

(c) shock most downstream **(d)** shock travelling upstream

Fig. 2.17 Velocity fields measured with LDV in [23]

The experiments from Ref. [23] have subsequently been used for a series of numerical studies which concern shock-buffet prediction on 2D aerofoils. These will be discussed in Section 2.4.4.

2.4.3 Experiments on 3D configurations

Roos extended his work to 3D wing configurations in [24]. He presented key differences between shock-buffet obtained in his 2D experiments of [18] and those on 3D configurations. There were two noteworthy observations coming from his experiments. First, that on 3D wings, shock-buffet extends not only in the chordwise, but also in the spanwise direction. Secondly, 3D shock-buffet is a multi-frequency phenomenon, with a broadband of frequencies between $0.2 < St < 0.6$ being identified in lift and pressure signals.

Dandois introduced in [25] the results of two experimental investigations conducted on 3D models based on the 2D OAT15A profile described in the previous section. The tests in the S3Ch wind tunnel was set at $M_\infty = 0.82$, $Re_{mac} = 2.5$ million, and $\alpha = 2-4°$. The tests in the S2MA wind tunnel, on a similar model, were conducted at $M_\infty = 0.78-0.86$, $Re_{mac} = 2.83-8.49$ million. Steady and unsteady wall pressures were measured, oil flow visualisations were used to identify areas of flow separation.

In [25], both experiments revealed that the 3D shock-buffet phenomenon occurs over a range of frequencies between $St = 0.1-0.6$ with the highest coherence in the spanwise direction to occur at a St close to 0.3.

Molton *et. al.* [26] and Dandois *et. al.* [27] complemented the results in [25] by successfully applying shock-buffet control solutions with conventional and air-jet vortex generators.

Lawson *et. al.* [28] produced experimental observations of shock-buffet response on the RBC12 half wing-body model in the Aircraft Research Association's Transonic Wind Tunnel (ARA TWT). Data was collected using strain gauges, accelerometers, steady and unsteady pressure transducers, and visualisations were generated by means of dynamic pressure sensitive paint (PSP). The value for M_∞ was varied between 0.7 - 0.84, and Re_{mac} maintained between 2.8 and 3.9 million. The experiments focused on investigating different buffet-onset indicators, as well as, producing a characterisation of the shock-buffet phenomenon.

Six different shock-buffet onset indicators were evaluated. The buffet-onset maps ($\alpha - M_\infty$) obtained with all 6 are given in Fig. 2.18. The authors found good prediction of shock-buffet onset using 4 of the 6 indicators:

- shock-buffet onset characterized by a divergence in the wing root strain measurements.
- shock-buffet onset characterised by an increase of fluctuation of the wing tip acceleration.
- shock-buffet identified at the intersection between the C_L vs α curve with the linear portion of it after it was translated by $\Delta\alpha = 0.1$ °.
- shock-buffet onset predicted well by the trailing-edge pressure divergence

Frequency analysis of the data produced by Lawson *et. al.* and subsequently by Masini *et. al.* [29] revealed that on this aircraft configuration, shock-buffet occurs at $St = 0.08 - 0.16$, values lower than typically encountered on other aircraft configurations. Dynamic PSP images showed that the shock-buffet phenomenon occurred on the outboard part of the wing for this particular aircraft configuration.

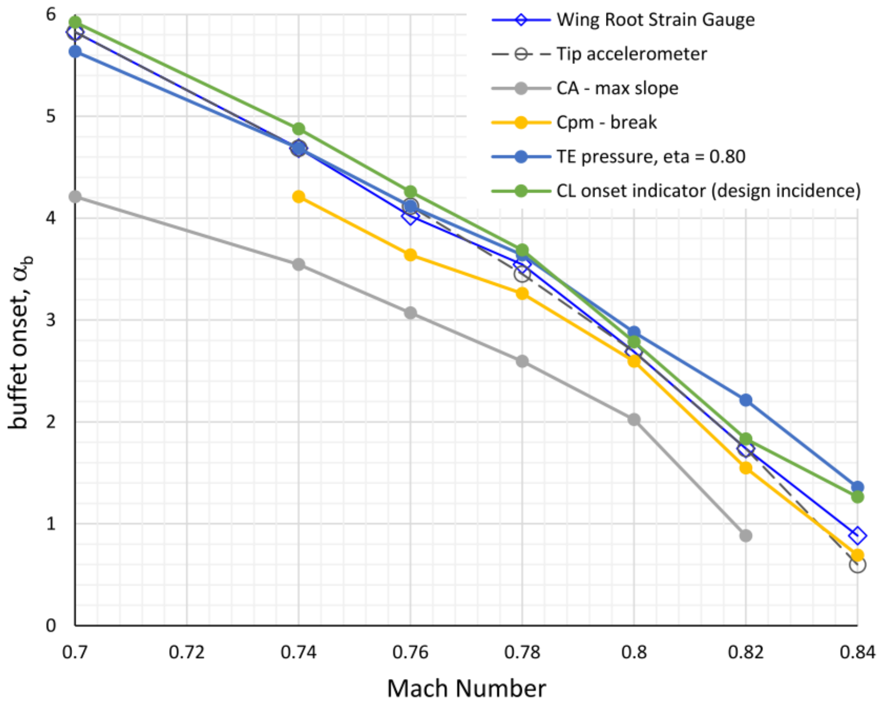

Fig. 2.18 Buffet-onset envelopes as predicted by the 6 indicators investigated in [28]

The shock-buffet response of the NASA Common Research Model (CRM) wing-body aircraft configuration was investigated in [30], [31], [32], [33], and [34] at $M_\infty = 0.85$ and $Re_{mac} = 0.9 - 30$ million.

Balakrishna and Acheson [30] provided a first insight into the freestream incidences at which shock-buffet occurs on this aircraft. The model was tested in the NASA facilities at $M_\infty = 0.70$ and 0.85; $Re_{mac} = 5.0$, 19.8, and 30 million. Their analysis was limited in scope due to lack of instrumentation on the CRM wind tunnel model. Only one wing root strain gauge and one unsteady pressure sensors were mounted. The authors defined C_B, the buffet coefficient, as a measure of the amplitude of the fluctuation recorded in the root strain signals. The value for C_B obtained at two M_∞ and $Re_{mac} = 5.0$ million are given in Fig. 2.19.

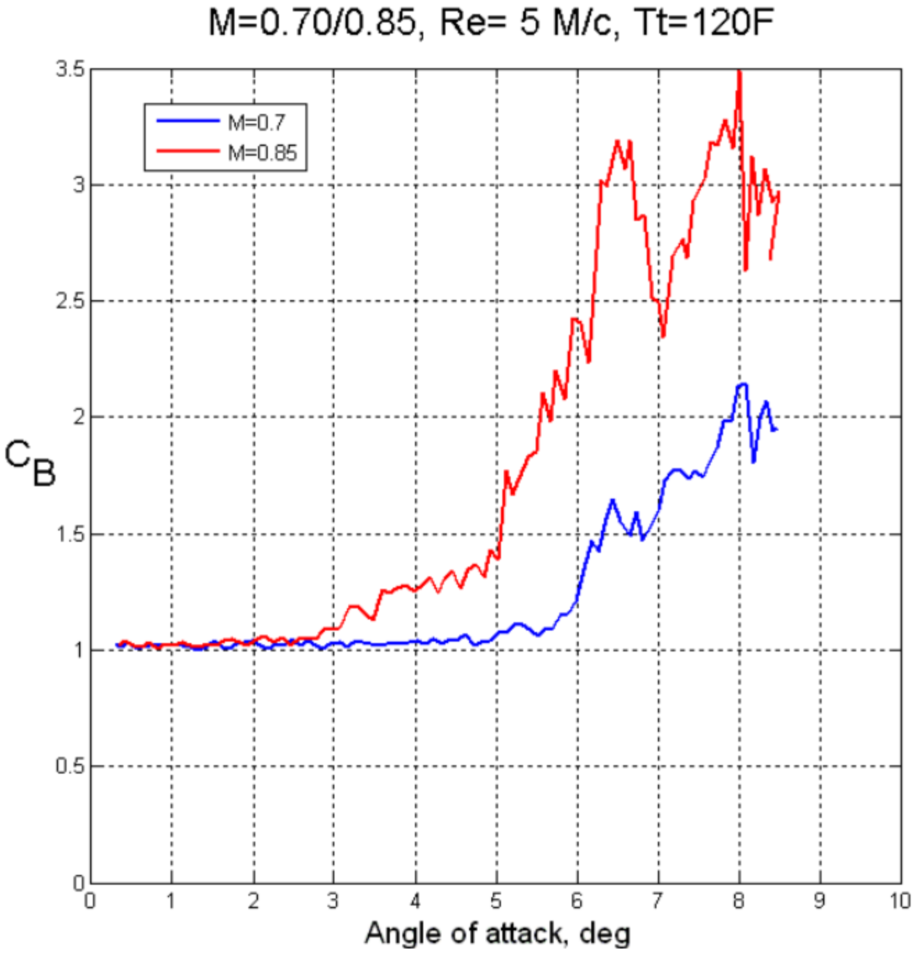

Fig. 2.19 Root strain gauges recorded at $M_\infty = 0.70$ and 0.85, and $Re_{mac} = 5.0$ million in [30]

The effect of M_∞ is clear, a lower freestream Mach number resulted in a delayed buffet onset. At $M_\infty = 0.85$, the authors found buffet onset to be at $\alpha_{onset} = 3.0°$. Two subsequent buffet regimes were defined. First, between $\alpha = 3.0 - 5.0°$, the increase in fluctuation is minimal, thus the shock fluctuations were believed to remain of small amplitude. The second buffet regime, characterised by high amplitude fluctuations was recorded at incidences, α, higher than 5.0°.

Koike *et. al.* [33] experimentally tested the NASA CRM in the Japan Aerospace Exploragion Agency (JAXA) facilities. M_∞ was maintained at 0.85, Re_{mac} was chosen as 0.95 and 1.5 million. Unsteady pressure data was recorded at two spanwise locations, $\eta = y/b = 0.5$ and 0.6. The analysis of the pressure fluctuation revealed a buffet onset at an incidence of $\alpha_{onset} = 3.0°$. The authors concluded in a similar manner with Balakrishna and Acheson that following the onset of the buffet there are two buffet regimes: one of small shock oscillation in the chordwise direction (in this case $3 < \alpha < 5.5°$), and the other characterised by large shock oscillations in the chordwise directions ($\alpha > 5.5°$). Frequency analysis of the data revealed a broadband of frequencies present, with the dominating St of 0.3.

Sugioka *et. al.* [32] [34] complimented the results obtained by Koike *et. al.* by conducting more experiments on the NASA CRM, and collecting data using fast-response PSP. This technique allowed for a more in-depth analysis of the three-dimensionality of the shock-buffet phenomenon at $M_\infty = 0.85$ and $Re_{mac} = 1.54$ million.

Mean C_P, M_{loc} (local Mach number), and C_{PRMS} contours obtained at various incidences are given in Fig. 2.20. The transonic aerodynamics of a wing are evident. A lambda shock front is easily visible at all incidences. As incidence increases two things happen. First, the shock front travels in the upstream direction. Secondly, as the M_{loc} contours reveal, the Mach number imediately upstream of the shock increases. This suggests an increase in the shock-strength and a higher possibility of shock-induced separation.

The C_{PRMS} contours reveal that at $\alpha = 2.82°$, corresponding to a C_L value lower than the design point, no significant fluctuation is visible. At $\alpha = 4.68$ and 6.0 °, the values of C_{PRMS} at the shock front increase, but the spatial distribution remains along the shock front. Only at $\alpha = 6.52°$, the fluctuations cover a larger area of the wing, indicating significant spanwise and chordwise fluctuations of the shock.

Another interesting feature of the shock-buffet phenomenon captured in [34] is a spanwise shock waviness which gives birth to the so called *buffet cells*, a term pioneered by Iovnovich

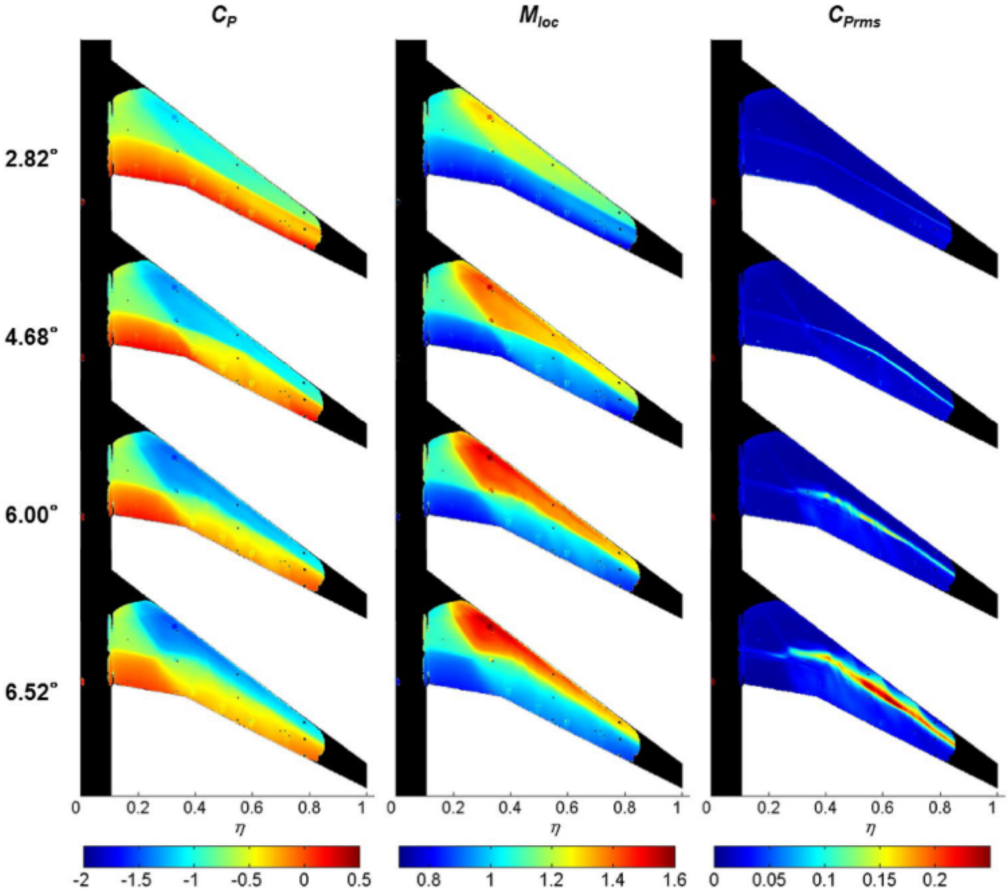

Fig. 2.20 Mean and RMS values of C_P as measured using fast-response pressure sensitive paint in [34]

et. al. in [35]. The authors produced time-accurate contours of the variable $C'_P = C_P - C_{Pmean}$. The contours obtained for an incidence $\alpha = 6.0°$ are given in Fig. 2.21 at 9 instances. An interesting feature is present along the shock front. The buffet cells of alternating colours are visible. Observing their evolution in time, they can be seen to travel in the outboard direction. Alternating colours in the buffet cells, representing positive and negative values of C'_P, indicate if the time-accurate position of the shock wave is upstream (-ve C'_P) or downstream (+ve C'_P) from its mean position.

Figure 2.21 indicates that the time-accurate shape of the shock front is wavy. Frequency analysis of this data helped understand the modes in which the shock oscillates. Sugioka *et. al.* found two dominant modes of different frequencies ($St = 0.09$ and $St = 0.31$) and wavelengths In Fig. 2.22 these two modes are sketched.

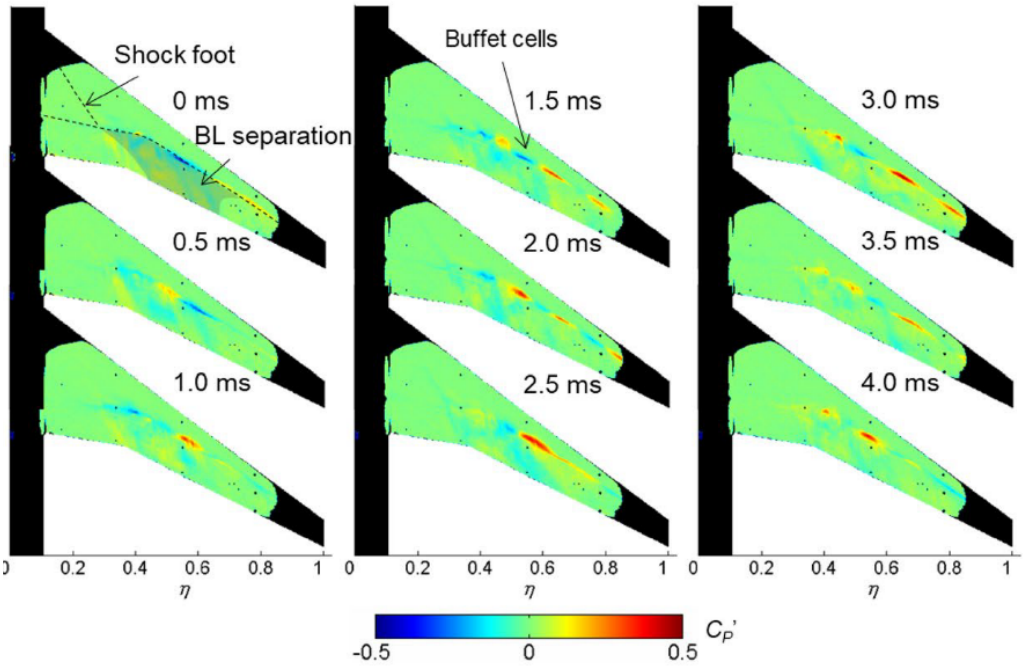

Fig. 2.21 Buffet-cells observed in [34]

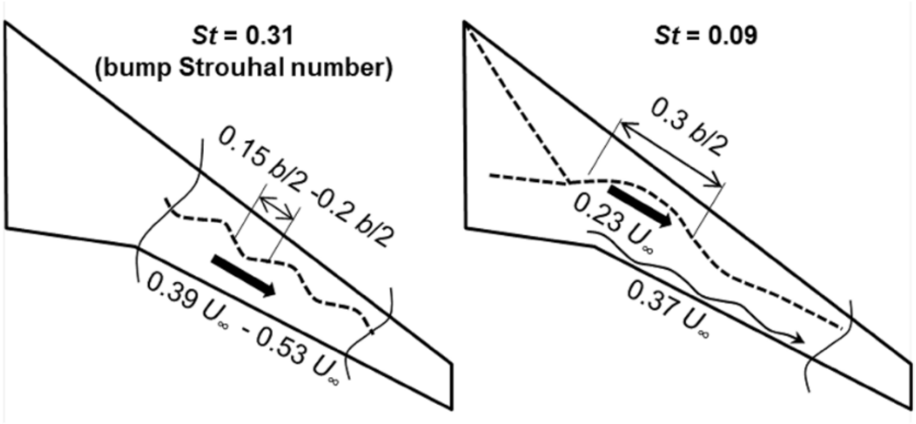

Fig. 2.22 Sketches of the two main modes of shock oscillations observed in the experiments of Sugioka *et. al.* [34]

In a 2019 study by Paladini *et. al.* [36], experiments based on four different three-dimensional swept wings were compared. The authors strived to produce an understanding of which shock-buffet characteristics are generally valid and which are configuration dependant. Their conclusions were that oscillation *St* were consistently between 0.2 and 0.3 for all four aircraft configurations, a finding that is in agreement with other experimental observations performed by others.

2.4.4 Numerical predictions of shock-buffet

The first mention of a Navier-Stokes-based simulation of the shock-buffet phenomenon was by Levy in [12]. A circular arc 18% thick symmetric aerofoil was simulated at $M_\infty = 0.72$, 0.754, and 0.783, corresponding to three flight regimes: attached flow, shock-buffet, and fully-separated steady flow. Experimental data was available for validation purposes.

At the lowest $M_\infty = 0.72$, the numerical simulations accurately captured the shock position and strength, as well as the pressure recovery downstream of the shock. A discrepancy was found at the trailing edge, where some trailing-edge separation was present in the experiments but not in the numerical results. The numerical results for the fully-separated, steady flow at $M_\infty = 0.783$ compared well with the experiments only upstream of the shock. The author suggested that the turbulence model used to close the Reynolds-averaged Navier-Stokes (RANS) equations was primitive and not adequate for accurate predictions of shock-indunced boundary layer separation.

The simulations at $M_\infty = 0.754$ captured the shock-buffet phenomenon. A comparison between experiments and numerical results is given herein in Fig. 2.23. A qualitative comparison could be performed between experiments and numerical results. Similar levels of pressure fluctuations were computed in the time-accurate simulations. The buffet cycle was qualitatively similar.

Other early experiments on circular aerofoils concluded that the prediction of shock-buffet using an unsteady RANS (URANS) approach had similar conclusions. The prediction of shock-buffet using URANS was highly dependant on the turbulence modelling approach [13][14].

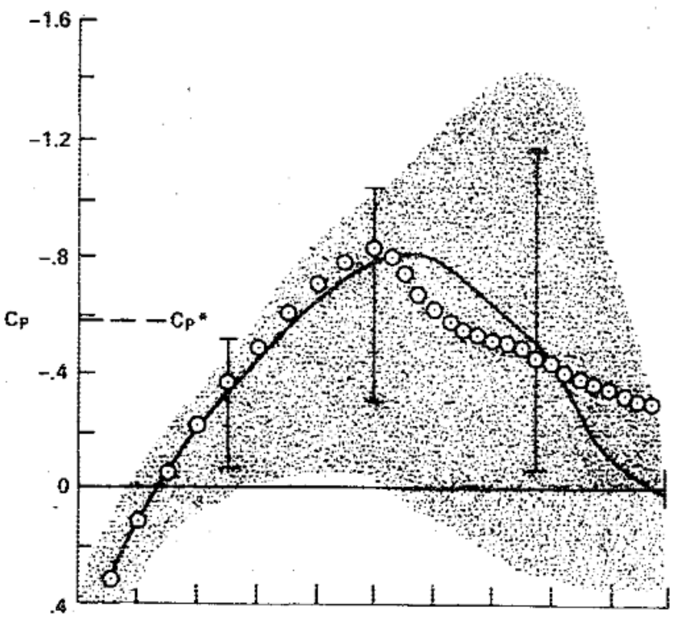

Fig. 2.23 Comparison of C_P on the upper side of the aerofoil. Numerical results are given by the solid line (C_{Pmean}) and shaded area (time-accurate C_P). Experimental mean and time-accurate values are given through symbols and error bars respectively

Numerical results on the OAT15A configuration

The experiments performed on the OAT15A aerofoil in [23] have been since used for a series of numerical studies in which CFD capabilities have been tested. In the experiments, the aerofoil was under shock-buffet at flight conditions of $M_\infty = 0.73$, $Re = 3$ million, and $\alpha = 3.5°$.

Brunet has studied in [37] the effect of different turbulence models and numerical parameters on shock-buffet prediction. His initial assessment concluded that URANS can be used in the context of shock-buffet prediction, despite the fact that some turbulence models required only captured it at a higher angle of attack than the experiments.

In [38], the explicit algebraic Reynolds Stress Model (EARSM) of Shih, Zhu and Lumley (SZL) [39] was used as an advanced closure to the URANS equations. The authors found that self-sustained shock-buffet was only predicted from an incidence $\alpha = 4.5°$ onwards.

Thiery and Coustols [40][41] produced numerical results in which the effect of turbulence models, wind tunnel geometry (see Fig. 2.24), and three dimensionality of the problem are assessed. The authors selected the Spalart-Allmaras (SA) [42], the k-ω BSL (BSL) and Shear Stress Transport (SST) [43], and the KKL [44] turbulence models for comparison. Solutions were produced using the ONERA elsA code, the URANS equations were discretized by a second-order Jameson scheme with artificial viscosity, the turbulent transport equations were discretized using a Roe scheme.

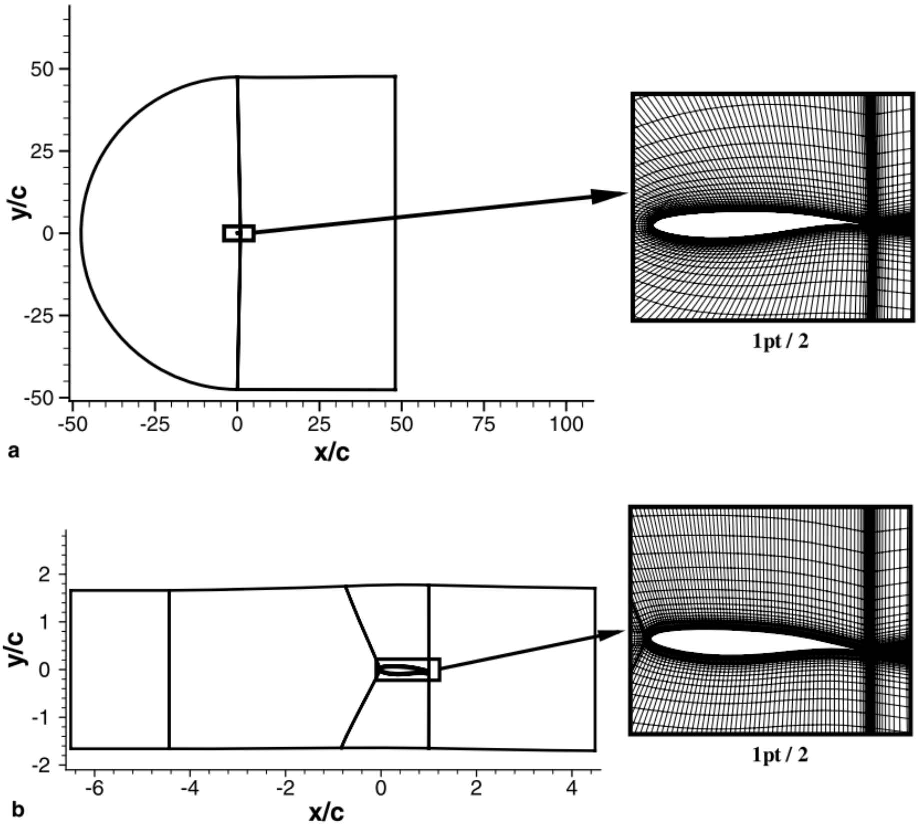

Fig. 2.24 The free flight (a); and wind tunnel condition (b) grids and geometries used in [41]

When comparing the turbulence models, Thiery and Coustols found that the SST and KKL produced shock-buffet response both in free flight and wind tunnel condition. The SA only captured buffet when the wind tunnel walls were accounted; and the BSL turbulence model did not capture any shock induced unsteadiness. Modelling the upper and lower wind tunnel walls resulted in an increased amplitude of the shock wave oscillation in both predictions by the SST and KKL turbulence models. The computed frequency of oscillation varied with turbulence model and ranged from 71 to 78 Hz, which is higher than the experimental value of 69 Hz.

In the 2D studies, only the upper and lower walls of the wind tunnel were considered, in the 3D studies from [41], the side walls were considered as well. Only the SST turbulence model captured a self-sustained oscillation. From Fig. 2.25, adding the side walls of the wind tunnel resulted in a decrease in oscillation amplitude. The final fluctuations were similar to the ones computed in the 2D free flight simulations.

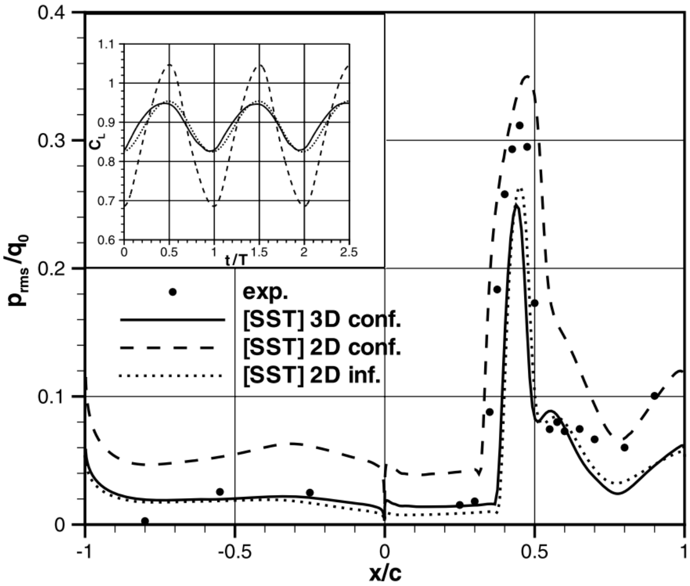

Fig. 2.25 The effect of wind tunnel walls on computed shock-buffet oscillation amplitude in [41]. "2D inf." - free flight; "2D conf." - top and bottom walls accounted for; "3D conf." - full 3D wind tunnel geometry

Deck [45] computed the shock-buffet regime on the OAT15A aerofoil using URANS closed with the SA turbulence model, Detached Eddy Simulations (DES), and pioneered the Zonal DES (ZDES) approach. This was one of the first efforts in using a higher order modelling approach to predicting shock-buffet. Deck's motivation behind proposing the ZDES was to eliminate the meshing constraints that DES required in order to avoid "grid-induced separation". Shock-buffet was captured successfully at $M_\infty = 0.73$, $Re = 3$ million, and $\alpha = 3.5°$ by the ZDES approach. The URANS and DES approaches only captured shock-buffet at incidences $\alpha = 4.5$ and $4.0°$ respectively. Although the frequency of the oscillation computed by ZDES was 73 Hz (5% overpredicted), the position of the shock and magnitude of unsteadiness in the separated boundary layer region were badly predicted. Deck also produced additional arguments in favour of Lee's acoustic wave propagation mechanism (see Fig. 2.26) of the shock-buffet phenomenon by computing convection velocities similar in value to what the experiments of Jacquin *et. al.* [23] have shown.

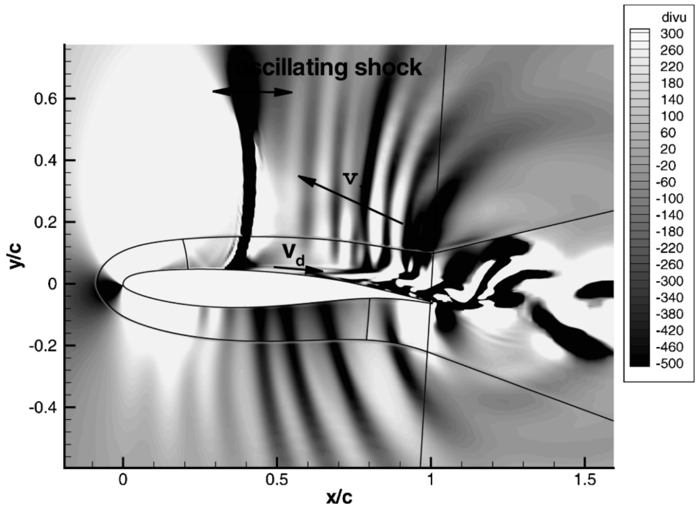

Fig. 2.26 Velocity divergence fields computed by ZDES in [45]

Grossi *et. al.* [46] used URANS and Delayed DES (DDES) closed with the SA turbulence model. Both approaches predicted shock-buffet with an overprediction in the amplitude and frequency of oscillation. Huang *et. al.* [47] applied an Improved DDES (IDDES) [48]. In their results, the shock location was predicted further upstream than in the experiments with similar levels of oscillation. In [49], an Organised Eddy Simulation (OES) was successfully applied. The authors used Proper Orthogonal Decomposition (POD) to quantify the frequency response of the shock-buffet phenomenon that was predicted.

Wall Modelled Large Eddy Simulations (WMLES) were produced in [50] about the OAT15A aerofoil at $M_\infty = 0.73$, $Re = 3$ million, and $\alpha = 3.5°$. Compared to Wall Resolved LES (WRLES) computations, WMLES simulations are cheaper as, although LES model is used all the way to the wall, the inner boundary layer turbulence is modelled rather than calculated.

A summary of all the results obtained for the OAT15A test case is given in Fig. 2.27 and Table 2.1. The spectrum of results presented reveal the difficulty in producing an accurate prediction of shock-buffet with high fidelity CFD methods.

The V2C Dassault Aviation aerofoil was simulated at $M = 0.7$, $Re = 500,000$, and $\alpha = 4°$ using Direct Numerical Simulations (DNS); an effort by Zauner *et. al.* [53] to produce a better understanding of the mechanics involved in transonic flow of aircraft wings. Shock-buffet characteristics dominated by fluctuations at $St = 0.12$ and 0.5-0.6 were computed. Figure 2.28 shows an instantaneous snapshot of their results via numerical Schlieren technique. The authors describe the mechanics of boundary layer transition via Kelvin-Helmholtz

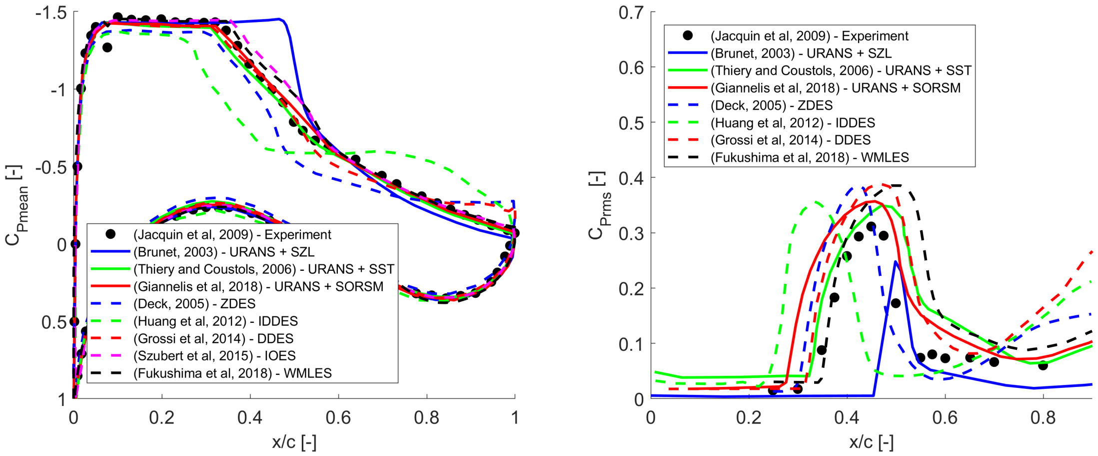

(a) mean C_P values **(b)** C_{PRMS} values

Fig. 2.27 Comparison of mean and RMS pressures observed in experiments of [23] and numerical studies of [37], [45], [41], [47], [51], [49], [50], and [52]. Figure compiled by the author using data readily available in the aforementioned publications.

Table 2.1 Comparison of results obtained for the OAT15A in shock-buffet regime

Source	Approach	Frequency (Hz)
Jacquin *et. al.* [23]	**Experiment**	**69**
Brunet [37]	URANS + SZL	74
Deck [45]	ZDES	70
Thiery and Coustols [41]	URANS + SA / SST / KKL	71-78
Huang *et. al.* [47]	IDDES	78
Grossi *et. al.* [51]	DDES	80.5
Szubert *et. al.* [49]	I-/OES	78.1
Fukushima *et. al.* [50]	WMLES	70
Giannelis *et. al.* [52]	URANS + SST / SORSM	72 - 75

instabilities and revealed two dominant oscillations present during shock-buffet. A high frequency oscillation, mainly observed due to the separated boundary layer was found at $St = 0.5 - 0.6$. A second dominant mode of oscillation, present at the location of the shock-wave was identified to have a frequency corresponding to $St = 0.12$.

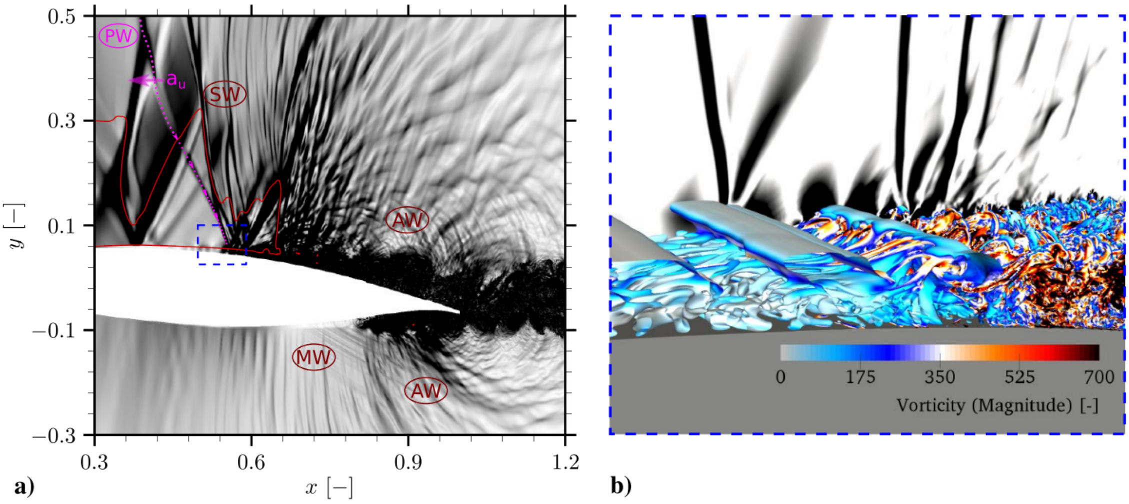

Fig. 2.28 Numerical Schlieren and Q-criterion isosurfaces computed in [53]

2.4.5 3D numerical predictions of shock-buffet

Iovnovich and Raveh [35] simulated 3D wings based on the RA16SC1 aerofoil. The simulations were run using an URANS approach closed with the SAE (SA turbulence model with Edwards modification) [54]. The freestream conditions were set as $M_\infty = 0.84$, $Re_{mac} = 20$ million. The validation performed in their study revealed that URANS simulations needed increased values of M_∞, Re_{mac}, and α to produce shock buffet, when compared to wind tunnel tests. Sweep angle (Λ) effects were investigated using infinite swept wings. Aspect Ratio (AR) was varied between 2 - 7.7 in finite wings to understand the wingtip effects.

Iovnovich and Raveh found that, for infinite wings, increasing the sweep angle can have a significant impact on the mechanics of the shock-buffet phenomenon. At low Λ, the three-dimensionality of shock-buffet is governed by areas of large shock-strength where shock-induced separation appeared. At $20° < \Lambda < 30°$, a periodic three-dimensionality appeared, with the main feature being a wavy shock front and multiple separation bubbles. The highest $\Lambda = 40°$ tested, the wing was completely stalled due to significant shock-induced lateral separation. The sweep angle effects can be visualised in Fig. 2.29. The observation of the sweep angle effects resulted in the authors to conclude that: at low sweep angle, shock-buffet resembles 2D buffet where the oscillations occur mainly in the chordwise directions; at high sweep angle ($\Lambda > 20$) the shock-buffet phenomenon is driven by a lateral (spanwise) shock-oscillation which locally gives birth to a 2D buffet-like phenomenon. They pioneered the term of *buffet cells* to describe this spanwise waviness of the shock coupled with bubbles of shock-induced separated boundary layer.

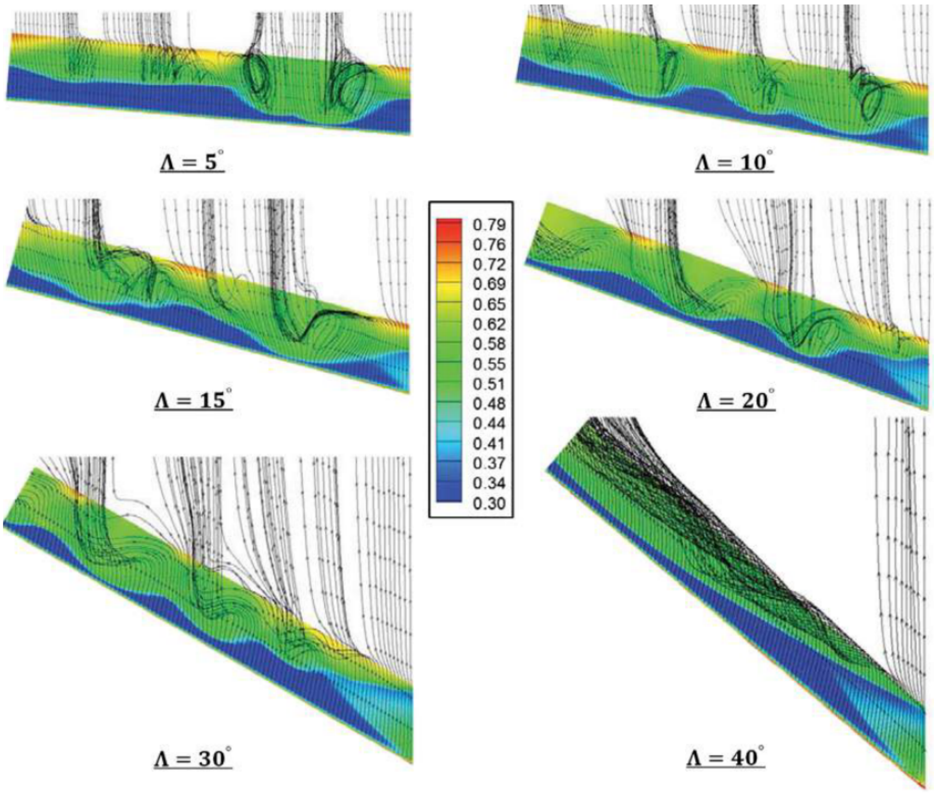

Fig. 2.29 Effect of sweep angle on three-dimensionality of shock buffet observed via C_P contours and streamlines [35]

The effect of AR was also investigated in [35]. The authors found that a low $AR = 3-4$ will result in the wing tip vortex interacting with the spanwise waviness described above, resulting in a more complex shock-buffet phenomenon. This phenomenon is dominated by higher fluctuation levels (C_{Prms}) towards the outboard of the wing (See Fig. 2.30). At $AR > 4$, the effect of the wingtip vortex on shock-buffet diminishes.

The RBC12 wing-body aircraft configuration was simulated by Sartor and Timme in [55], [56] and [57]. In [56], the M_∞ effect on buffet was investigated by simulating the aircraft using URANS closed with the SA turbulence model and an EARSM in the form of a realizable quadratic eddy viscosity model (RQEVM). The RQEVM provided additional modelling of turbulence compared with SA. M_∞ was varied between 0.76 and 0.84, Re_{mac} was maintained constant at 3.75 million. The effects of M_∞ were quantified in terms of shock-buffet onset incidence (α_{onset}), evolution of fluctuation magnitude observed in C_L, and frequency content.

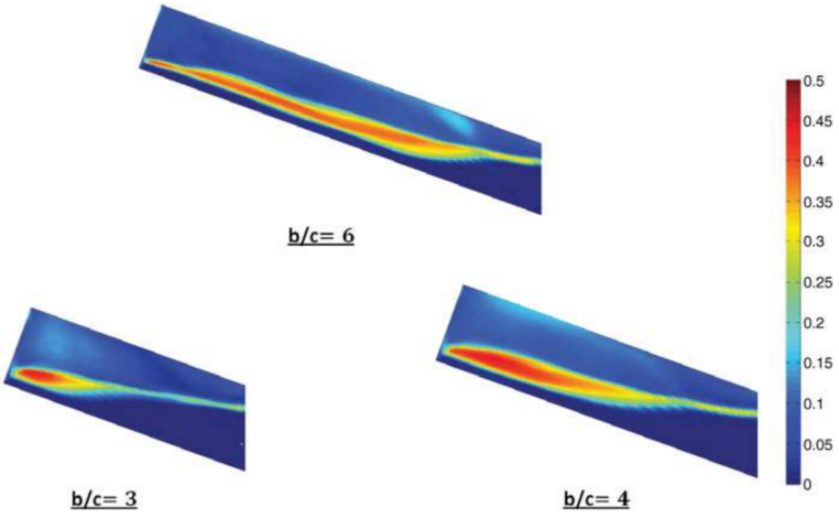

Fig. 2.30 Effect of Aspect Ratio on fluctuation levels (C_{Prms}) in shock-buffet regime [35]

Sartor and Timme found that as M_∞ increases, α_{onset} decreases. At lower Mach numbers, the fluctuation in C_L was seen to increase with increase in incidence whereas at high Mach numbers, the fluctuation remained small and reached a plateau value soon after onset. The frequencies computed by Sartor and Timme were in the range of St 0.1 to 0.4.

In [57] SA-based URANS and DDES simulations about the RBC12 aircraft at $M_\infty = 0.8$, $Re_{mac} = 3.75$ million and $\alpha = 3.8°$ were produced. Sartor and Timme investigated the effect of discretization schemes. They found that a 1st order upwind Roe discretization scheme was favourable for the SA turbulence model to capture shock-buffet. Comparison with data obtained in previous wind tunnel campaigns was possible. Similarities were found between experiments, URANS and DDES results in terms of shock position, unsteadiness and magnitude of fluctuation. The DDES simulation captured more details with regards to the structures developing in the unsteady shock-induced separation as can be seen in Fig. 2.31. In the URANS results, the waviness in the shock front and the buffet cells were more visible than in the DDES results.

Reynolds number effects on the RBC12 aircraft were presented by Masini *et. al.* [58]. The wind tunnel-sized and full scale aircraft were simulated at $Re_{mac} = 3.75$ and 27 million. Masini *et. al.* found that the shock-buffet topology is similar at the two values of Re_{mac}, however, an increase in Re_{mac} resulted in a lower load fluctuation over the aircraft.

The NASA CRM wing-body was simulated using the ZDES approach in Refs. [59] and [60]. Both studies revealed difficulties in getting accurate shock-buffet predictions using this

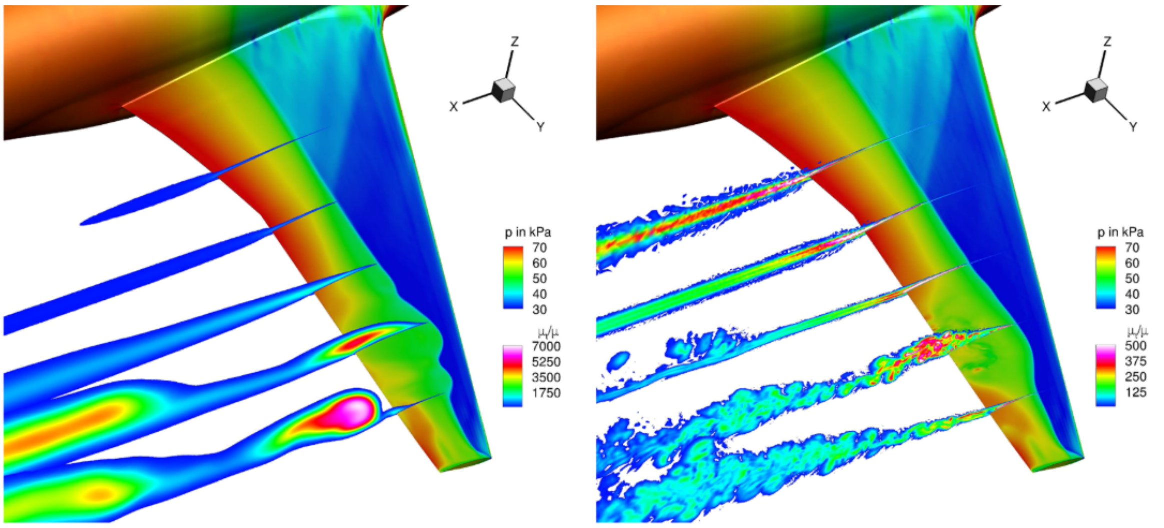

a) URANS **b) DDES**

Fig. 2.31 Surface C_P contours and slices of instantaneous eddy-viscosity (μ_t) computed in [57] via URANS and DDES

approach. Some potential was observed by an SA-based ZDES approach with a wall function. In their latest developments, Ohmichi *et. al.* [61] produced a modal analysis of shock-buffet on the NASA CRM. Although only a qualitative comparison with the experiments was possible, the authors showed the applicability of modal decomposition to produce visualisations of dominant oscillation modes during shock-buffet.

Timme [62] has also simulated the NASA CRM at $M_\infty = 0.85$, $Re_{mac} = 5$ million, and $\alpha = 3.5 - 3.85°$ using the URANS approach closed with SA turbulence model. The focus was on prediction of shock-buffet onset and investigation of the global instability shock-buffet mechanism proposed by Crouch *et. al.* in [63].

The literature only contains a limited number of numerical studies on 3D configurations.

2.5 Conclusions

In this chapter, the field of transonic aerodynamics, with focus on shock-buffet, was introduced. During transonic flight, aircraft experience simultaneous subsonic and supersonic airflow in the vicinity of their aerostructures. The inherited presence of a shock wave results in shock wave/boundary layer interactions (SWBLI) which can lead to shock-induced boundary layer separation or shock-buffet at high Mach numbers and high incidences. The need to guarantee a safe manoeuvrability of aircraft makes it essential to be able to capture shock-buffet onset margins and to produce a detailed characterisation of shock-buffet development past its onset.

A selection of previous experimental investigations revealed particularities of this phenomenon: effect of freestream conditions, typical frequencies of oscillation, or potential geometrical factors that can have an influence on it. With advance in Computational Fluid Dynamics (CFD), high fidelity unsteady Reynolds-averaged Navier-Stokes (URANS) and higher order modelling approaches have been applied to some 2D and 3D configurations.

This chapter highlighted that there are still challenges in trying to produce an accurate prediction of shock-buffet by means of URANS. In particular, the variation in the results compiled for 2D shock-buffet predictions in Fig. 2.27 and Table 2.1 reveal an uncertainty in applying eddy-viscosity based turbulence models to this problem. Only a few numerical attempts have been published with regards to shock-buffet in 3D aircraft configurations. A gap in knowledge was found as no published work addressed the use of the full Reynolds Stress Model in shock-buffet predictions.

To end this chapter, the reader is also referred to the reviews of Lee [64] and Giannelis *et. al.* [65] which contain a more in-depth analysis of all published work in the field.

Chapter 3

Computational strategy

3.1 Introduction

Computational Fluid Dynamics (CFD) and other computational methods play a key role in the design and investigation of aircraft aerodynamics. Although by all-means it is still not able to 100% replace the use of wind-tunnels and other experimental techniques, CFD provides the designer / researcher with a powerful tool. And with the recent development in the areas of *High Performance Computing* (HPC), CFD is being used more intensively during the design process.

In this chapter the computational strategy of this project is described. The mathematical background and numerical approaches are introduced and explained. A summary of the various software, and techniques implemented within is included at the end of the chapter.

To avoid confusion with other symbols used in the thesis, all symbols from this chapter are defined herein and some of them are not included in the Nomenclature if they overlap with others which may have other meaning in general.

3.2 Governing equations of fluid flow

In the process of simulating fluid flow via CFD, the three fundamental laws of nature must be considered:

- The conservation of mass
- Newton's second law of motion: *F=ma* (the conservation of momentum)
- The conservation of energy

By using CFD, mathematical statements of the three fundamental laws of nature are solved using various techniques over small parts of the fluid flow domain referred to as *control volumes*. These numerical statements are commonly known as the *Navier-Stokes* equations which are given in conservative, vectorial form in Equations 3.1-3.6. The equations in the following paragraphs are taken from [66].

$$\frac{\partial}{\partial t}\iiint_V \vec{W} dV = -\iint_{\partial V} \overline{\overline{F}} \cdot \vec{n} dS \tag{3.1}$$

where

$$\vec{W} = \begin{Bmatrix} \rho \\ \rho u \\ \rho v \\ \rho w \\ \rho E \end{Bmatrix} \tag{3.2}$$

and

$$\overline{\overline{F}} = (\vec{F}_i^c + \vec{F}_v^c) \cdot \vec{e}_x + (\vec{G}_i^c + \vec{G}_v^c) \cdot \vec{e}_y + (\vec{H}_i^c + \vec{H}_v^c) \cdot \vec{e}_z \tag{3.3}$$

with

$$\vec{F}_i^c = \begin{Bmatrix} \rho u \\ \rho u^2 + p \\ \rho uv \\ \rho uw \\ \rho Hu \end{Bmatrix}, \vec{F}_v^c = - \begin{Bmatrix} 0 \\ \tau_{xx} \\ \tau_{xy} \\ \tau_{xz} \\ u\tau_{xx} + v\tau_{xy} + w\tau_{xz} + q_x \end{Bmatrix}, \tag{3.4}$$

$$\vec{G}_i^c = \begin{Bmatrix} \rho v \\ \rho uv \\ \rho v^2 + p \\ \rho vw \\ \rho Hv \end{Bmatrix}, \vec{G}_v^c = - \begin{Bmatrix} 0 \\ \tau_{xy} \\ \tau_{yy} \\ \tau_{yz} \\ u\tau_{xy} + v\tau_{yy} + w\tau_{yz} + q_y \end{Bmatrix}, \tag{3.5}$$

$$\vec{H}_i^c = \begin{Bmatrix} \rho w \\ \rho uw \\ \rho vw \\ \rho w^2 + p \\ \rho Hw \end{Bmatrix}, \vec{H}_v^c = - \begin{Bmatrix} 0 \\ \tau_{xz} \\ \tau_{yz} \\ \tau_{zz} \\ u\tau_{xz} + v\tau_{yz} + w\tau_{zz} + q_z \end{Bmatrix}. \tag{3.6}$$

$\vec{W}$ is the vector of conserved quantities, $\overline{\overline{F}}$ is the flux density tensor composed of the viscous ($\vec{F}_v^c$, $\vec{G}_v^c$, and $\vec{H}_v^c$) and inviscid ($\vec{F}_i^c$, $\vec{G}_i^c$, and $\vec{H}_i^c$) flux vectors in the three Cartesian directions. ρ, u, v, w, p, and E denote the density, the Cartesian velocity components, static pressure, and total internal energy. The shear stresses (τ) and and heat fluxes (q) in the viscous fluxes are given in the Eq. 3.7 - 3.12 and Eq. 3.13.

$$\tau_{xx} = 2\mu \frac{\partial u}{\partial x} + \lambda \left(\frac{\partial u}{\partial x} + \frac{\partial v}{\partial y} + \frac{\partial w}{\partial z} \right) \tag{3.7}$$

$$\tau_{yy} = 2\mu \frac{\partial v}{\partial y} + \lambda \left(\frac{\partial u}{\partial x} + \frac{\partial v}{\partial y} + \frac{\partial w}{\partial z} \right) \tag{3.8}$$

$$\tau_{zz} = 2\mu \frac{\partial w}{\partial z} + \lambda \left(\frac{\partial u}{\partial x} + \frac{\partial v}{\partial y} + \frac{\partial w}{\partial z} \right) \tag{3.9}$$

$$\tau_{xy} = \tau_{yx} = \mu \left(\frac{\partial u}{\partial y} + \frac{\partial v}{\partial x} \right) \tag{3.10}$$

$$\tau_{xz} = \tau_{zx} = \mu \left(\frac{\partial u}{\partial z} + \frac{\partial w}{\partial x} \right) \tag{3.11}$$

$$\tau_{yz} = \tau_{zy} = \mu \left(\frac{\partial v}{\partial z} + \frac{\partial w}{\partial y} \right) \tag{3.12}$$

where μ is the viscosity modelled using the Sutherland law and $\lambda = -\frac{2}{3}\mu$.

$$q_x = \mathscr{K} \frac{\partial T}{\partial x}, q_y = \mathscr{K} \frac{\partial T}{\partial y}, \textit{ and } q_z = \mathscr{K} \frac{\partial T}{\partial z} \tag{3.13}$$

where T is the temperature, and $\mathscr{K}$ is the thermal conductivity.

To close the equations, pressure p is calculated using the equation of state:

$$p = \rho R T = (\gamma - 1)\rho \left(E - \frac{u^2 + v^2 + w^2}{2} \right) \tag{3.14}$$

with γ and R the specific heat ratio, and gas constant respectively.

3.3 The RANS problem

3.3.1 What are the RANS equations

Direct Numerical Simulations (DNS) of turbulent flows are expensive and not appropriate for industrially relevant flows. As such, to account for the turbulent nature of high *Re* flows, a Reynolds decomposition [67] can be applied to the full NS equations to split flow quantities (e.g. x-velocity, u) into the mean ($\bar{u}$) and fluctuating (u') components (see Eq. 3.15).

$$u(\vec{x},t) = \bar{u}(\vec{x}) + u'(\vec{x},t) \; where \; \vec{x} = \begin{Bmatrix} x \\ y \\ z \end{Bmatrix} \tag{3.15}$$

A time-averaging can then be applied to produce the *Reynolds-Averaged Navier-Stokes* equations. During the process of averaging, new quantities, known as Reynolds stresses appear in the RANS equations. These Reynolds stresses, defined in Eq. 3.16 are, just like all the other flow quantities unknowns. Thus, the system, as it is, becomes unsolvable as there are more unknowns than equations (known as the RANS closure problem).

$$\mathscr{R}_{ij} = -\rho\overline{u'_i u'_j} \tag{3.16}$$

3.3.2 Turbulence modelling as a solution to the RANS problem

The solution to the RANS problem is to produce additional equations that provide a way to model, or calculate the unknown Reynolds stresses, $\mathscr{R}_{ij}$. Since the effect of the Reynolds stresses is similar to that of a shear stress, Boussinesq has proposed an approximation through which $\mathscr{R}_{ij}$ can be modelled [68].

The Boussinesq hypothesis introduces the concept of turbulent eddy viscosity μ_t. The RANS equations are updated to include the turbulent contributions as described in Eq. 3.17.

$$\mu_{tot} = \mu + \mu_t \; \lambda_{tot} = -\frac{2}{3}\mu_{tot} \tag{3.17}$$

The Reynolds stresses are then *modelled* using the Boussinesq approximation:

$$\mathscr{R}_{ij} = -\rho\overline{u'_i u'_j} = \mu_t\left(\frac{\partial\overline{u_i}}{\partial x_j} + \frac{\partial\overline{u_j}}{\partial x_i} - \frac{2}{3}\delta_{ij}\frac{\partial\overline{u_k}}{\partial x_k}\right) - \frac{2}{3}\delta ij\rho k \tag{3.18}$$

with δ_{ij} = 1 if $i = j$, and 0 if $i \neq j$.

A turbulence model is then used to provide transport equations for quantities that can be used to model the Reynolds stresses. Such eddy viscosity-based turbulence models can consist of 0, 1, 2, 3 or even 4 equations for quantities such as: turbulent viscosity (μ_t), turbulent kinetic energy (k), or specific dissipation rate (ω).

Throughout this project two main turbulence modelling approaches have been considered.

3.3.3 The k-ω Shear Stress Transport turbulence model

The k-ω Shear Stress Transport (SST) [43] turbulence model is a two-equation closure for the RANS equations. The two transport equations (see Eq. 3.19 - 3.20 calculate the turbulent kinetic energy (k), and the specific dissipation rate of eddy viscosity (ω).

The scope of this turbulence model is to combine the benefits of the Wilcox $k-\omega$ in the boundary layer with the benefits of the $k-\varepsilon$ in the regions outside it.

$$\frac{\partial \rho k}{\partial t} + \vec{\nabla}\cdot(\rho\vec{u}k) - \vec{\nabla}\cdot\big((\mu+\mu_t\sigma_k)\vec{\nabla}k\big) = \widetilde{\mathscr{P}} - \beta_k\rho k\omega \tag{3.19}$$

$$\frac{\partial \rho\omega}{\partial t} + \vec{\nabla}\cdot(\rho\vec{u}\omega) - \vec{\nabla}\cdot\big((\mu+\mu_t\sigma_\omega)\vec{\nabla}\omega\big) = \frac{\gamma\rho}{\mu_t}\mathscr{P} - \beta_\omega\rho\omega^2 + 2\sigma_{omega2}(1-F_1)\frac{\rho}{\omega}\vec{\nabla}k\cdot\vec{\nabla}\omega \tag{3.20}$$

where the coefficients $\phi \in \{\sigma_k, \sigma_\omega, \gamma, \beta_\omega\}$ are interpolated using

$$\phi = F_1\phi_1 + (1-F_1)\phi_2 \tag{3.21}$$

where $\phi_1 \in \{\sigma_{k1}, \sigma_{\omega1}, \gamma_1, \beta_{\omega1}\}$, and $\phi_2 \in \{\sigma_{k2}, \sigma_{\omega2}, \gamma_2, \beta_{\omega2}\}$ are the coefficients for $k-\omega$ (inside boundary layer), and $k-\varepsilon$ (outside boundary layer) model respectively.

The values for those coefficients have been set in [43] to:

$$\sigma_{k1} = 0.85,\ \sigma_{\omega1} = 0.5,\ \gamma_1 = 0.555556,\ \beta_{\omega1} = \beta_k\left(\gamma_1 + \frac{\sigma_{\omega1}\kappa^2}{\sqrt{\beta_k}}\right)$$

$$\sigma_{k2} = 1,\ \sigma_{\omega 2} = 0.857,\ \gamma_2 = 0.44,\ \beta_{\omega 2} = \beta_k\left(\gamma_2 + \frac{\sigma_{\omega 2}\kappa^2}{\sqrt{\beta_k}}\right)$$

with $\kappa = 0.41$, $\beta_k = 0.09$, the blending function F_1 is given by

$$F_1 = \tanh(arg_1^4),\ arg_1 = \min\left(\max\left(\frac{\sqrt(k)}{\beta_k \omega y}; \frac{500\nu}{y^2\omega}\right); \frac{4\rho\sigma_{\omega 2}k}{CD_{k\omega}y^2}\right) \tag{3.22}$$

$$CD_{k\omega} = \max\left(2\rho\sigma_{\omega 2}\frac{1}{\omega}\vec{\nabla}k\cdot\vec{\nabla}\omega; 10^{-20}\right) \tag{3.23}$$

Therefore, the F_1 function controls the blending between the $k-\omega$ and the $k-\varepsilon$ models. In the boundary layer, F_1 must be 1, whereas outside it should tend to 0.

The *shear-stress* correction introduced by Menter has the role of fixing the overprediction of the shear-stress by the $k-\omega$ baseline turbulence model. In this case:

$$\mu_t = \min\left(\frac{\rho k}{\omega}; \frac{a_1\rho k}{\bar{\Omega}F_2}\right) \tag{3.24}$$

with

$$F_2 = \tanh(arg_2^2),\ arg_2 = \max\left(2\frac{\sqrt{k}}{\beta_k\omega y}; \frac{500\nu}{y^2\omega}\right) \tag{3.25}$$

$$\bar{\Omega} = \sqrt{2\Omega:\Omega},\ \Omega_{ij} = 0.5\left(\frac{\partial u_i}{\partial x_j} - \frac{\partial u_j}{\partial x_i}\right) \tag{3.26}$$

a_1 = 0.31, the Bradshaw constant.

3.3.4 Second-order closures: the full Reynolds Stress Model

The main approach used in this project is to use a second-order closure. This implies providing transport equation for each of the 6 $\mathscr{R}_{ij}$. The resulting turbulence models are commonly referred to as the full Reynolds Stress Model (RSM). The advantage of this approach is the implied calculation of each individual component of the Reynolds stress matrix. The disadvantage comes at a greater computational cost, as more equations are being solved.

The Reynolds stress transport equation can generally be written as:

$$\frac{\partial(\overline{\rho}\mathscr{R}_{ij})}{\partial t}+\frac{\partial}{\partial x_k}\left(\overline{\rho}\mathscr{R}_{ij}\tilde{u}_k\right)=\overline{\rho}P_{ij}+\overline{\rho}\Pi_{ij}-\overline{\rho}\varepsilon_{ij}+\overline{\rho}D_{ij}+\overline{\rho}M_{ij} \tag{3.27}$$

with $\frac{\partial(\overline{\rho}\mathscr{R}_{ij})}{\partial t}$ local time derivative; $\frac{\partial}{\partial x_k}\left(\overline{\rho}\mathscr{R}_{ij}\tilde{u}_k\right)$ the convection of $\mathscr{R}_{ij}$; $\overline{\rho}P_{ij}$ the production term; $\overline{\rho}\Pi_{ij}$ pressure-strain correlation; $\overline{\rho}\varepsilon_{ij}$ dissipation term; $\overline{\rho}D_{ij}$ diffusion term; and $\overline{\rho}M_{ij}$ contribution due to fluctuating mass flux.

The $\tilde{u}$ term in equations above refers to the Favre averaged (or density weighted) velocity which is defined as $\tilde{u}=\frac{\overline{\rho u}}{\overline{\rho}}$. Density averaging velocity fields leads to a simpler expression when solving problems with large density variations such as transonic aerodynamics of aircraft. Since this turbulence model is intended for use in transonic aircraft simulations, this approach was found suitable by its creators.

In addition to the transport equations of all components of the Reynolds stresses (3 in 2D, 6 in 3D), the RSM will include an additional equation for a turbulent quantity, typically the scalar dissipation rate (ε), or specific dissipation rate (ω). This is used to provide an additional closure for the functions in the model that require further modelling.

In this project, two variations of RSM have been used. The SSG/LRR-g variation, used to compute the results in Chapter 6, is described in full detail below. A Linear-Pressure-Strain variation, present in Chapter 5 is briefly introduced too with emphasis on the key differences when compared to the SSG/LRR-g model.

The SSG/LRR-g RSM

The Speziale-Sarkar-Gatski / Launder-Reece-Rodi (SSG/LRR-ω) RSM was developed at DLR as a blend of the two original RSM models, acting as the LRR near-wall and like the SSG in the inviscid part of the flow [69]. In this study, the SSG/LRR-g variation presented in [70] is used. It contains a reformulation of the ω equation in the original SSG/LRR-ω. ω is replaced with $g=\sqrt{1/\omega}$.

The g variation of the SSG/LRR RSM was introduced as a solution to the problems the original model had in near-wall regions. The ω would become singular, introducing numerical errors, which were highly dependant on the near-wall grid resolution. By offering this transformation, it was observed that these problems were eliminated in the context of 2-equation $k-\omega$ turbulence models, and now, in the context of the full RSM [70].

From Eq. 3.27, the individual terms become:

- **production term**:

$$\overline{\rho}P_{ij} = -\overline{\rho}\mathscr{R}_{ik}\frac{\partial \widetilde{u}_j}{\partial x_k} - \overline{\rho}\mathscr{R}_{jk}\frac{\partial \widetilde{u}_i}{\partial x_k} \tag{3.28}$$

- **pressure-strain correlation term** is blended between that of the LRR near wall [71], and SSG outside the viscous boundary layer [72] using Menter's blending function, F_1 given in Eq. 3.22.

$$\begin{aligned}
\overline{\rho}\Pi_{ij} = &-\left(C_1\overline{\rho}\varepsilon + \frac{1}{2}C_1^{*,(SSG/LRR)}\overline{\rho}P_{kk}\right)\widetilde{b}_{ij} \\
&+C_2^{(SSG/LRR)}\overline{\rho}\varepsilon\left(\widetilde{b}_{ik}\widetilde{b}_{kj} - \frac{1}{3}\widetilde{b}_{mn}\widetilde{b}_{mn}\delta_{ij}\right) \\
&+\left(C_3^{(SSG/LRR)} - C_3^{*,(SSG/LRR)}\sqrt{\widetilde{b}_{mn}\widetilde{b}_{mn}}\right)\overline{\rho}\widetilde{k}\widetilde{S}^{*}_{ij} \\
&+C_4^{(SSG/LRR)}\overline{\rho}\widetilde{k}\left(\widetilde{b}_{ik}\widetilde{S}_{jk} + \widetilde{b}_{jk}\widetilde{S}_{ik} - \frac{2}{3}\widetilde{b}_{mn}\widetilde{S}_{mn}\delta ij\right) \\
&+C_5^{(SSG/LRR)}\overline{\rho}\widetilde{k}\left(\widetilde{b}_{ik}\widetilde{W}_{jk} + \widetilde{b}_{jk}\widetilde{W}_{ik}\right)
\end{aligned} \tag{3.29}$$

The dissipation rate, ε, is computed using:

$$\varepsilon = \frac{C_\mu \widetilde{k}}{g^2} \tag{3.30}$$

with C_μ = 0.09. The specific kinetic turbulent energy is related to the Reynolds stress tensor by:

$$\widetilde{k} = \frac{1}{2}\mathscr{R}_{ii} \tag{3.31}$$

All the coeficients in Eq. 3.29 are interpolated between the values in the LLR model (near wall), and the values in the SSG model (outside the viscous layer) using Menter's F_1 from Eq. 3.22:

$$\begin{aligned} C_i^{(SSG/LRR)} &= F_1\widehat{C}_i^{(LRR)} + (1-F_1)\widehat{C}_i^{(SSG)} \\ C_i^{*,(SSG/LRR)} &= (1-F_1)C_i^{*,(SSG)} \end{aligned} \tag{3.32}$$

The individual coefficients from LRR and SSG take the values of those from Table 3.1.

Table 3.1 Values of the coefficients in the SSG and LLR models that are used in the SSG/LRR pressure-strain term; $C_2^{(LRR)}$ = 0.52 .

-	$\widehat{C}_1$	$\widehat{C}_1^*$	$\widehat{C}_2$	$\widehat{C}_3$	$\widehat{C}_3^*$	$\widehat{C}_4$	$\widehat{C}_5$
SSG	3.4	1.8	4.2	0.8	1.3	1.25	0.4
LRR	3.6	0	0	0.8	0	$\frac{18C_2^{(LRR)}+12}{11}$	$\frac{-14C_2^{(LRR)}+20}{11}$

- **dissipation term**:

$$\overline{\rho}\varepsilon_{ij} = \frac{2}{3}\overline{\rho}\varepsilon\delta_{ij} \tag{3.33}$$

- **diffusion term**:

$$\overline{\rho}D_{ij} = \frac{\partial}{\partial x_k}\left[\left(\overline{\mu}\delta kl + D^{SSG/LRR}\overline{\rho}\mathscr{R}_{kl}g^2\right)\frac{\partial\mathscr{R}_{ij}}{\partial x_l}\right] \tag{3.34}$$

where $\overline{\mu}$ is the mean viscosity, and the diffusion coefficient varies between the values of it in the LRR and SGG models via:

$$D^{(SSG/LRR)} = F_1 \sigma^* + (1 - F_1) \frac{2}{3} \frac{C_s}{C_\mu} \tag{3.35}$$

with σ^* = 0.5, and C_s = 0.22.

- **fluctuating mass flux term** is neglected in this version of the RSM.

In addition to the $\mathscr{R}_{ij}$ transport equations, this turbulence model is closed by solving a transport equation for g. This equation is simply a reformulation of the ω equation in Menter's baseline $k - \omega$ turbulence model. ω is substituted with $1/g^2$. This results in:

$$\frac{\partial(\overline{\rho} g)}{\partial t} + \frac{\partial(\overline{\rho} g \widetilde{u}_k)}{\partial x_k} = \overline{\rho} P^g - \overline{\rho} \varepsilon^g + \overline{\rho} D^g + \overline{\rho} C_D^g + \overline{\rho} G^g \tag{3.36}$$

In a similar way to the previous equation, the terms above are defined as:

- **production term**:

$$\overline{\rho} P^g = \alpha_w \frac{g}{2\widetilde{k}} \overline{\rho} \mathscr{R}_{ik} \frac{\partial \widetilde{u}_i}{\partial x_k} \tag{3.37}$$

- **destruction term**:

$$\overline{\rho} \varepsilon^g = -\frac{1}{2} \beta_w \frac{\overline{\rho}}{g} \tag{3.38}$$

- **diffusion term**:

$$\overline{\rho} D^g = \frac{\partial}{\partial x_k} \left[(\mu + \sigma_w \overline{\rho} \widetilde{k} g^2) \frac{\partial g}{\partial x_k} \right] \tag{3.39}$$

- **cross-diffusion term**:

$$\overline{\rho} C_D^g = \sigma_d \overline{\rho} g^2 \min\left(\frac{\partial \widetilde{k}}{\partial x_k} \frac{\partial g}{\partial x_k}; 0 \right) \tag{3.40}$$

- and the additional **gradient term**:

$$\overline{\rho}G^{g} = -\frac{3}{g}(\mu + \sigma_w \overline{\rho}\widetilde{k}g^2)\frac{\partial g}{\partial x_k}\frac{\partial g}{\partial x_k} \tag{3.41}$$

The coefficients that appear in the equations above are set to those appearing in the ω equation of Menter's baseline $k-\omega$ turbulence model (see Table 3.2). They also blend between the viscous layer and freestream flow using Eq. 3.42.

$$\phi_i = F_1\phi_i^{inner} + (1-F_1)\phi_i^{outer} \tag{3.42}$$

Table 3.2 Values for the coefficients in the g transport equation.

i	α_w	β_w	σ_w	σ_d
outer	0.44	0.0828	0.856	2 σ_w
inner	0.5556	0.075	0.5	0

The Linear Pressure-Strain RSM

The Linear Pressure-Strain RSM is used as a RANS closure in Chapters 4 and 5, and based on the work of [73] [74]. The key differences between this variation of the RSM and the SSG/LRR-g lays in the linear modelling of the pressure-strain term, $\overline{\rho}\Pi_{ij}$.

The Stress-Omega RSM

Is another variation of the RSM turbulence model based on the LRR [71] RSM and Wilcox's $k-\omega$ turbulence model [75]. The Stress-Omega RSM (SORSM) is only used herein in Chapter 4.

3.4 Discretization approach

3.4.1 Finite Volume Method

The system of equations representing the conservation of mass, momentum, energy, and turbulent quantities, is impossible to solve analytically for the general fluid flow scenario. The CFD solvers used for this project use the Finite Volume Method (FVM) to solve the equations by integrating them over finite control volumes.

Let's consider the 3D, time-dependant, RANS equations described in the sections above closed with the SSG/LRR-g RSM, and re-written for a physical domain $\Omega(t) \subset \mathbb{R}^3$ with a boundary $\partial\Omega(t)$, a time-dependant coordinate $\vec{x}(t)$ and a velocity field $\vec{U}(\vec{x}(t),t)$. With:

$$\vec{U}(\vec{x}(t),t) = [u(\vec{x},t), v(\vec{x},t), w(\vec{x},t)]^T,\ and\ \vec{x}(t) = [x(t), y(t), z(t)]^T \tag{3.43}$$

Then, the equations, in integral conservative form can be written as:

$$\int\limits_{\Omega(t)} \frac{\partial \vec{W}}{\partial t} d|\Omega| + \int\limits_{\partial\Omega(t)} (\vec{F}_c \cdot \vec{n} - \vec{F}_v \cdot \vec{n}) d|\partial\Omega| = \int\limits_{\Omega(t)} \vec{Q} d\Omega \tag{3.44}$$

where $\vec{W}$ is the vector of state variables:

$$\vec{W} = [\rho, \rho u, \rho v, \rho w, \rho E, \rho\mathscr{R}_{11}, \rho\mathscr{R}_{12}, \rho\mathscr{R}_{13}, \rho\mathscr{R}_{22}, \rho\mathscr{R}_{23}, \rho\mathscr{R}_{33}, \rho g]^T \tag{3.45}$$

$\vec{F}_c$ is the vector of convective fluxes, $\vec{F}_v$ is the vector of diffusion fluxes, $\vec{n}$ is the unit normal, $|\partial\Omega|$ is the surface area surrounding the physical domain $\Omega(t)$ and $\vec{Q}$ are the source terms.

Equation 3.45 can be rewritten using Leibniz integral rule for the time-dependant terms and becomes:

$$\frac{d}{dt}\int\limits_{\Omega(t)} \vec{W} d|\Omega| + \int\limits_{\partial\Omega(t)} (\vec{F}_c \cdot \vec{n} - \vec{F}_v \cdot \vec{n} - \vec{W}\vec{\dot{x}} \cdot \vec{n}) d|\partial\Omega| = \int\limits_{\Omega(t)} \vec{Q} d|\Omega| \tag{3.46}$$

In a typical simulation, Eq. 3.46 is solved for every control volume in the fluid flow domain using various spatial and temporal discretization schemes. By applying the divergence theory, the residual, $\vec{R}$, is computed which gives the flux imbalance within the volume Ω as a function of the sum of fluxes that pass through the volume's boundary surfaces. $\vec{R}$ is a measure of numerical error in iterative methods, a reduction in $\vec{R}$ describing lower numerical errors.

3.5 Choice of Solvers

Two solvers are used to generate the results presented in this manuscript. The commercial ANSYS Fluent solver provided the framework to obtain the results in Chapters 4, and 5. The industrial standard DLR-Tau code, is used in Chapter 6.

The ANSYS Fluent code is the commercial CFD solver available at the University of Sheffield with an intuitive GUI and good integration with proprietary pre and post-processing tools.

The DLR-Tau is a code developed at the German Aerospace Center (DLR) [77]. It is the standard for simulation of aircraft aerodynamics, and well appreciated in the industrial and scientific communities. In this project, Tau is used to produce time-accurate simulations in shock-buffet regime of aircraft. A dual time-stepping scheme is used.

3.6 Hardware

The simulations presented herein were run on the following High Performance Computing HPC facilities: The University of Sheffield **Iceberg, ShARC,** and **Greengrid**; The German Aerospace Centre $C^2A^2S^2E^2$.

Chapter 4

Numerical prediction of 2D shock-buffet

4.1 Introduction

This chapter contains an attempt to predict shock-buffet on the OAT15A aerofoil test case described by the experiments of Jacquin *et. al.* [23]. A summary of other similar research was given in Section 2.4.4. The aim herein is to identify challenges associated with prediction of shock-buffet using the selected mathematical and numerical approaches; and to develop best practices with regards to preprocessing, running and post-processing of unsteady CFD simulations.

The OAT15A supercritical aerofoil geometry is shown in Fig. 4.1. It has a maximum t/c value of 12.3% and chord length of 0.23 m. The trailing-edge was maintained blunt and has a thickness of 0.5% chord. The aerofoil contains typical features of supercritical aerofoils: large leading-edge radius, a long flat plateau on the suction side, and maximum camber location towards the trailing-edge.

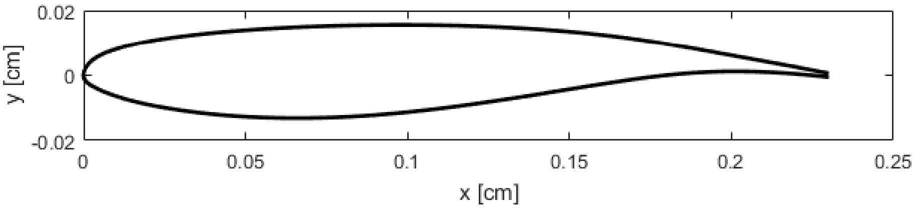

Fig. 4.1 The OAT15A aerofoil geometry

In [23] the shock-buffet regime observed at freestream conditions of $M_\infty = 0.73$, $Re_c = 3.0$ million and $\alpha = 3.5°$ is documented. Thus, the freestream conditions in the current project are set to be identical.

4.2 Numerical approach

4.2.1 Numerical grids

A family of grids consisting of 3 levels: L1, L2 and L3 is generated using the Pointwise meshing tool. The aerofoil is placed inside a C-H fluid domain with boundaries 50 chord lengths away. The grids are generated in two zones. The *extrude normal* feature of the tool is used to build a C-grid part and to maintain orthogonal quality near the surface of the aerofoil. The downstream zone is built using a multiblock approach. The domain indicating the two zones can be seen in Fig. 4.2.

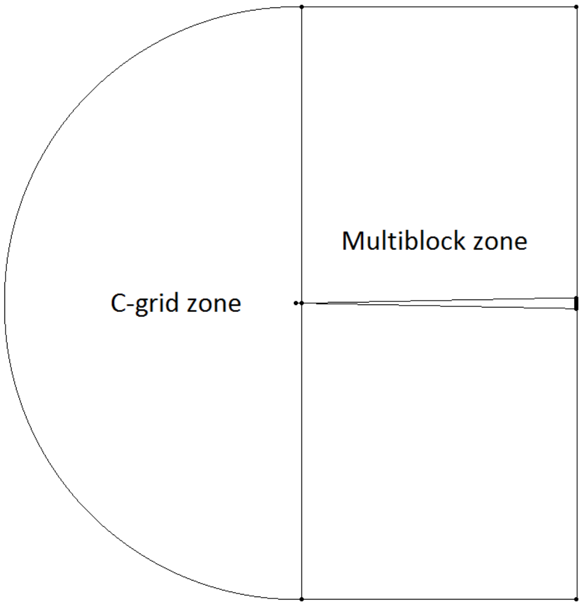

Fig. 4.2 Fluid domain around the OAT15A aerofoil

Refinement from one level to the next is performed by multiplying number of elements on each side of the aerofoil and the wake by 1.25; the growth rate of elements in the normal direction is reduced from 1.2 (L1) to 1.18 (L2) and 1.16 (L3); resulting in an increase in elements of approx. 50% compared to the previous level. This gives a consistent increase in cell density across the entire grid. The height of the first cell near the aerofoil boundaries in the L1 grid is selected such that y^+_{max} is 1. For L2 and L3, the height of the cell adjacent to walls is reduced by 1.25. Table 4.1 contains the exact values for each of the parameters described above.

Table 4.1 Characteristics of the three grids generated for the OAT15A aerofoil

Characteristic	Grid		
	L1	L2	L3
Cell count, *thousands*	43	68	95
Node count on aerofoil	249	386	483
Node count in normal direction	79	88	98
Node count in the wake	150	187	232
First cell height, m	$1.9 * 10^{-6}$	$1.5 * 10^{-6}$	$1.2 * 10^{-6}$
y^+ value	1	0.8	0.63

Figure 4.3 gives the farfield and close-up views of the L3 grid.

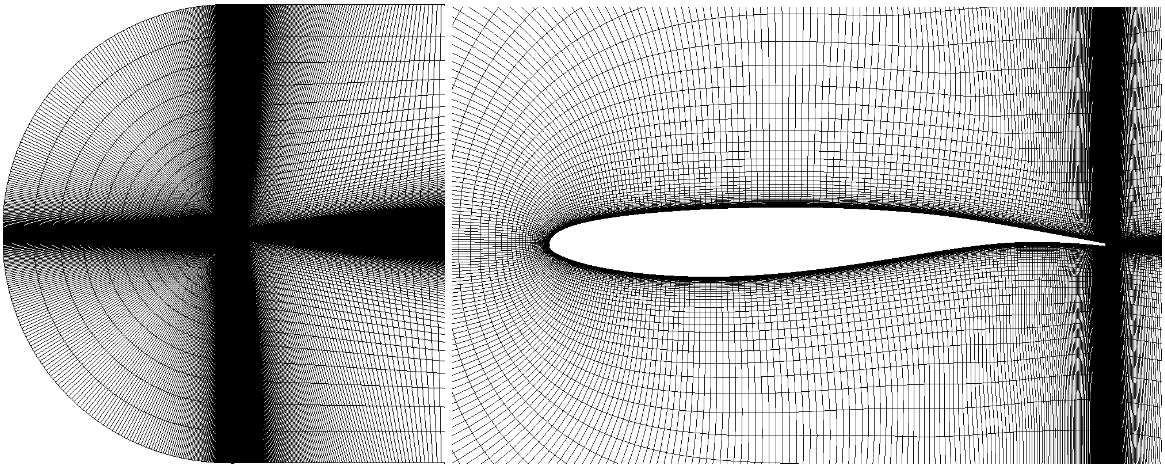

(a) farfield view **(b)** aerofoil close-up

Fig. 4.3 L3 grid around OAT15A generated using Pointwise

4.2.2 Solver

The Finite Volume Method (FVM) ANSYS Fluent CFD code is used in this chapter to produce time-accurate simulations of shock-buffet around the OAT15A aerofoil. Spatial discretisation is achieved using a second-order upwind Roe scheme, gradients are computed using a Least Squares Cell-Based method.

The URANS equations are solved using an implicit dual time-stepping method. The time step, Δt is set to $10\mu s$. It was chosen based on the convective time of a molecule over the aerofoil and will result in approx. 1500 time steps per buffet cycle. Similar values for Δt have been used in literature, in [52] a smaller timestep resulted in no significant change in shock-buffet prediction.

Residual convergence criteria was set to a value of 10^{-6} for all of the solved equations. A study was first performed in which the maximum number of inner iterations per timestep were set as 20, 60, or 100 to evaluate convergence levels. It was found that, compared with other equations, Residual levels for the continuity equation would not decrease more than 3 orders of magnitude, meaning that the solver would run the maximum number of iterations per timestep before proceeding to the next one. When assessing the time history of C_L, no difference was found between the simulations ran with a maximum of 60 or 100 inner iterations. As a results, a maximum of 60 inner iterations per timestep was found to be sufficient, even if the continuity Residual did not reach original convergence criteria. For future attempts, a better assessment of appropriate convergence criteria is recommended to reduce wasted computational time, however at the time of running these simulations, no further attempts to evaluate this were made.

Previous published research in the area of shock-buffet prediction by URANS approach concluded that the choice in turbulence model is essential in capturing shock-buffet dynamics. In Section 2.4.4, the literature surveyed revealed that there is an uncertainty in getting accurate prediction of shock-buffet on the OAT15A. For this reason, in this study, the most successful turbulence modelling approaches from previous studies are chosen.

First, an eddy-viscosity-based closure, the $k-\omega\ SST$ [43] was chosen based on the results of Thiery and Coustols [40] [41], Illi *et. al.* [78], and Giannelis *et. al.* [52].

Secondly, to avoid reliance on the Boussinesq approximation that eddy-viscosity-based turbulence models require, a second moment closure is used in project as well. The full

Reynolds Stress Model (RSM) models each individual Reynolds stress component with its own transport equation. It was less widely applied to shock-buffet predictions due to increase in computational cost associated with the increased number of equations being solved. When this project first started, only one study, by Illi *et. al.* [78] was published with positive conclusions with regards to the performance of the ε^h RSM [79] . Recently, a second study by Giannelis *et. al.* [52] also provided positive feedback for the Stress-Omega RSM (SORSM) [75].

ANSYS Fluent 18.2 includes four variations of the RSM turbulence model: the Linear Pressure-Strain (LPS) by Launder [73]; the Quadratic Pressure-Strain (also known as SSG) by Speziale, Sarkar and Gatski [72]; the Stress-Omega RSM (SORSM) which is based on the work of Launder, Reece and Rodi [71] and Wilcox's $k-\omega$ turbulence model [75]; and the Stress-BSL RSM which is a modified version of SORSM. Initial simulations performed in 2016 and not presented herein showed that the stability of the solver was sensitive to meshing strategy and numerical discretisation schemes, and at the time, shock-buffet could only be predicted using the Linear Pressure-Strain variation of the RSM. This is the reason why, this variation of the RSM remained the focus of our investigation. Following the publication of other RSM based results by Giannelis *et. al.* [52], the use of Stress-Omega variation of RSM is reconsidered on the latest set of grids.

Boundary conditions

Freestream boundary conditions at farfield were set for M_∞ = 0.73, P_∞ = 79500 Pa and T_∞ = 300K which resulted in an air density of $\rho = 0.92\ kg/m^3$. Viscosity was calculated using the Sutherland law. The value for *Re* was calculated as 3 million and matched the experiments. Incidence was varied by changing the appropriate components of the velocity. The turbulent intensity was set to 1%, and the turbulent length scale was set to 0.0161 m; based on the chord length and ANSYS guidelines.

At wall, a no-slip condition was selected. The experiments had the boundary layer tripped at a distance 7% chord from the leading edge. Previous numerical studies concluded that in numerical simulations, the tripping of the boundary layer does not have a significant impact on the results. Early simulations conducted during this research project confirmed this observation. Therefore, the simulations presented herein assume fully turbulent flow throughout the fluid domain. All turbulence models used in this study had low-Re settings, meaning that no wall functions were used.

4.3 Results

4.3.1 Mesh sensitivity

A mesh sensitivity study is conducted in the shock-buffet regime of the OAT15A at $M_\infty = 0.73$, $Re_c = 3$ million and $\alpha = 3.5°$. Simulations are run on all three grids, the URANS equations are closed by the $k-\omega$ SST and the Linear Pressure-Strain RSM. The boundary layer is not tripped. Time-accurate computed C_L is extracted and plotted for the last 0.1 seconds of simulated time in Fig. 4.4.

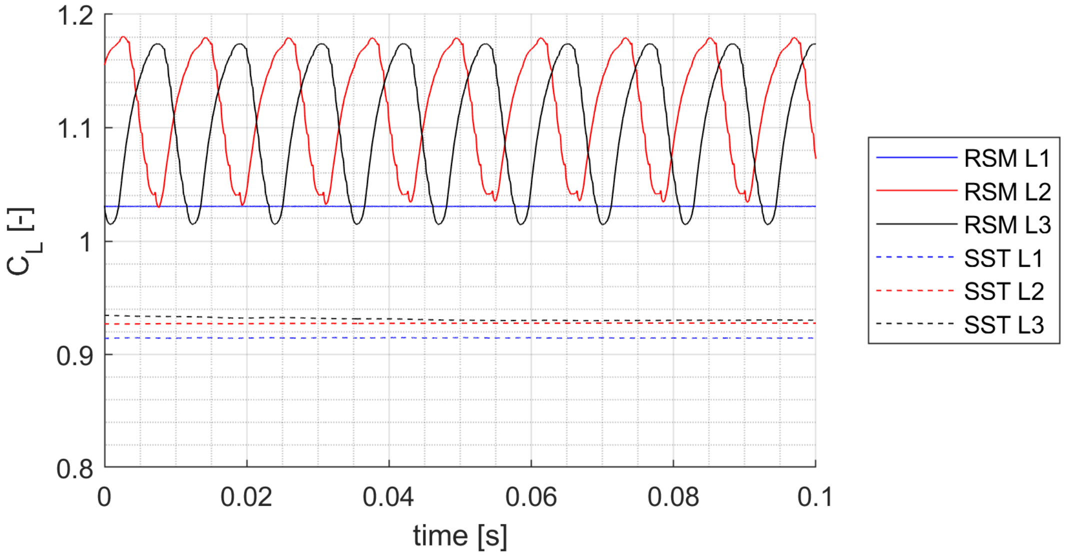

Fig. 4.4 Mesh sensitivity analysis on the computed time-accurate C_L of the OAT15A aerofoil at $M_\infty = 0.73$, $Re_c = 3$ million and $\alpha = 3.5°$

No unsteadiness is recorded in the simulations in which $k-\omega$ SST is used, the final C_L value varies insignificantly between L2 and L3 at a value of 0.93. The results obtained with the Linear Pressure-Strain RSM show different patterns. The L1 simulations converge to a steady-state and a $C_L = 1.03$. The results obtained on the L2 and L3 grids show a periodic oscillatory behaviour characteristic of shock-buffet. Figure 4.4 shows that the results computed on L2 and L3 seem to have different dominant frequencies of oscillation. For this reason, the Power Spectral Distribution (PSD) of the C_L signals are compared in Fig. 4.5. The frequency is given in non-dimensionalised Strouhal number, $St = fc/U_\infty$. It is clear that on the L2 grid there is no one frequency dominant, rather a broadband of frequencies that then converge into one on the more refined L3 grid.

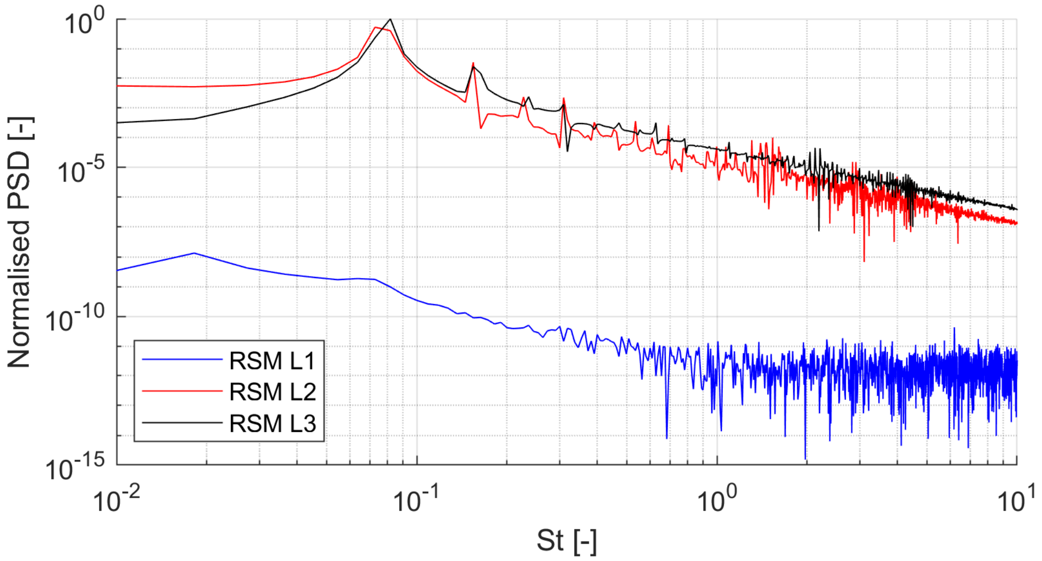

Fig. 4.5 Power spectral distributions of the C_L signals computed on the 3 grids

The values for C_{Lmean}, C'_{Lrms}, and St computed in the RSM-based simulations are given in Table 4.2. The value for C_{Lmean} does not change significantly between L2 and L3. There is an increase in C'_{Lrms} and the dominant St becomes clearer. It is believed that increasing the grid density further will not have a significant impact on the results. Therefore, the solution obtained on the L3 grid is considered mesh-independent.

Table 4.2 Computed C_L statistics across all three grids, results obtained by closing the URANS equations with the Linear Pressure-Strain RSM

-	L1	L2	L3
C_{Lmean}	1.03	1.12	1.11
C'_{Lrms}	0	0.05	0.056
St	0	0.072-0.081	0.081

4.3.2 Effect of turbulence modelling at $\alpha = 3.5°$

In this section, numerical results at $M_\infty = 0.73$ and $Re_c = 3$ million are compared with experiments. The periodic C_L shown in Fig. 4.4 is a typical indication of shock-buffet. Experiments by Jacquin *et. al.* [23] documented the characteristics of shock-buffet at these free stream conditions. The results presented in this section have been computed on the L3 grid. The URANS equations are closed with $k-\omega$ SST, Linear Pressure-Strain (LPS) RSM and the Stress-Omega (SO) RSM.

Fig. 4.6 re-iterates on the time-accurate C_L computed on the L3 grid by using the three different turbulence closures at freestream conditions of $M_\infty = 0.73$, $Re_c = 3$ million, and $\alpha = 3.5°$.

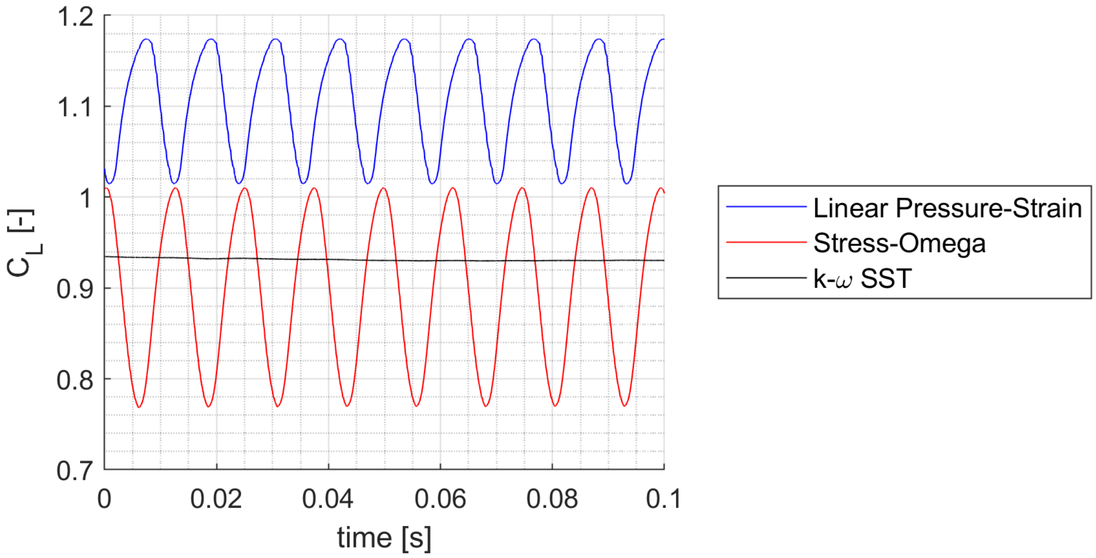

Fig. 4.6 Last 0.1 seconds of computed C_L by using the three turbulence models on the L3 grid

No oscillation is captured by the $k-\omega$ SST turbulence model. Periodic fluctuations are computed with both variations of the RSM model, however, the mean values and amplitude of fluctuation are visibly different between the two predictions. In particular, a lower C_{Lmean} and higher C'_{Lrms} is computed by the Stress-Omega RSM. Exact C_L data is not available from the experiments, thus pressure coefficient distributions are more relevant for discussing the accuracy of both models. Figures 4.7 and 4.8 give a comparison of computed time-accurate, mean and fluctuation amplitude in C_P with recorded experimental values; for the two variations of RSM. The computed power spectral distributions (PSD) at the location of peak $C'_{P_{rms}}$ are shown in Fig. 4.9

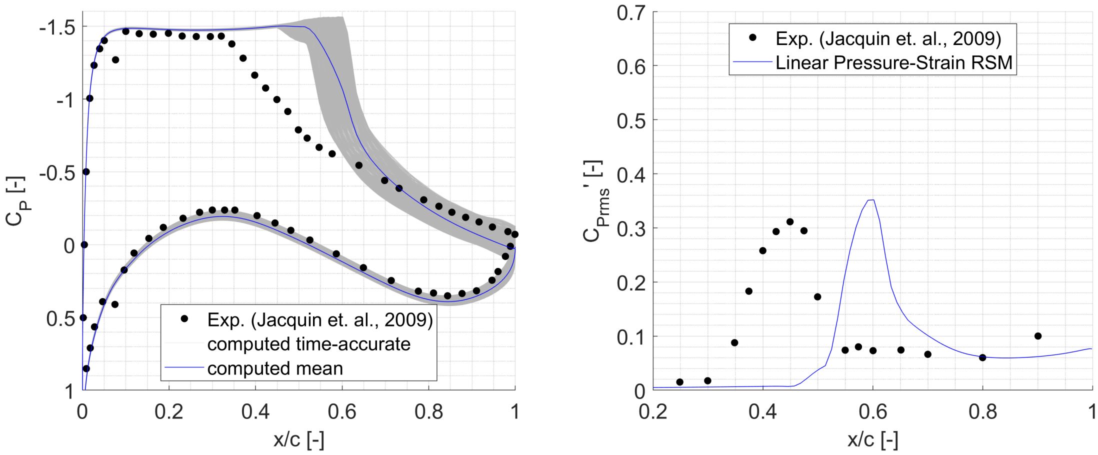

(a) time-accurate and mean

(b) fluctuation RMS

Fig. 4.7 Comparison between computed (with Linear Pressure-Strain RSM) and experimental C_P at $M_\infty = 0.73$, $Re_c = 3$ million, and $\alpha = 3.5°$

Figures 4.7 and 4.8 show the key differences in the prediction of shock-buffet with the two variations of RSM. The time-accurate C_P show large variation at shock position, coupled with unsteadiness downstream too. The pressure upstream of the shock is largely unaffected in the results computed with the Linear Pressure-Strain RSM, some fluctuation in the level of the pressure plateau is present in the Stress-Omega RSM results. Interestingly, the shock oscillation on the suction side of the aerofoil results in some change of loading on the pressure side too.

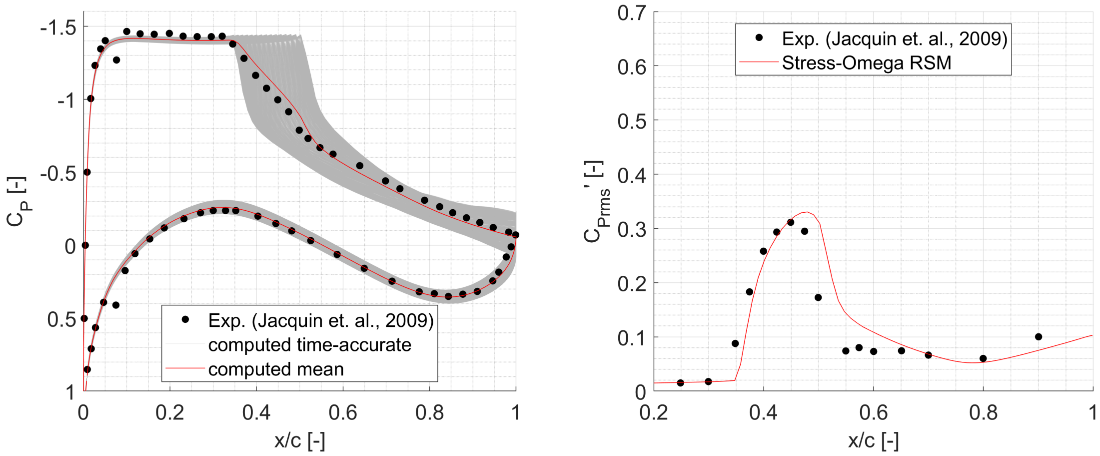

(a) time-accurate and mean **(b)** fluctuation RMS

Fig. 4.8 Comparison between computed (with Stress-Omega RSM) and experimental C_P at $M_\infty = 0.73$, $Re_c = 3$ million, and $\alpha = 3.5°$

Secondly, if we focus particularly on the shock strength that can be interpreted through how abrupt and how large the change in pressure occurs across the shock, the Linear Pressure-Strain RSM results indicate a weak compression wave occurs first, followed by the actual shock, particularly visible when the shock travels upstream. Analysis of velocity contour plots showed this may be due to an initial thickening and separation of the boundary layer predicted upstream of the shock.

The Linear Pressure-Strain RSM predicts a mean shock and peak pressure fluctuation, $C'_{Prms,peak}$, location of $x/c = 0.15$ more downstream than the experiments. In comparison, the Stress-Omega RSM accurately predicts the the mean shock location and hence the location of peak pressure fluctuation. The amplitudes of oscillation predicted by the two RSMs are similar in magnitude and reflect well the experiment. The spatial propagation of the pressure fluctuation is well predicted by the Stress-Omega RSM and is narrower in the results obtained with the Linear Pressure-Strain RSM.

The PSD of C_P at the location of peak fluctuation show that both simulations predict higher shock-buffet frequencies than experiment. In terms of St, the frequencies are overpredicted by 10% and 20% by the Stress-Omega RSM and the Linear Pressure-Strain RSM respectively.

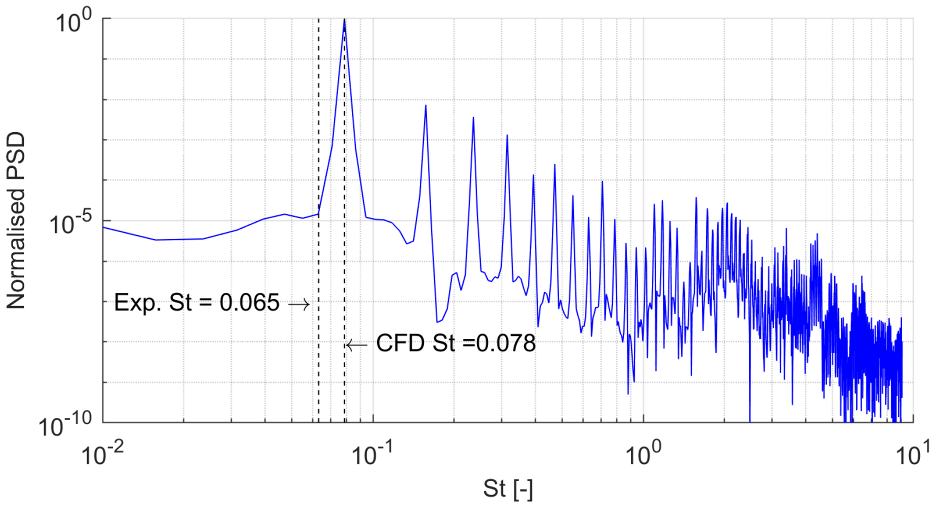

(a) Linear Pressure-Strain RSM

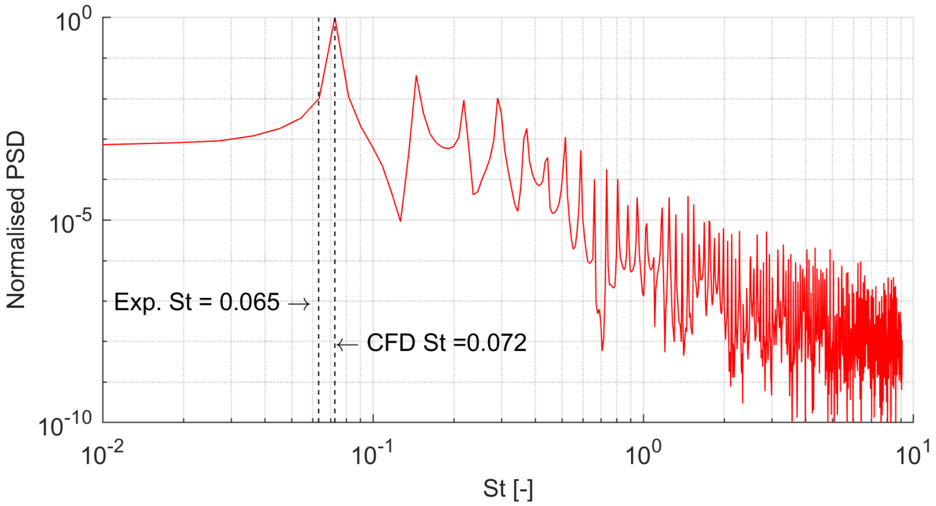

(b) Stress-Omega RSM

Fig. 4.9 Comparison between computed and experimental PSD of C_P at x/c = 0.45. Freestream $M_\infty = 0.73$, $Re_c = 3$ million, and $\alpha = 3.5°$

4.3.3 Prediction of shock-buffet envelope at $M_\infty = 0.73$ and $Re_c = 3$ million

In this section, the robustness of the two variations of RSM is tested. Simulations are ran at incidences $\alpha = 3.1$, 3.25, and 3.9° to assess whether either of the two RSM can accurately capture the whole buffet polar accurately, or at least the general trends observed in the experiments. A broader buffet envelope, covering a range of M_∞ and α was already published by Giannelis *et. al.* [52]. The authors produced URANS simulations closed with the Stress-Omega RSM, on a similar grid, and similar numerical parameters, thus a comparison between the two sets of computed data is possible.

The reasoning behind this section stems from previous reports that the RANS-based simulations closed with RSM can be inherently unstable, hard to converge or, sensitive to numerical parameters. Thus, although previously published in [52], this section adds an element of repeatability, and new knowledge with regards to the performance of the Linear Pressure-Strain RSM, which was not documented before.

Computed mean pressure coefficients (C_{Pmean}) and amplitude of fluctuation (C'_{Prms}) are shown in Figs. 4.10 and 4.11 for the two turbulence models. Table 4.3 gives the location ($x/c_{C_{Prms,peak}}$) and amplitude of maximum pressure fluctuation $C_{Prms,peak}$ in comparison with experiments and numerical results from [52].

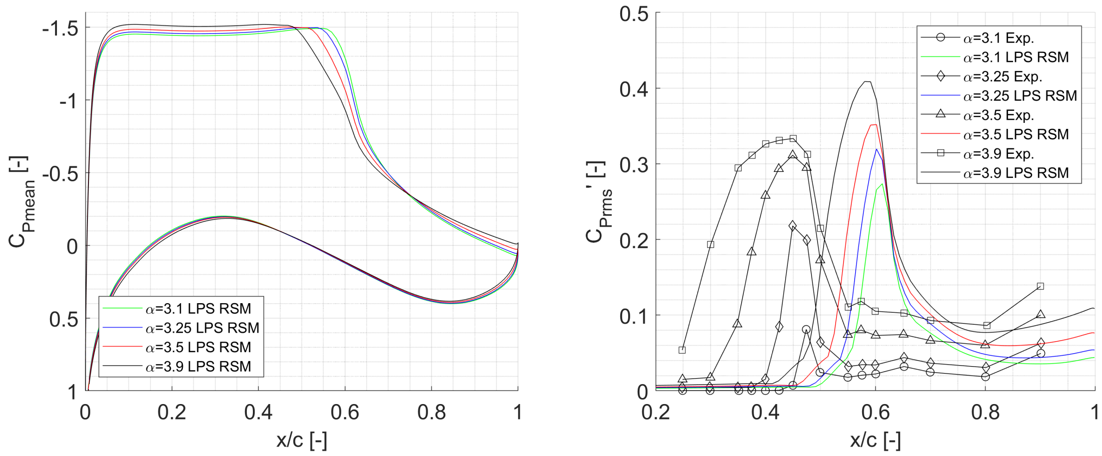

(a) mean pressure coefficient **(b)** RMS of fluctuation

Fig. 4.10 Comparison between Experimental and Linear Pressure-Strain (LPS) RSM computed pressure on the OAT15A at various incidences

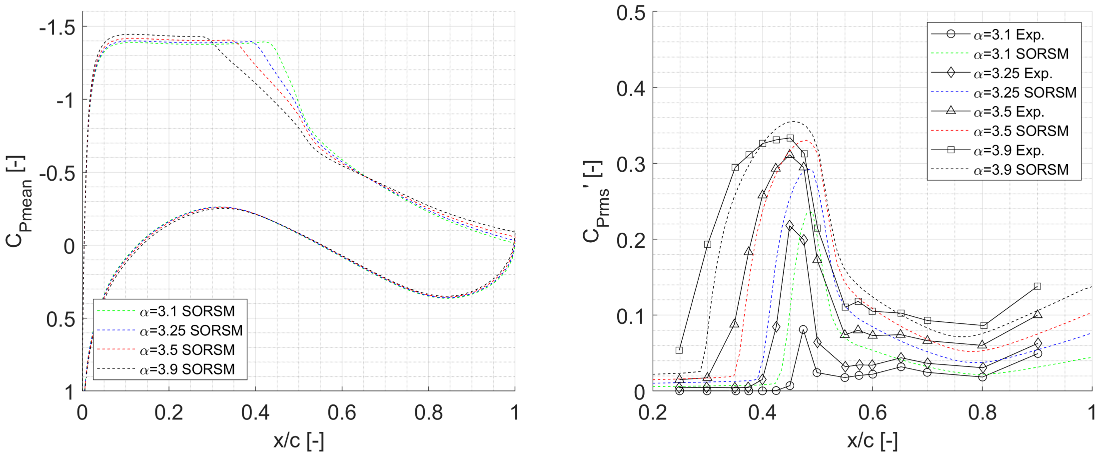

(a) mean pressure coefficient

(b) RMS of fluctuation

Fig. 4.11 Comparison between Experimental and Stress-Omega (SO) RSM computed pressure on the OAT15A at various incidences

From Figs. 4.10b and 4.11b, the amplitude of pressure fluctuation is predicted to increase with incidence. The Stress-Omega RSM captures well the location of high pressure fluctuation, whereas the Linear Pressure-Strain consistently predicted it further downstream. The location of the highest amplitude of fluctuation moves marginally towards the leading edge as the incidence is increased, the portion of aerofoil sustaining pressure fluctuation also increases, just like the experiments. This results in Figs. 4.10a and 4.11a, in a weaker adverse pressure gradient on the mean C_P. Neither of the two variants of the RSM model accurately predicted the significant decrease in C'_{Prms} at the lower incidence of $\alpha = 3.1°$.

Table 4.3 Comparison between current, literature computed, and experimental fluctuation characteristics at different incidences.

	$x/c_{C'_{Prms,peak}}$				$C'_{Prms,peak}$			
	3.1°	3.25°	3.5°	3.9°	3.1°	3.25°	3.5°	3.9°
Current, LPS RSM	0.61	0.6	0.6	0.58	0.27	0.32	0.35	0.4
Current, SO RSM	0.49	0.48	0.48	0.46	0.24	0.29	0.33	0.36
Giannelis *et. al.* [52], SO RSM	0.46	0.45	0.45	0.43	0.12	0.21	0.25	0.30
Jacquin *et. al.* [23], Exp.	0.47	0.45	0.45	0.45	0.08	0.21	0.31	0.33

Table 4.3 gives a quantitative comparison between the current CFD data, CFD data from [52], and the experimental values from [23]. It gives another interpretation of the observations made above. When comparing the current SO RSM results with those obtained by Giannelis *et. al.*[52], a discrepancy can be observed in both value and location of maximum C_P fluctuation, particularly at an incidence of $\alpha = 3.1°$. Although the mathematical modelling in both sets of results is similar (both sets of simulations were run on the same solver, with a similar meshing strategy, and identical mathematical model), it is believed that the discrepancies can be due to small differences in grids as well as numerical parameters which may have an impact on the final results.

4.4 Conclusions

A numerical study was performed to investigate the prediction of shock-buffet on the 2D OAT15A aerofoil test case first experimentally tested by Jacquin *et. al.* [23] at free stream conditions of $M_\infty = 0.73$ and $Re_c = 3$ million. The URANS-based simulations were performed on multi-block structured grids, three turbulence models were used as closures: $k-\omega$ SST, Linear Pressure-Strain Reynolds Stress Model (RSM), and Stress-Omega RSM. The aim was to assess potential benefits in prediction of shock-buffet when using RSM as an advanced URANS closure.

No shock-buffet was captured in the results computed with the $k-\omega$ SST turbulence model at an incidence $\alpha = 3.5°$; thus this eddy-viscosity based turbulence closure was discarded from any further investigation. On the other hand, the simulations ran with the two variations of the RSM, captured self-sustained, periodic shock oscillations easily identified through time history of C_L and C_P slices. When compared to experiments, the shock-buffet prediction with the Stress-Omega RSM agreed well with the experiments. Computed C_{Pmean}, amplitude and location of fluctuation correlated well with experimental values. On the other hand, results obtained with the Linear Pressure-Strain RSM presented an inaccurate shock position, resulting in a displacement of $x/c = 0.15$ from the experimental values. Both sets of results had frequencies of oscillation higher than the experimental one.

The robustness of the RSM was investigated by running simulations at different free stream incidences and assessing how well the RSM can predict the whole polar in shock-buffet.

The CFD results correlated well with experiments, the overall trends were well predicted although the computed amplitude of pressure fluctuation was higher than in the experiments.

Chapter 5

Off-design transonic aerodynamics of NASA CRM

Chapter 2, Section 2.4 describes shock-buffet as a type of periodic, unsteady Shock wave/boundary layer interaction (SWBLI), preceded by appearance of shock-induced separation. This chapter introduces simulations regarding the prediction of the onset and development of shock-induced separation by means of steady Reynolds-averaged Navier-Stokes (RANS) simulations. The aim is to complement the results already published for the AIAA CFD Drag Prediction Workshops, compare with experimental observations and produce guidelines as to how different turbulence modelling strategies cope with prediction of off-design transonic aerodynamics.

A wing-body geometry, relevant of today's commercial aircraft is selected and simulated at various flight incidences.

5.1 The NASA CRM aircraft

The wing/body/nacelle/pylon/horizontal-tail (WBNPH) NASA *Common Research Model*[1] (CRM) is the result of a collaboration aiming to produce an open, and up-to-date configuration that is representative of contemporary transonic aircraft. Its development is presented in

---

[1] for NASA CRM website see: https://commonresearchmodel.larc.nasa.gov/

Ref. [80], and was focused on aerodynamic design constraints typical to commercial aircraft. For example, 1.3g safety margin to buffet, design-point within 1% ML/D_{max}, appropriate sizing of the horizontal tail, etc. The wing was fitted on an existing fuselage representative of wide-body aircraft such as the Airbus A330 and Boeing B777. Nacelle and pylon were designed accordingly and sized based on a high bypass ratio engine. The WBNPH CRM is shown in Fig. 5.1, the resemblance with a typical transport aircraft is evident. Figure 5.2 shows the wing sections at 9 spanwise locations, revealing the intricate design of the supercritical transonic aerofoils that were used. Reference values for the wing are given in Table 5.1 in comparison with Airbus A330 and Boeing B777 to emphasise on the similarities.

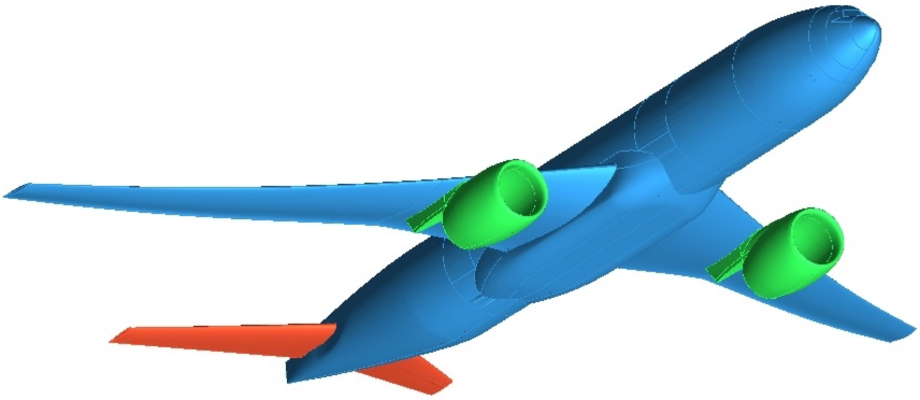

Fig. 5.1 The full NASA CRM configuration:wing-body, nacelle-pylon and horizontal tail

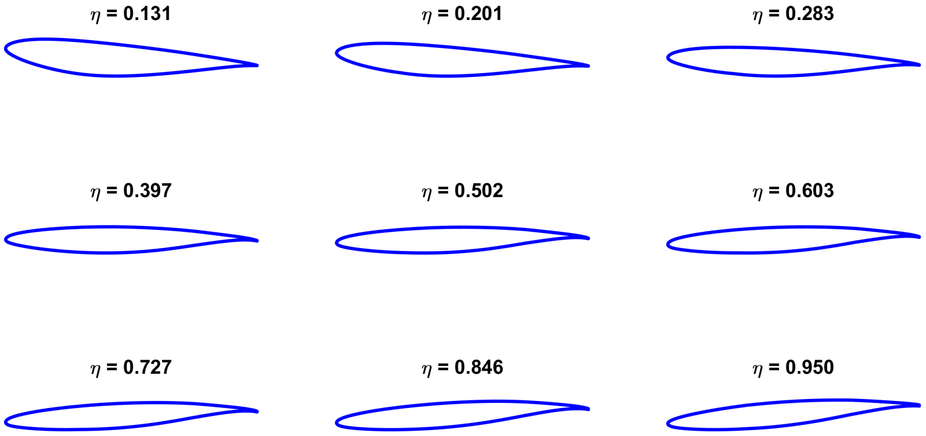

Fig. 5.2 The 2D wing sections of the CRM at different spanwise locations

The aircraft was first introduced as a blind test-case during the 4th *American Institute of Aeronautics and Astronautics* (AIAA) CFD *Drag Prediction Workshop*[2] (DPW) and has

---

[2] for AIAA CFD DPW website see: https://aiaa-dpw.larc.nasa.gov/

Table 5.1 The dimensions of the NASA CRM wing

Dimension	CRM	A330-300	B777-300
Ref. Area, m^2	389.76	363.10	427.80
Span, m	59.23	58	60.90
Ref. Chord, m	7.06	7.26	8.75
Aspect Ratio	9	9.26	8.67
Taper Ratio	0.275	0.251	0.149

since remained the test-case for the 5^{th} and 6^{th} AIAA CFD DPWs. The results have been since made available on the AIAA CFD DPW webpages and published in special editions / publications of AIAA Journal of Aircraft in comparison with experimental data [81] [82] [83] [84] [2]. The scatter of results from these workshops revealed that there are still difficulties in producing accurate predictions of transonic aerodynamics at off-design flight conditions. One of the most common issue was the overprediction of the *side-of-body* (SOB) separation at the trailing-edge of the wing-root; problem which is also interrogated herein.

Furthermore, during the 5^{th} AIAA CFD DPW, it was found that wind tunnel model deformations have an impact on the aerodynamics of the aircraft. Hence, to improve the accuracy of the CFD simulations, for the 6^{th} DPW, wind tunnel model deformations were measured (see Fig. 5.3) and applied to the CFD model to create a new family of geometries, one for each incidence[3] [85] [86]. The resulting family of geometries in Fig. 5.4 shows the significant wingtip bending and twisting as the incidence is increased.

5.2 Numerical approach

The *full-sized*, *deformed*, *wing-body* NASA CRM from the 6^{th} AIAA CFD DPW is used during this study. Two sets of results are obtained. The first aims to complement the results already published in [82] as part of the 6^{th} AIAA CFD DPW. The second set aims to investigate the *onset* and *development* of shock-induced boundary layer separation and the limitations of the current numerical approach.

---

[3] **NOTE:** As a terminology rule, for the remainder of the study, the deformed CRM geometries will be referred to as **aeX** where **ae** stands for aeroelastic deformations and **X** stands for the incidence at which the deformations applied were measured. For example, *ae250* is the CRM geometry which was deformed with the deformations measured at $\alpha = 2.5°$ incidence.

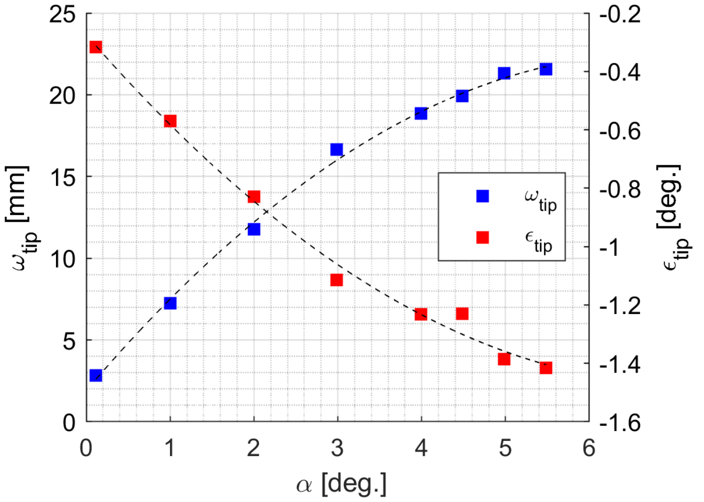

Fig. 5.3 Measured wing tip deflection (ω_{tip}) and twist (ε_{tip}) in the ETW wind tunnel [85]

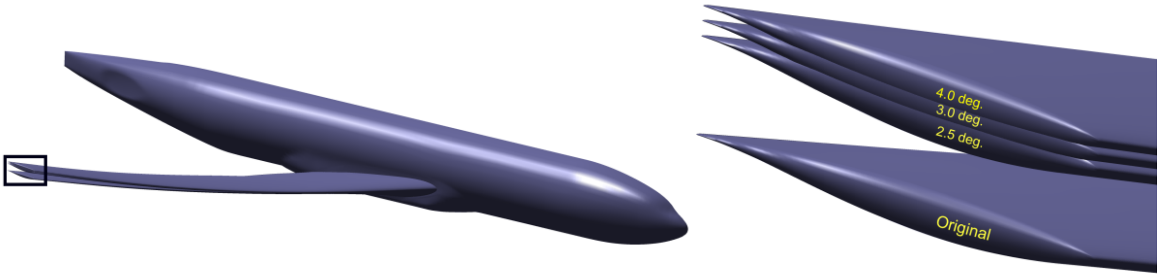

Fig. 5.4 Effect of wing deformation on the original NASA CRM

5.2.1 Numerical grids

A variety of grids for this geometry have been already made available on the AIAA CFD DPW website by the organising committee and their participants. For this research project however a new family of grids is developed based on the latest guidelines of the AIAA CFD DPW organising committee (see Table 5.2).

Table 5.2 Mesh generation guidelines provided by the AIAA CFD DPW organising committee

Guidelines	Coarse	Medium	Fine
Number of DOF, *million*	30	45	70
First cell height, *m*	$3.26 * 10^{-5}$	$2.83 * 10^{-5}$	$2.46 * 10^{-5}$
y^+_{avg}	1	0.87	0.76
Min. number of elements at TE	8	10	12
Growth rate at viscous wall		<1.2	
Farfield boundaries		100 * semi-spans away	

The first decision in building this family of grids was to choose between the different types: structured and unstructured. Results from the 5^{th} and 6^{th} AIAA CFD DPW revealed a greater variation between those obtained with unstructured grids and less between those obtained with structured grids [84][2]. Further advantages of structured grids include the ability to align elements with the flow direction, and much more control in surface element distribution and refinement in the vicinity of the areas of interest. This comes with a considerable more effort required to build the grids by comparison with unstructured grids. As such, it was decided that structured grids are most appropriate for this study. In this case, the grids evolved overtime before reaching the state presented in this chapter.

The *ICEM CFD* meshing software from *ANSYS* was used to generate the grids for this study. A multi-block structured approach is considered. The half wing-body aircraft is placed at the centre of a symmetry plane with a radius of 100 wing semi-spans. The domain takes the shape of a semi-sphere with the aircraft in the centre (see Fig. 5.5). Common structured grids around aerofoil / aircraft type geometries include C-, O-, or H-grid types exemplified in Fig. 5.6 below.

The blocking structure in ICEM CFD refers to the edges along which element distribution can be manipulated. They were built from the outside towards the inside followin the O-grid strategy. The final grids contain over 180 blocks which can be adjusted to produce the final grid. Figure 5.7 shows the details of this blocking structure. The blocks were initially

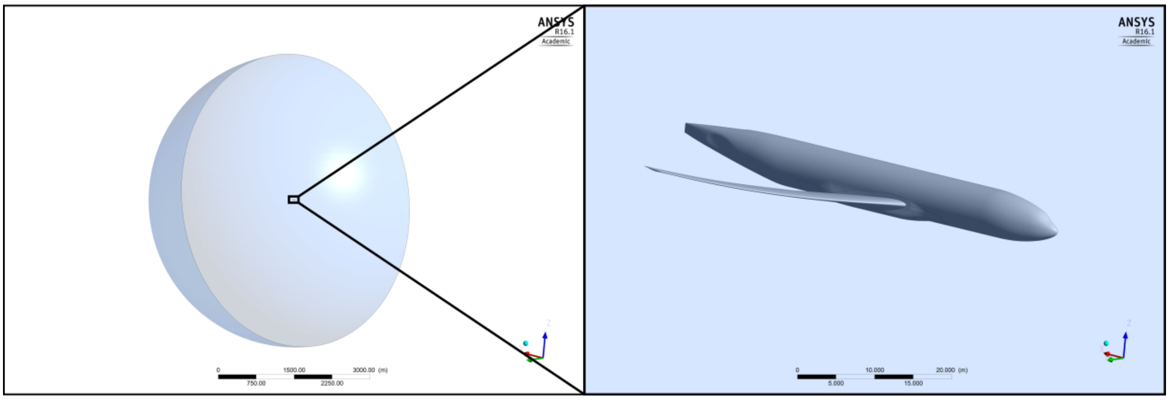

Fig. 5.5 Fluid domain around the NASA CRM

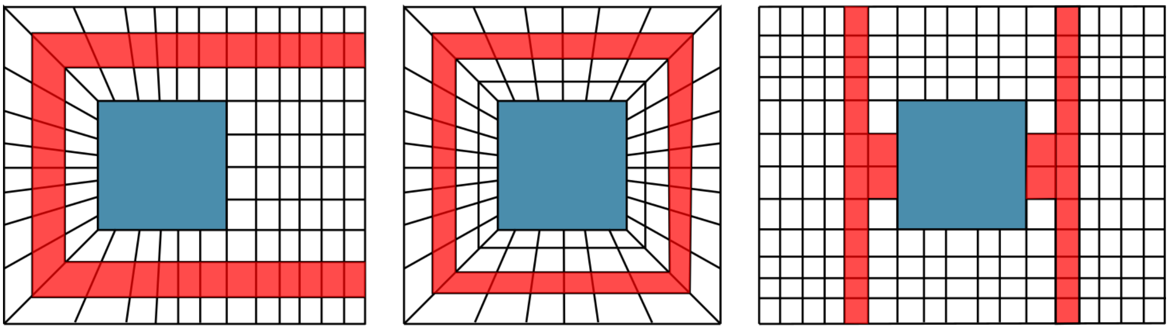

(a) C-Grid (b) O-Grid (c) H-Grid

Fig. 5.6 Example of grid types around a square geometry

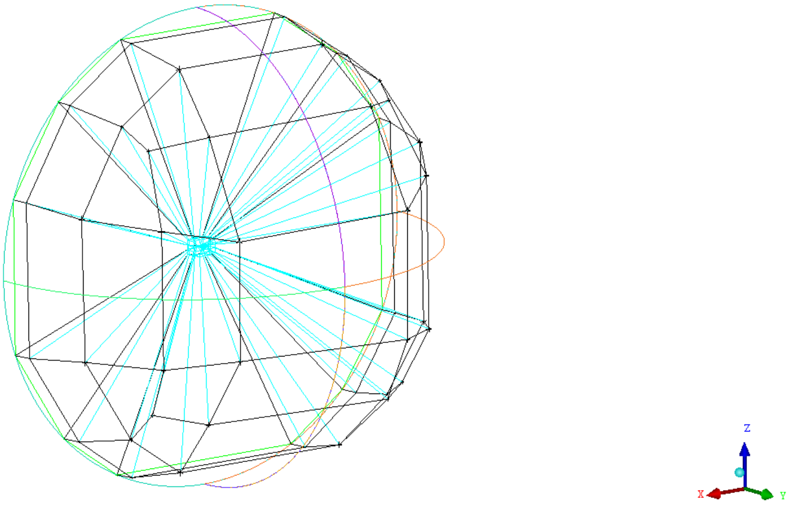

(a) blocking in farfield

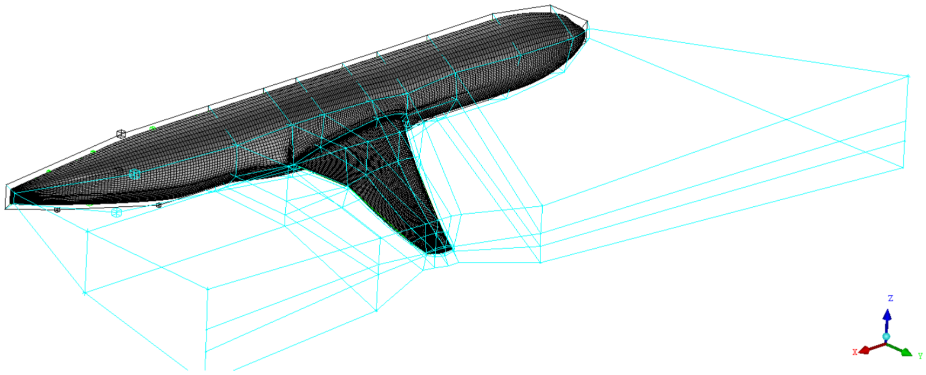

(b) blocking around aircraft

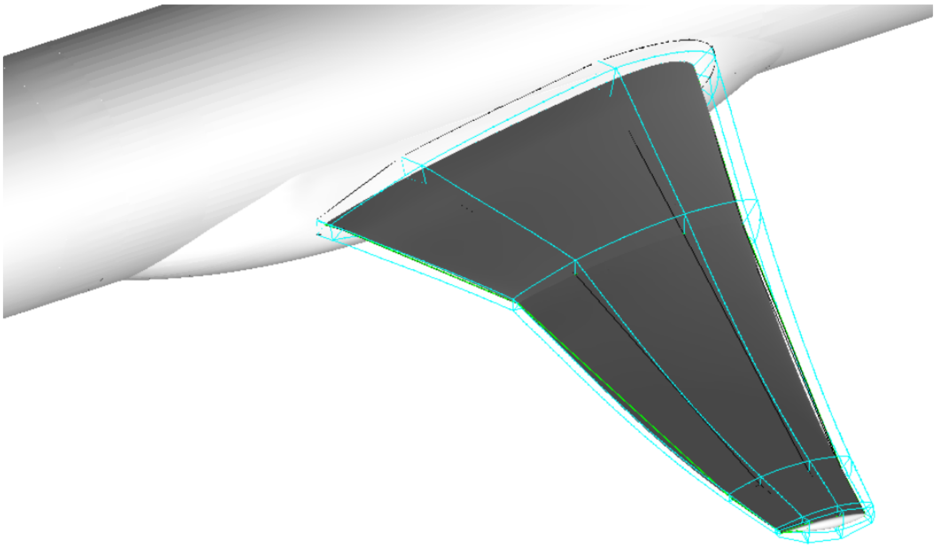

(c) blocking around wing

Fig. 5.7 Blocking structure in ICEM CFD

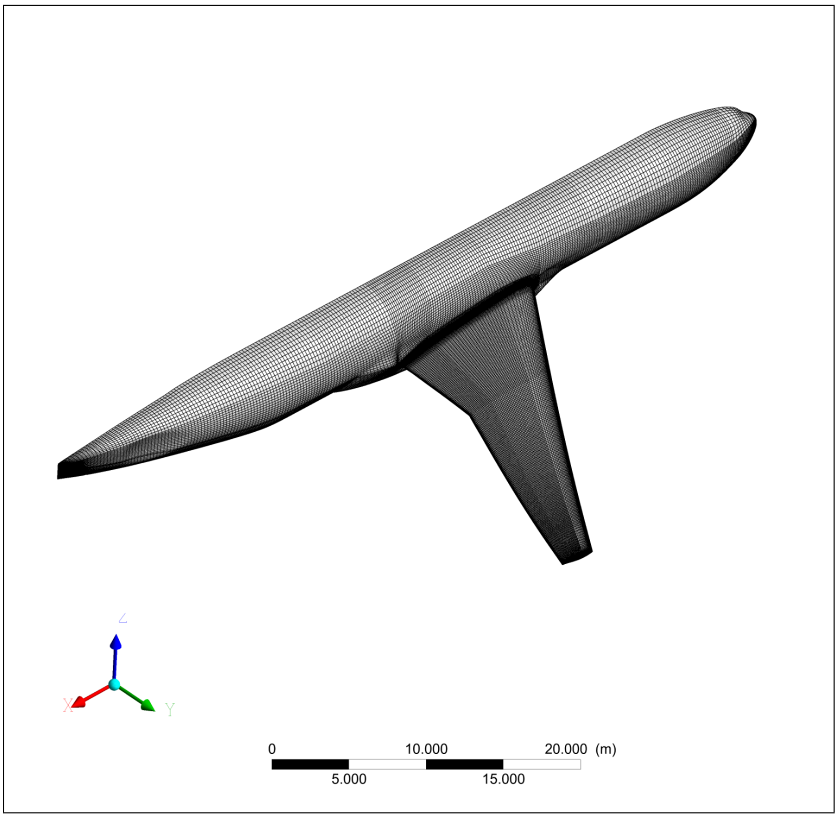

Fig. 5.8 Surface element distribution on the medium grid

generated around the CRM with deformations at 2.5° incidence and later adapted to the other geometries. Adaptation required a translation and rotation of the blocks around the wing whilst maintaining the surface and volume element distribution.

The refinement strategy from coarse to medium and fine grids consists in increasing the number of nodes in each of the x, y and z directions by 15%. This included the decrease in height of the first cell by 15% as well. As a result, the number of nodes increased by 1.45 (1.15^3) with each refinement step. For reference, the characteristics of the three grids that were generated are given in Table 5.3. Figure 5.8 shows the surface mesh for the medium-sized grid.

5.2.2 Solver

The *Finite Volume Method* ANSYS Fluent 16.1 ®is used to solve the discretised RANS equations. Two turbulence models are considered in this study as adequate closures: the

Table 5.3 Characteristics of the three grids generated for this study

Characteristic	Grid		
	Coarse	Medium	Fine
Node count, *million*	11	16.7	25.8
First cell height, *m*	$3.2 * 10^{-5}$	$2.8 * 10^{-5}$	$2.4 * 10^{-5}$
y^+ value	1	0.8	0.67

$k-\omega$ *SST* [43] and *Linear Pressure-Strain RSM* [71]. The *Stress-Omega RSM*, which was proven to be more accurate in Chapter 4 was discarded following multiple attempts during which the simulations could not be converged due to instability of the solver.

Second order upwind schemes were used to discretise the *RANS*, k and ω equations. A first order upwind scheme was used for the *RSM* equations to improve stability of the simulations. Adaptive Courant number was used where possible to speed up the simulation convergence. All runs were performed on the University of Sheffield Iceberg and ShARC HPC facilities. More details about the numerical method can be found in Chapter 3 where the *RANS* approach, the turbulence models and other aspects are described in detail.

All simulations in this chapter are based on a steady-state approach.

Boundary conditions

Freestream boundary conditions at farfield were set for M_∞ = 0.85, P_∞ = 3800 Pa and T_∞ = 310K which resulted in an air density of $\rho = 0.045\ kg/m^3$ and Re_{mac} of 5 million. Viscosity was calculated using the Sutherland law. Incidence was varied by changing the appropriate components of the velocity. The turbulent intensity was set to 0.5%, and the turbulent length scale was set to 0.49 m; based on the chord length and ANSYS guidelines.

At wall, a no-slip condition was selected. All turbulence models used in this study had low-Re settings, meaning that no wall functions were used.

5.2.3 Computational test matrix

A summary of the freestream conditions for this study is given in Table 5.4. Freestream *M*, *Re*, *T* and *P* were maintained constant, incidence α was increased. The appropriate deformed geometries were used at the corresponding incidences. To ensure that the mesh sensitivity study was in line with the other AIAA CFD DPW results, a C_L = 0.5 condition was used.

Table 5.4 Computational run matrix

M	Re	T_∞, K	P_∞, Pa	α, °	Deformations	Grid	Closure
0.85	5 million	310	3800	N/A, $C_L = 0.5$	ae275	C, M, F	RSM
				2.5	ae250	M	RSM, SST
				3.0	ae300	M	RSM, SST
				3.5	ae350	M	RSM, SST
				4.0	ae400	M	RSM, SST
				4.5	ae400	M	RSM
				5.0	ae400	M	RSM
				5.5	ae400	M	RSM
				5.75	ae400	M	RSM
				6.0	ae400	M	RSM

5.3 Results

5.3.1 Verification and Validation

Convergence criteria

The convergence of the simulations is monitored through the *Residuals* and force monitors on the aircraft. Fluent outputs *Residuals*, which are measures of how relative error changes with each iteration, for each equation in the system. A good measure of simulation convergence is for the *Residuals* to decrease with each iteration. Depending on the type and complexity of these simulations, in Fluent, the *Residuals* should decrease by at least three orders of magnitude.

Figure 5.9 gives an example of the evolution of the continuity *Residual* and C_L as output by simulating the flow using RANS closed with *SST* (a) or *RSM* (b). In both cases, the continuity

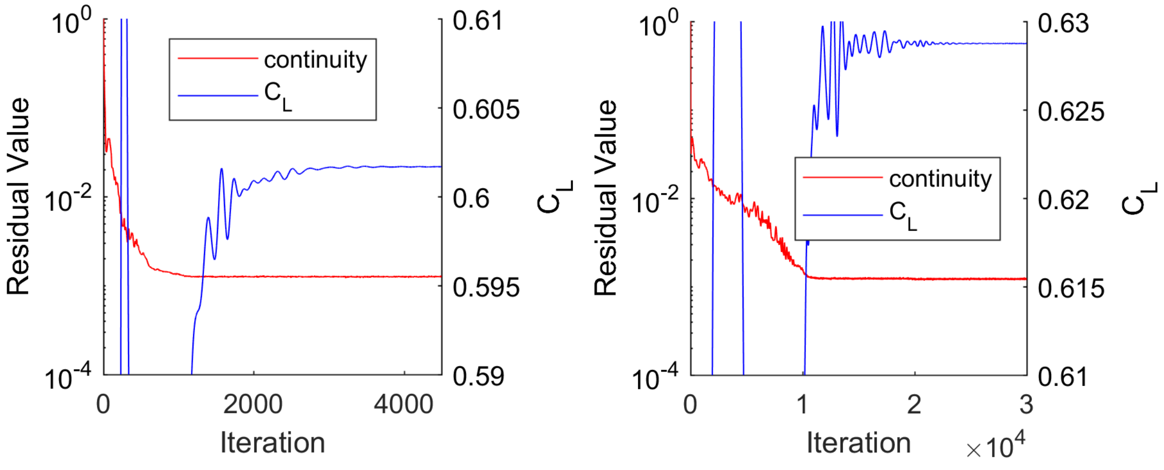

(a) residuals SST **(b)** residuals RSM

Fig. 5.9 Residuals

Residual decreases by at least three orders of magnitude before C_L reaches a converged, steady-state.

Grid sensitivity

The grid sensitivity study was performed in line with with the 6^{th} AIAA CFD DPW requirements. The *ae275* configuration was simulated at design point of $C_L = 0.5$ using the RANS approach closed with the *RSM* turbulence model. The evolutions of total (C_D), pressure (C_{D-PR}), and viscous (C_{D-V}) drag coefficients as well as pitching moment coefficient (C_M) and incidence α with increase in grid size are monitored. The function describing the increase in grid size is $N^{-2/3}$, where N is the number of nodes in the grid.

At the time when these simulations were conducted, Fluent did not include a target C_L boundary condition (i.e. variable α until target C_L is achieved) like other aerospace-focused CFD codes do. As such, three simulations were performed on each grid. The first two simulations, at α = 2.2 and 2.75° respectively, as it is known that the polar is linear in this range of incidences.The $\delta C_L/\delta\alpha$ can then be found. A third simulation was run at an incidence that was interpolated based on the $\delta C_L/\delta\alpha$ so that $C_L = 0.5$. This process can be visualised in Fig. 5.10. There is a small variation in the incidence at which $C_L = 0.5$ is reached with the three grids which is in the order of $10^{-2\circ}$.

The evolution of drag over the three grids is visualised in Fig. 5.11. Wind tunnel and 6^{th} AIAA CFD DPW results are superimposed for reference. It is defined that *1 drag count* (1

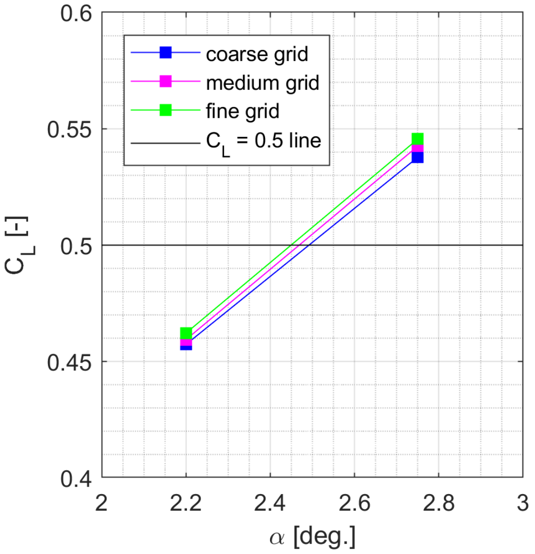

Fig. 5.10 Process of determining the α at which $C_L = 0.5$ in the grid sensitivity study

dc) as being 10^{-4}. The total drag decreases by less than 10 dc with the increase in node count. It is overpredicted when compared to the 6^{th} AIAA CFD DPW numerical results and experimental data. From Fig. 5.11 b and c, it is visible that this overprediction is due to the viscous drag which is overpredicted. At the time of writing there was no opportunity to further break down the C_{D-V} into the various typical components to analyse whether this overprediction is due to wing or fuselage drag. In either case, a possible overprediction in viscous drag can be associated with either poor prediction of the boundary layer or poor prediction of shockwave strength.

The changes of C_M and α with the increase in grid size are given in Fig. 5.12. Both quantities are within the range that were predicted in the 6^{th} AIAA CFD DPW and change very little. The discrepancies in C_M and α at C_L = 0.5 with respect to experiments have been previously attributed to sting support systems [87].

Of equal importance is to analyse the change in wing aerodynamics with grid size. The pressure coefficient, C_P, distributions at six spanwise locations are given in comparison with experimental data from NASA Ames from [88] in Figs. 5.13 and 5.14. Figure 5.14 is just a zoomed in view of Fig.5.13 with focus at the shock location. There are insignificant differences between the three simulations. When compared to experimental data, the simulations accurately capture the suction peak, supersonic plateau and the strong adverse

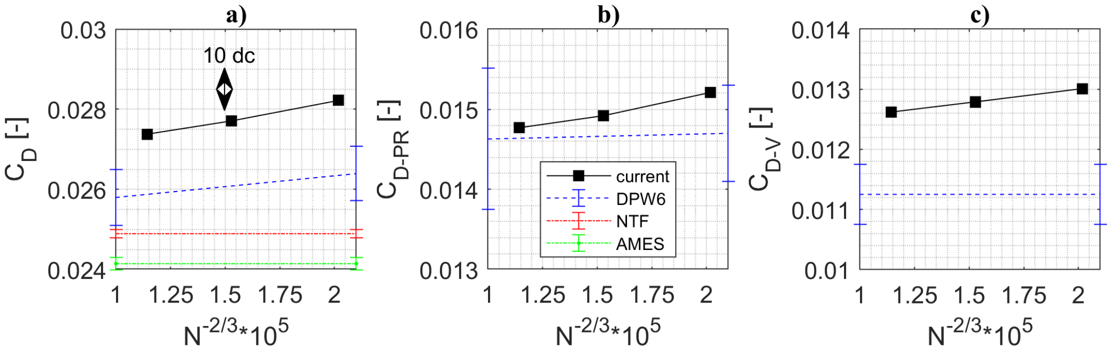

Fig. 5.11 Grid sensitivity evaluated through: a) C_D, b) C_{D-PR}, and c) C_{D-V} at $C_L = 0.5$

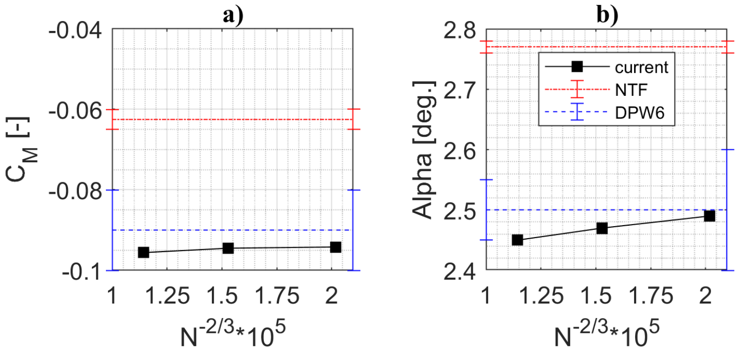

Fig. 5.12 Grid sensitivity evaluated through C_M, and α at $C_L = 0.5$

pressure gradients at and downstream of the shock front. Shock location is predicted further downstream than observed in the experiments at the η = 0.727 and 0.846 spanwise locations.

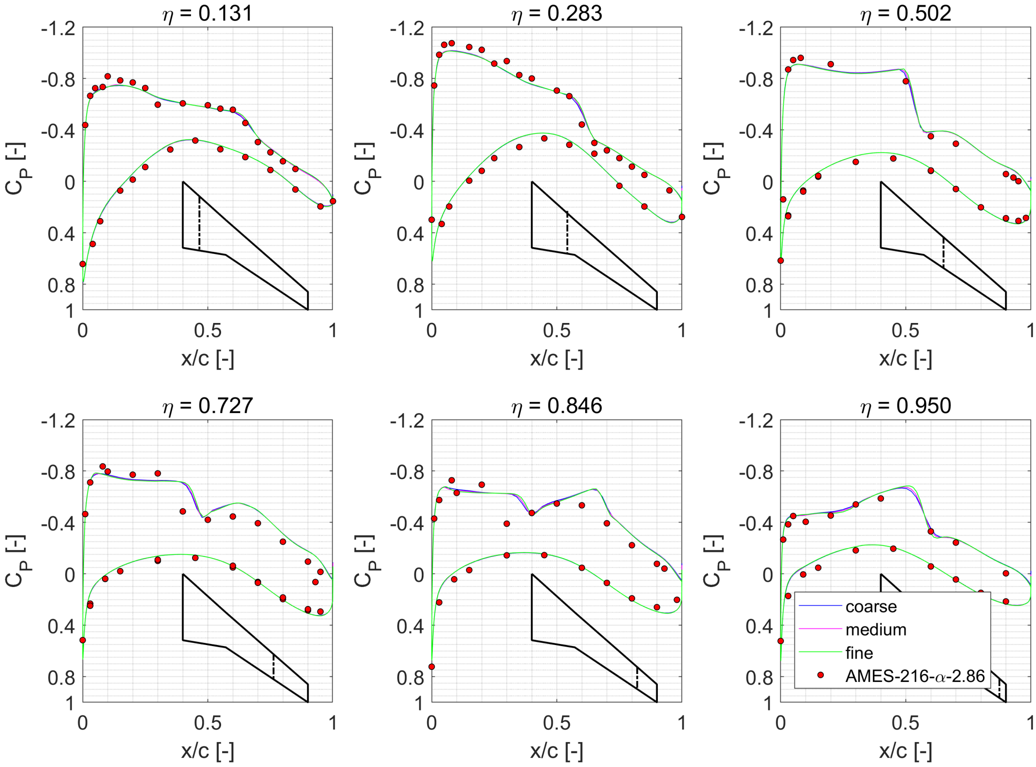

Fig. 5.13 Pressure coefficient slices at $C_L = 0.5$

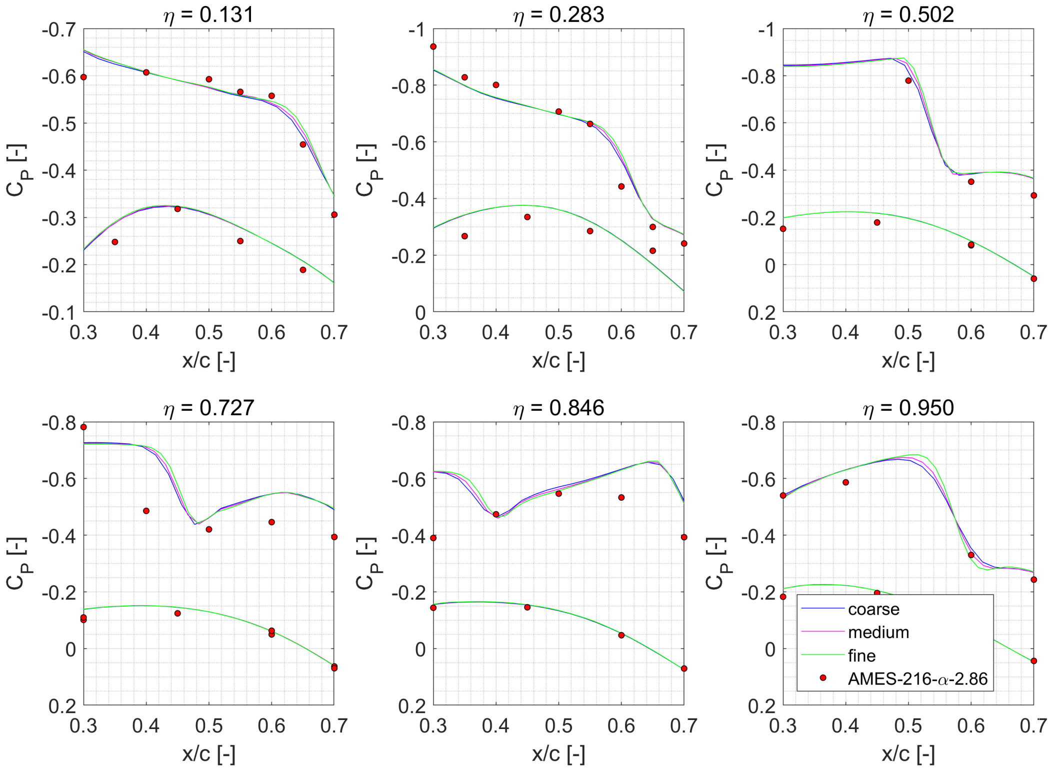

Fig. 5.14 Pressure coefficient slices at $C_L = 0.5$

Following the observations made durin this grid-sensitivity study, it is considered that the grids are sufficiently fine to produce a grid-independent solution. For the remainder of the study, unless otherwise stated, the medium-sized grid has been used.

5.3.2 Turbulence model study

The next step following the grid-sensitivity study is to asses which of the two chosen turbulence closures are more appropriate for simulating this aircraft configuration in off-design, high incidence, transonic flight. As such, a comparison between the results obtained using the *SST* and *RSM* is given in a manner resembling the analyses in the AIAA CFD DPWs.

The aerodynamic coefficients, C_L, C_D, and C_M computed using the two different turbulence models are given in comparison with exp. data from NASA in Fig. 5.15. It is a first good way to compare the results and observe the ability to produce accurate overall aerodynamics predictions using CFD. In terms of absolute accuracy of C_L (Fig. 5.15a), both sets of results predicted higher lift than the experiments. The absolute values obtained using the *SST* model are in better agreement with experiment at incidences α=2.5 to 3.5°. At α=4.0°, a sudden decrease in lift (also known as a *lift break*) is predicted by the *SST* model. This was also observed in previous results obtained with the *SST* turbulence model in Refs. [89] and [90]. It is attributed to a non-physical increase in the side-of-body (SOB) separation as shown in Fig. 5.16. Some CFD codes, but not Fluent, have in their implementation a *Quadratic Constitutive Relationship* to improve the prediction of such non-linear flows [91].

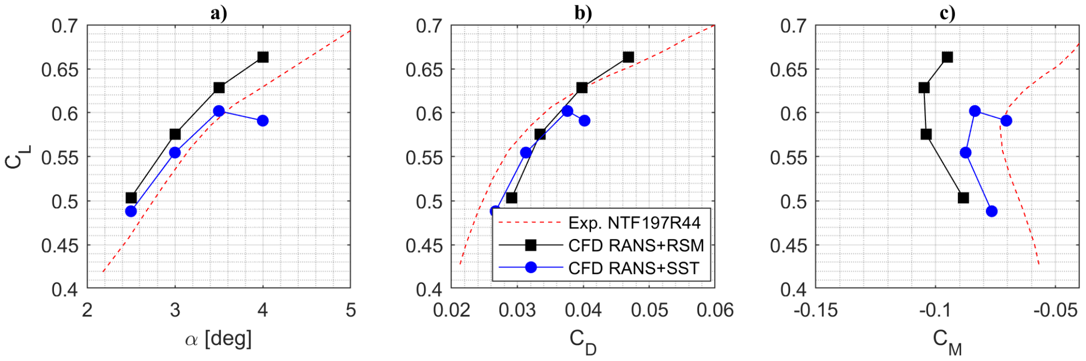

Fig. 5.15 Aerodynamic coefficients obtained with the two turbulence models

The C_L vs α curve can also give an indication of the evolution of aerodynamics as the incidence is increased. It is visible in Fig. 5.15 that the set of results computed using the *RSM* turbulence model is in much better agreement than that obtained with the *SST* model. The *SST* model gives a continuous decrease in $\delta C_L/\delta\alpha$ value, whereas the *RSM* model follows the experiment trends.

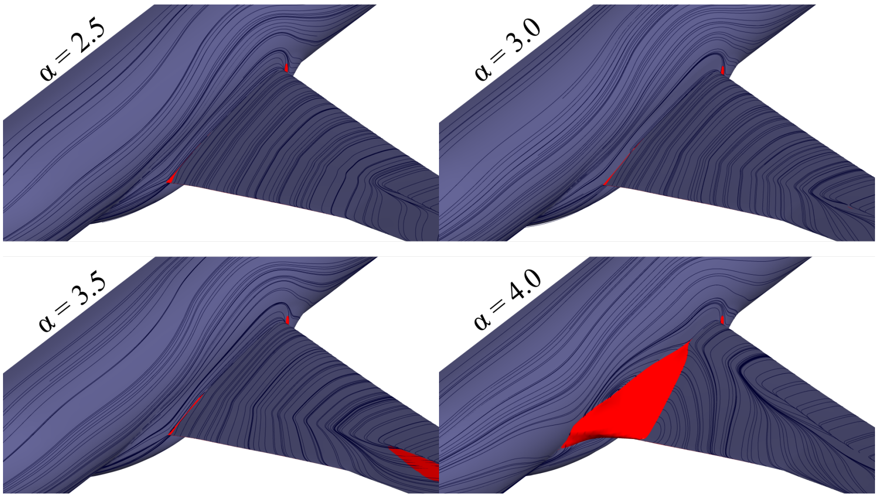

Fig. 5.16 Increase in the SOB as computed using the SST turbulence model. Isosurfaces of negative *u* shown in red.

Figure 5.17 gives the computed C_P contours on the suction side of the wing at α=2.5-4.0° The difference between the two sets of results is evident. In the *SST* results, a boundary layer separation bubble is present mid-wing at the shock-foot even from low incidence of 2.5° (see Fig. 5.18 for zoom in at $\alpha = 2.5 - 3.5°$). As the incidence is increased, this also increases but at α=4.0°, the SOB separation dominates the whole field. By comparison, in the set of data obtained with *RSM*, although some crossflow is present at α=2.5 and 3.0°, the separation bubble is not observed to appear until α=3.5°. Thus, both sets of results reveal different aerodynamics about this aircraft configuration.

To improve our understanding of how these predictions compare with the experiments, the computed C_P distributions at six η positions and α=3.5-4.0° are given in Fig. 5.19 and 5.20 along with experimental data. Surprisingly, from Fig. 5.19, the C_P computed with *SST* is still in much better agreement than that computed with *RSM*. This is mainly due to a better prediction of the shock-location which is poorly predicted by the *RSM* turbulence model. At α=4.0° though, as seen in Fig. 5.20, the effect of the large SOB has an impact on the pressure at the η locations inboard of the wing-kink. Thus, it is not advisable to believe that the modelling on the outboard of the wing is physical. The *RSM* results still show a further downstream location of the shockwave.

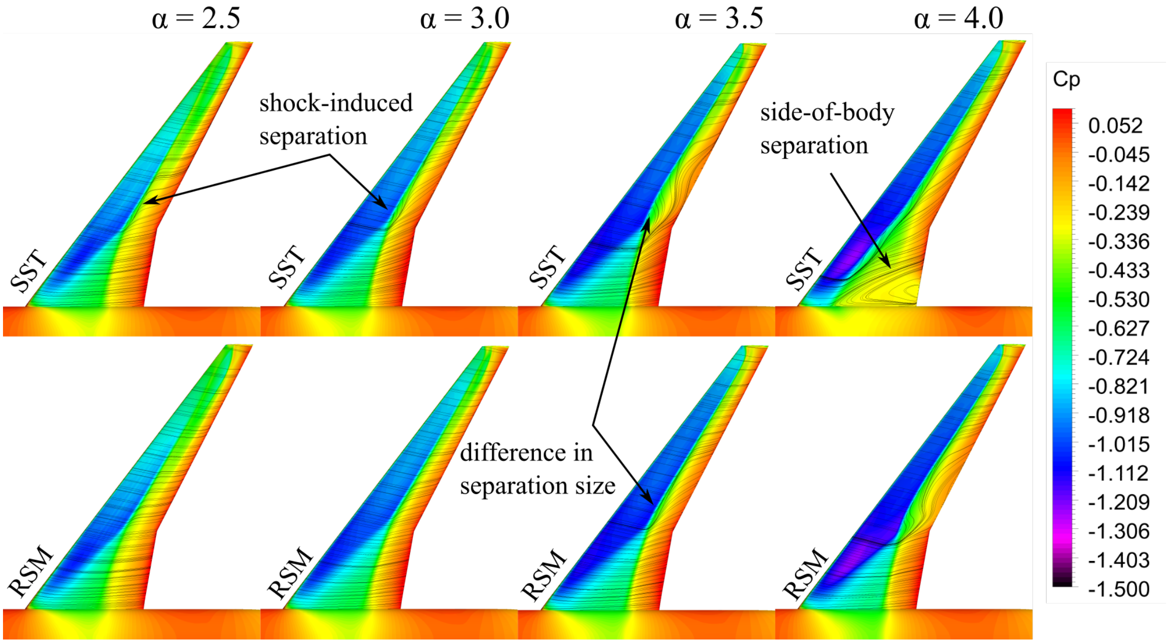

Fig. 5.17 C_P contours at different incidences

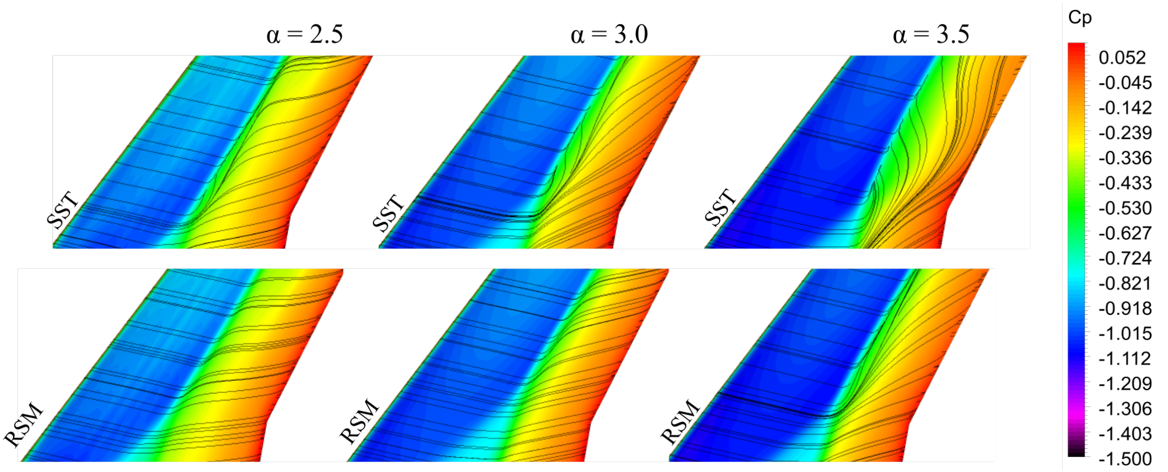

Fig. 5.18 Zoom in view of C_P contours at $\alpha = 2.5 - 3.5°$, to highlight the shock-induced separation present in the SST results

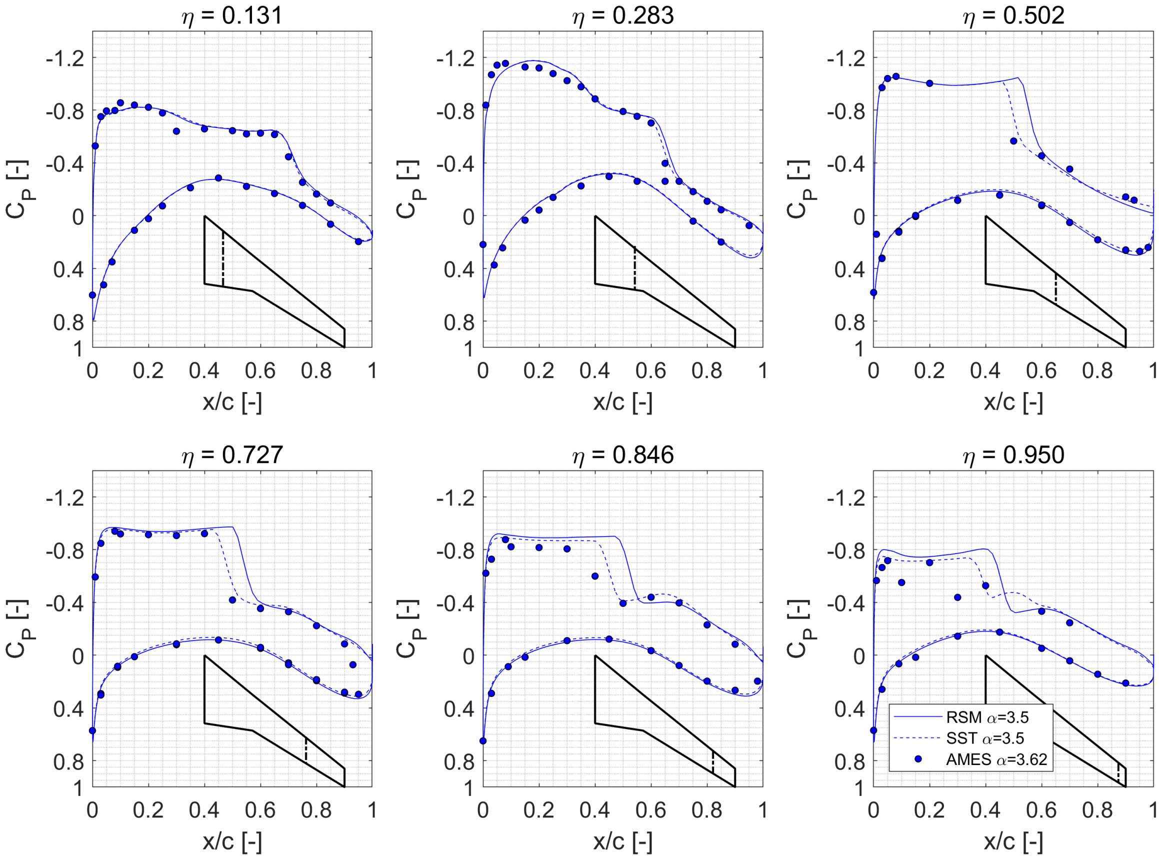

Fig. 5.19 C_P distributions as computed by *SST* and *RSM* at α=3.5°

This study is conclusive at this point. Although the *SST* results are in much better agreement with experimental data at small incidences, due to the limitations of the linear Boussinesq approximation, it is unable to predict the high incidence aerodynamics as a large *SOB* is predicted. On the other hand, the full *RSM* model does not suffer from this drawback. But unfortunatelly, the results are overpredicted and a good indication of this overprediction is the more forward downstream position of the shock-wave than that in the experiments.

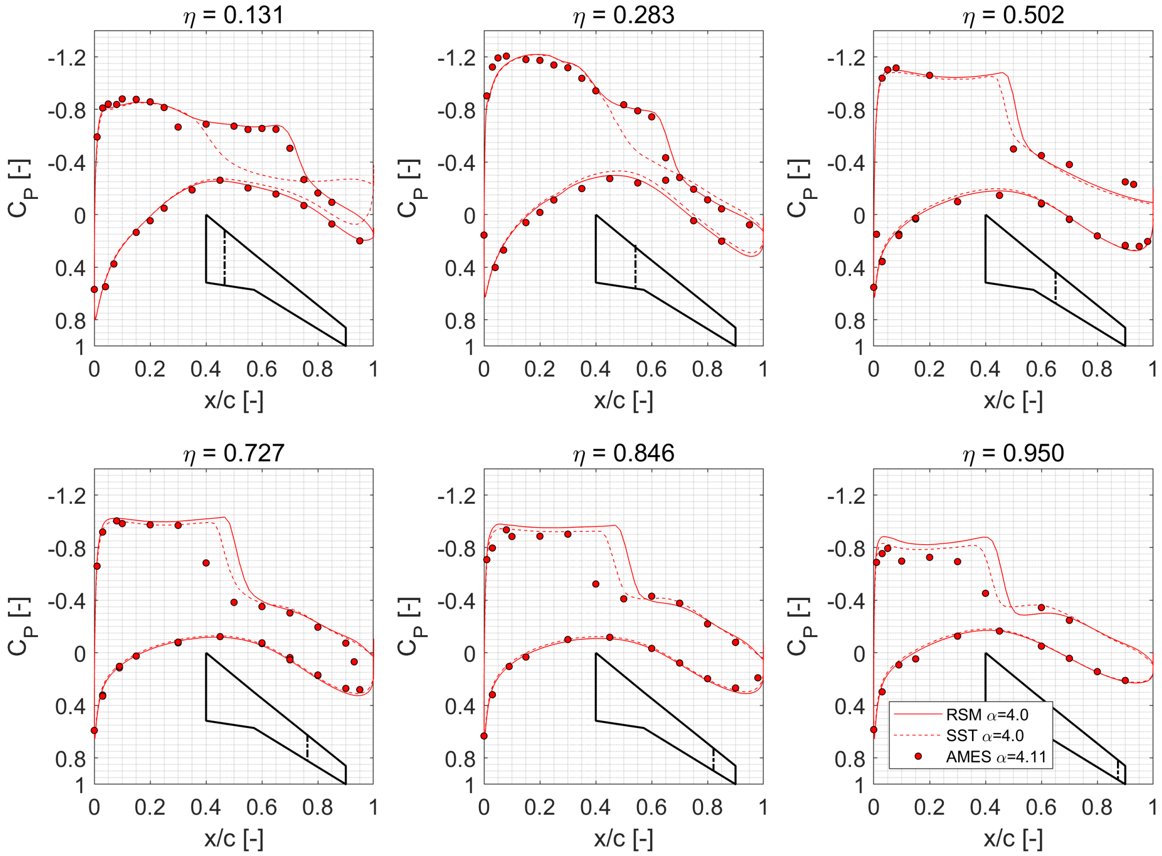

Fig. 5.20 C_P distributions as computed by *SST* and *RSM* at α=4.0°

5.3.3 Development of shock-induced boundary-layer separation

The *ae400* CRM is further simulated at incidences above 4.0° using the RANS approach closed with the *RSM*. Ideally, to accurately compare with the experiments, the CRM would be further deformed using the deformations measured in the wind tunnel. But, from Fig. 5.3 it is visible that as incidence increases, the wingtip deflection and twist (ω_{tip}, and ε_{tip} respectively) change less and less. After $\alpha = 4.0°$ they become negligible compared with those at lower incidence. Thus, the *ae400* geometry can be considered as a good approximation.

The additional simulated points have been added to the aerodynamic polars and are given in Fig. 5.21. As the incidence is increased, the slope of the C_L vs α curve computed with the *RSM* decreases with a $C_{Lmax} = 0.71$ at an incidence $\alpha_{stall} = 5.75°$. The computed stall angle is much lower than that observed in the experiments. In fact, it is visible that the value of $\delta C_L/\delta\alpha$ decreases too quickly. In [28], the authors suggest that this is an effect of shock-buffet or shock-induced boundary layer separation. To understand why, we need to inspect the evolution of C_P over the wing and that of the C_{Fx} and shear lines.

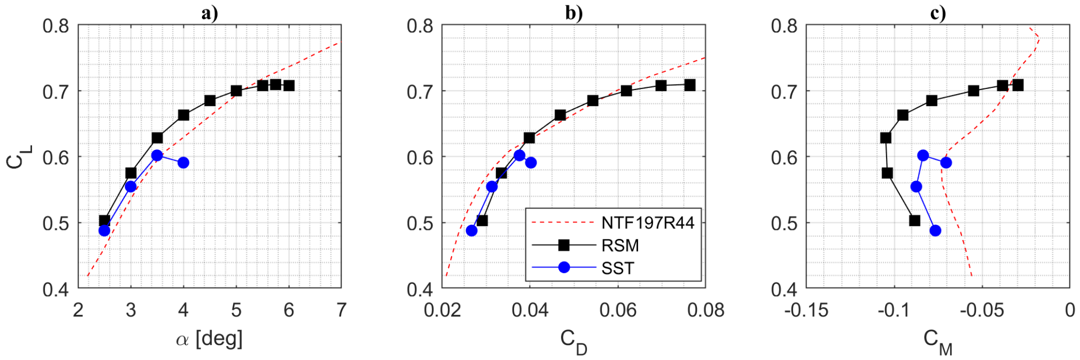

Fig. 5.21 Aerodynamic coefficients obtained with the two turbulence models

The C_P distributions at inboard (η = 0.131 & 0.283), mid (η = 0.502 & 0.727) and outboard (η = 0.846 & 0.95) spanwise locations are given in Fig. 5.22 for incidences α = 4.5, 5.0, 5.5, and 6.0°. The two inboard sections show little change in wing loading with increase in incidence. Only at α = 6.0°, at η = 0.283 the overall loading changes, possibly due to shock-induced separation reaching the inboard side of the wing.

In the two mid-wing sections shown in Fig. 5.22, the incidence is seen to have a significant impact on the C_P distributions.The shock location advances upstream with increase in incidence by up to 0.2 of local x/c. A flattening of the pressure recovery downstream of the shock is also visible. This can be linked with the presence of shock-induced separation. By comparison, the data from the experiments are in good agreement at η = 0.502 but discrepancies are observed at η = 0.727. The experiments did show any movement in the shock. Thus, in this particular region, the CFD results show a decrease in wing loading whereas the experiments do not. This is a potential reason for the more aggressive decrease in $\delta C_L/\delta\alpha$ in the CFD results.

Overall, the outboard wing sections are in good agreement with experiments.

It is now interesting to analyse how these changes in pressure loading are related to the global aerodynamics over the wing and how the shock-induced separation evolves on the suction side. From the C_P distributions, the area of interest where changes occur with increase in incidence is between η = 0.283 and 0.727.

Figure 5.23 gives evolution of C_{Fx} contours and wall shear lines with the increase in incidence. This visualisation provides with two important aspects of the development of shock-induced separation. Firstly, C_{Fx} contours provide an assessment of the overall health of the boundary layer and areas where it is more susceptible to separate. The closer to 0 C_{Fx} is, the more likely for the flow to separate or for local areas of recirculation to appear. Negative values of C_{Fx} indicate reversed flow with respect to the streamwise direction. Secondly, the shear lines are a more intuitive way of visualising the general flow pattern over the wing.

At C_L = 0.5, the design point, the majority of the flow over the wing is in the streamwise direction with the exception of a insignificant amount of cross flow just outboard of the wing kink (η = 0.397). The C_{Fx} contour reveals that the boundary layer health is good. As the incidence is increased to 3.0 and later to 3.5° the amount of crossflow becomes more significant and a separation line develops at the shock-foot. This is due to strong adverse pressure gradients that the air encounters across the shock. At 3.5° incidences, a small separation bubble is observed. No negative C_{Fx} is present yet but the low values indicate a *stressed* boundary layer more susceptible to separation.

The separation bubble expands in the chordwise and spanwise directions until it bursts when it reaches the trailing edge of the wing at α = 4.5°. The growth of the separation bubble is directly related to an increase in adverse pressure gradients attributed to the increase in incidence, easily visualised by the magnitude of C_P increase across the shock in Fig. 5.22, particularly at $\eta = 0.502$ and 0.603. Significant amount of negative and very low positive C_{Fx} is presente on the outboard side of the wing kink. The crossflow now extends over a long portion of the wing before redressing to streamwise direction at about η = 0.727. The trends continue with further increase in incidence, close to α_{stall}, the shock-induced separation is seen to travel inboard of the wing kink too. It is understandable why this amount of flow separation resulted in the stall of the aircraft.

We know from the comparison with the experiment in Fig. 5.22 that this separation zone is larger than in reality. It shows a possible limitation of this approach but also it is worth considering that by this point, experiments revealed a significant amount of shock-buffet to be occurring on the CRM. Thus, an unsteady RANS approach would be more suitable at predicting this flight scenarios.

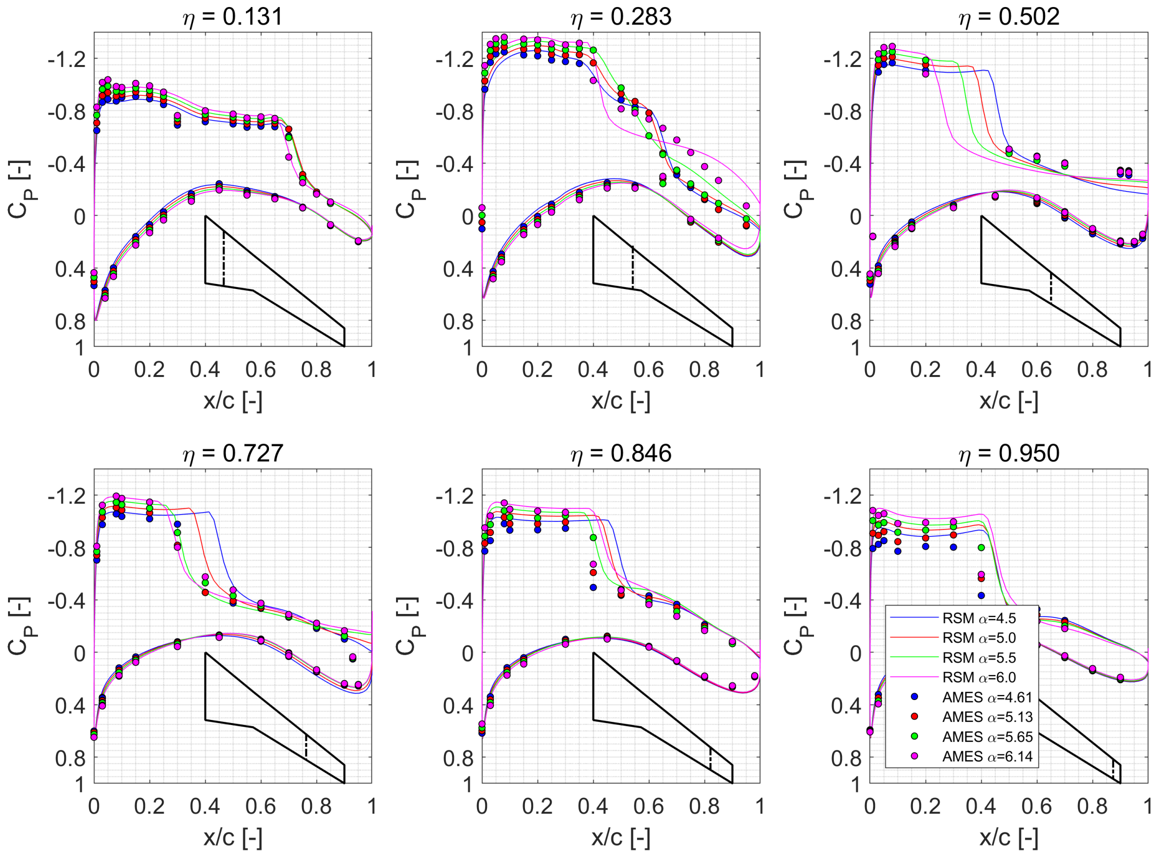

Fig. 5.22 Computed C_P distributions at α = 4.5 - 6.0° and comparison with experimental data

5.4 Lessons learnt and conclusions

In this chapter, an effort to predict off-design transonic aerodynamics of transport aircraft was presented. The *NASA Common Research Model* aircraft was chosen as a test-bed representative of modern wide-body transport aircraft. The steady RANS approach, commonly used in the industry, was closed with two different turbulence closures: the eddy-viscosity *Menter SST*, and the full, second-order *RSM* turbulence models.

A new family of grids was developed and presented in Section 5.2 based on the guidelines of the *AIAA CFD Drag Prediction Workshop* organising committee. The grid-sensitivity study that followed revealed that the selected approach predicted good accuracy pressure loading on the wing surface but lacked accuracy in the absolute value of the viscous drag coefficient.

The turbulence model study that followed the guidelines of the 6^{th} *AIAA CFD DPW* was performed to assess the ability to produce good accuracy development of the transonic

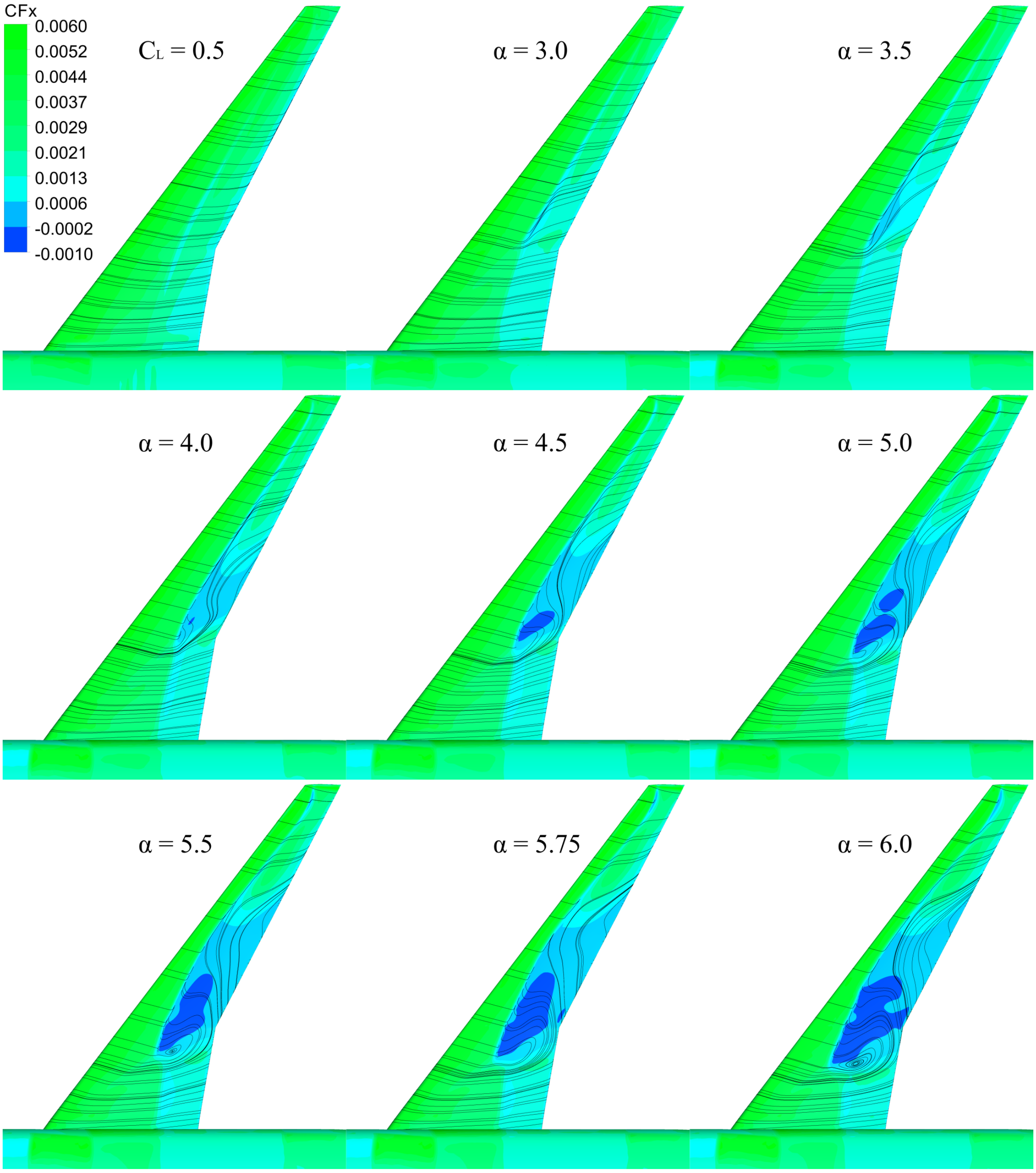

Fig. 5.23 Development of shock-induced separation visualised through shearlines and isosurfaces of negative streamwise velocity, u

aerodynamics as the aircraft is simulated at higher and higher incidence into the off-design flight regimes. The study showed that, similar to previous observations from others, the *SST* model overpredicted the side-of-body separation, inducing an early, non-physical stall of the aircraft.

With regards to the simulations performed at incidences higher than 4°, this chapter revealed that a steady RANS approach will not predict accurately the development of shock-induced separation.

Chapter 6

Characterisation of shock-buffet on NASA CRM

This chapter can be seen as a continuation of the previous one. It was just concluded that *steady-state* RANS simulations are not appropriate for off-design transonic flight as the shock-induced separation, which can be inherently unsteady, is overpredicted. This resulted in an early stall of the aircraft when compared with experimental observation.

Thus, in this chapter, *time-marching*, unsteady RANS (URANS) simulations are presented. The same *NASA CRM* aircraft introduced in Chapter 5 is simulated using a similar numerical approach. The aim is to assess the ability to predict the shock-buffet phenomenon in modern aircraft. The characteristics of the predicted phenomenon will be compared with experimental observations that have been already published by other research institutions.

A parametric study will follow to determine the impact of freestream, geometrical and numerical parameters on the prediction of this phenomenon.

The work conducted in this chapter is the result of an international collaboration and research exchange program between *The University of Sheffield* and the *German Aerospace Centre* (DLR - Deutschez Zentrum fur Luft- und Raumfahrt). The author is grateful for the support of both institutions which was essential to completing this work. The co-author of this work, Dr. Ing. Vlad Ciobaca, and the support of his colleagues at DLR is kindly acknowledged.

6.1 Numerical Approach

6.1.1 Geometry

The aeroelastically deformed wing-body *NASA CRM* from the 6^{th} *AIAA CFD DPW* introduced in Section 5.1 is used in this study. Only the *ae400* configuration which is deformed based on the wind tunnel model deformation when tested at an incidence $\alpha = 4.0\ ^\circ$ is considered.

6.1.2 Numerical grids

The medium grid from Section 5.2 is adapted and used in this study. The adaptation consists in an increase in nodes to 17.5 million and redistribution of surface grids to eliminate any areas where sudden jumps in element sizes were identified.

No other significant changes have been performed, the blocking structure remained the same, the volume grid was minimally changed.

6.1.3 Solver

The finite volume method and unstructured CFD code DLR-Tau [77] is used in conjunction with the DLR-FlowSimulator [92] python interface.

The RANS equations are closed with the *SSG/LRR-g* variation of the full *RSM* [70] (see Section 3.3.4 for details). Convective fluxes are discretized using a central scheme with matrix dissipation and added artificial viscosity. Turbulent fluxes are discretized using a second order upwind Roe scheme. A semi-implicit LU-SGS time-stepping scheme is used. The time-marching simulations are run with a dual time-stepping method with a maximum of 100 inner-iterations per physical timestep. C_L residual was monitored, and ensured that it decreased by at least 6 orders of magnitude before the end of the 100 inner-iterations.TAU provides C_L convergence criteria which, in hindsight, is a much better option to ensure that there is a consistency in the convergence of each timestep.

For time-marching simulations, a physical timestep $\Delta t = 0.5$ ms was chosen according to the convective time over the mean aerodynamic chord, and based on the experimental observations of the shock-buffet highest frequencies. A total physical time of at least 1 second is simulated for each data point. No simulation is started from scratch. Each time-marching simulation uses a partly-converged steady-state simulation as initialization.

The effect of Δt is investigated too. A total of 0.2 seconds of real time is simulated at $M_\infty = 0.85$, $Re_{mac} = 5$ million, and $\alpha = 6°$ is run with a $\Delta t = 0.1$ ms.

The DLR-FlowSimulator interface was used to prepare and run the paralelized jobs on the $C^2A^2S^2E^2$ HPC facilities.

Boundary conditions

Freestream boundary conditions at farfield were set for M_∞ = 0.85, T_∞ = 310K, reference Sutherland air viscosity and temperature $\mu = 1.7874 * 10^{-5}$ kg/ms and $T_{ref} = 273$K; and the appropriate value for Re_{mac} which for this study was varied among: 0.9, 1.5, and 5 million. DLR-Tau uses these three references values alongside with the reference viscosity and Sutherland law to compute the remaining flowfield variables (e.g. Pressure).

At wall, a no-slip condition was selected. All turbulence models used in this study had low-Re settings, meaning that no wall functions were used.

6.1.4 Computational test matrix

A continuation from Chapter 5 is ensured by maintaining the values for $M_\infty = 0.85$ and Re_{mac} = 5 million. A comparison with steady and unsteady experimental data obtained at these freestream conditions by Balakrishna *et. al.* [30] is possible. Incidence α is varied between 4 and 6.5°. These results provide an opportunity to analyse shock-buffet dynamics.

The value of Re_{mac} is then decreased to 1.5 and 0.95 million to investigate the Re effects on shock-buffet. The DLR-Tau solver takes Re_{mac} as an input which is achieved by changing reference ρ of the freestream air. Furthermore, a more in-depth, qualitative comparison with the recent experiments of Koike *et. al.* [33] and Sugioka *et. al.* [34] would be possible. For these two values of Re_{mac}, time-accurate results are produced at only one incidence α of 6°.

A summary of the computational test matrix is given in Table 6.1.

Table 6.1 Computational run matrix shock-buffet

Run	M_∞	Re_{mac}	α (°)	Geometry	Simulation Type	Remarks
			Verification and Validation			
1	0.85	5 million	4	ae400	steady-state	N/A
2	0.85	5 million	6	ae400	$\Delta t = 0.1$ ms	comp. with Run 5
			Buffet characterisation			
3	0.85	5 million	4	ae400	$\Delta t = 0.5$ ms	comp. with [30]
4			5			
5			6			
6			6.5			
			Effect of aeroelastic deformations			
7	0.85	5 million	5	ae500	$\Delta t = 0.5$ ms	N/A
8			6	ae550		N/A
			Effect of Reynolds Number			
9	0.85	1.5 million	6	ae400	$\Delta t = 0.5$ ms	comp. with [33] [34]
10	0.85	0.95 million	6	ae400	$\Delta t = 0.5$ ms	comp. with [33] [34]
			Effect of numerical parameters			
11-13	0.85	1.5 million	6	ae400	$\Delta t = 0.5$ ms	discret. schemes

6.1.5 Numerical probing of unsteady pressure data

In addition to typical output of surface and field data, a numerical probing of unsteady surface pressure data is being performed to assess, on-the-fly, the evolution of the time-marching simulations. This strategy mimics the way some wind tunnel data is being sampled and it offers the ability to perform a better assessment whether shock-buffet is present in the time-marching simulations or not.

For this purpose, 64 surface probes are defined on the suction side of the wing. Their locations was chosen to match those of the unsteady pressure transducers in the experiments from [30], [33], and [34]. The area between $\eta = 0.5 - 0.73$ and local $x/c = 0.15 - 0.8$ is covered; where the unsteady SWBLI is expected to occur. Figure 6.1 helps visualise this. The probes are virtual and no modifications were made to the actual CFD model/mesh, although it would be interesting to investigate if such modifications can change the results significantly.

The C_P is sampled at these locations once every 5 timesteps, giving a sampling frequency $f_{sampling}$ of 400 Hz ($St = 9.5$). As a result, based on highest expected frequency of shock-buffet, at least 20 samples will be recorded every period. For every simulation, each probe generates a signal. The signal is automatically recorded in a separate text file which can be used to plot the signal as the simulation progresses.

At each η location, the signals can be plotted together such as in Fig. 6.2 alongside a quick analysis of those signals. The left hand side of Fig. 6.2 gives the time histories of C_P at each chordwise location of that spanwise cut. In the middle, the amplitude of fluctuation is calculated using the root mean square values $C'_{P_{rms}} = rms(C_P - C_{Pmean})$. Plotting $C'_{P_{rms}}$ with regards to x/c helps determine the location of unsteadiness in the flow. Higher $C'_{P_{rms}}$ indicate that there is a larger deviation from the mean, thus higher oscillation amplitudes. Finally, on the right hand side, the Power Spectral Distribution (PSD) of the C_P signals is given against x/c and St. In this case, St (Strouhal number) is defined as $St = fc_{mac}/U_\infty$. The map shows which frequencies are dominant in the signals at different x/c location.

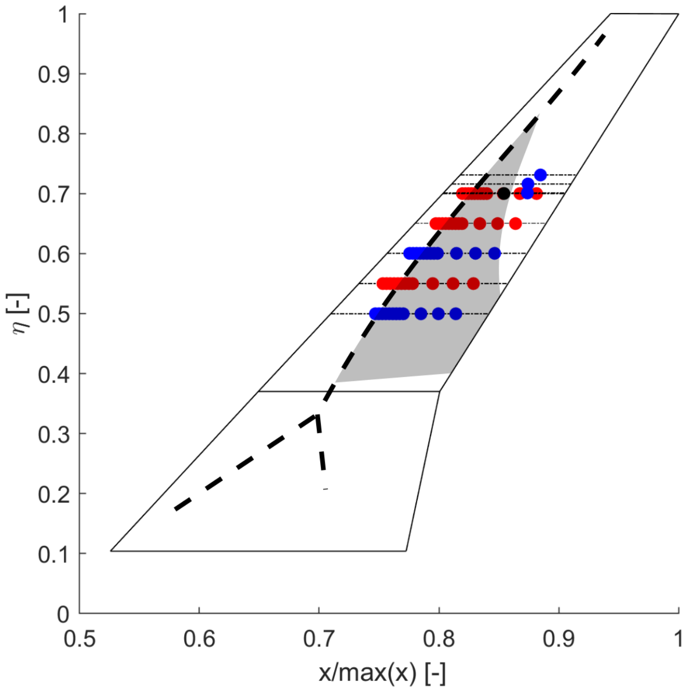

Fig. 6.1 Location of numerical surface probes where unsteady pressures are sampled based on location of unsteady pressure transducers in the experiments of: NASA (●); JAXA (●); and additional ones (●). The shaded gray area shows the location where shock-induced separation occurred in experiments

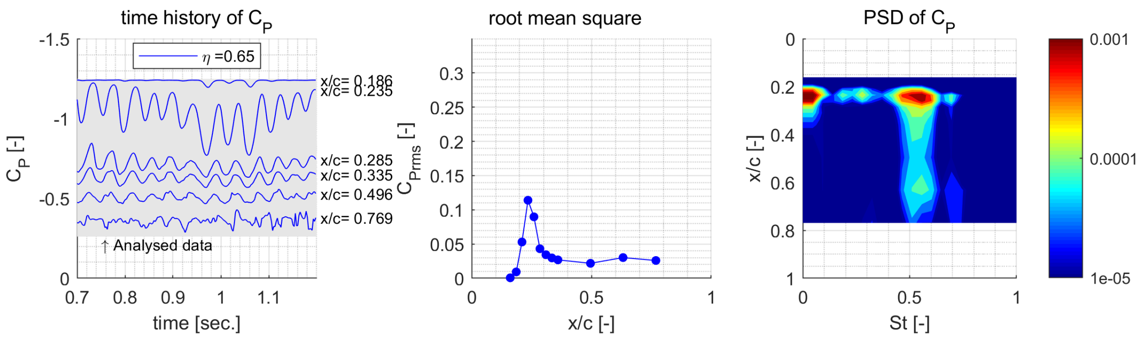

Fig. 6.2 Example analysis of unsteady C_P signals, data recorded for $M_\infty = 0.85$, $Re_{mac} = 5$ million, and $\alpha = 6.5°$

6.2 Results

6.2.1 Verification and validation

An important stage in producing any numerical results is ensuring that the model is appropriately validated and that numerical verification is performed. This section addresses this topic.

Numerical verification

As any other CFD code, the DLR-Tau code outputs residual values that can be monitored to assess the numerical evolution and convergence of simulations. In this study, two such residuals were monitored besides other physical quantities of interest.

For steady-state computations, the evolution of the *Density residual* and the value of the C_L were monitored to assess the convergence of the simulation. Fig. 6.3a shows that the *Density residual* decreases by up to 4 orders of magnitude before it plateaus. Sartor and Timme's [55] computations had a similar value in density residual. They suggested that, should it not be for the shock-induced separation, a further decrease to lower values would be present.

Time-marching simulations were ran with a maximum of 100 inner iterations which were sufficient for the C_L residual to decrease by 6-8 orders of magnitude, as shown by Fig. 6.3b. This means that the value of C_L changes by less than 10^{-6} between the penultimate and final inner iteration of the timestep. Considering that the value of C_L is in the order of 10^{-1}, this is an acceptable convergence criteria, also similar with what others who study similar phenomena have chosen [56].

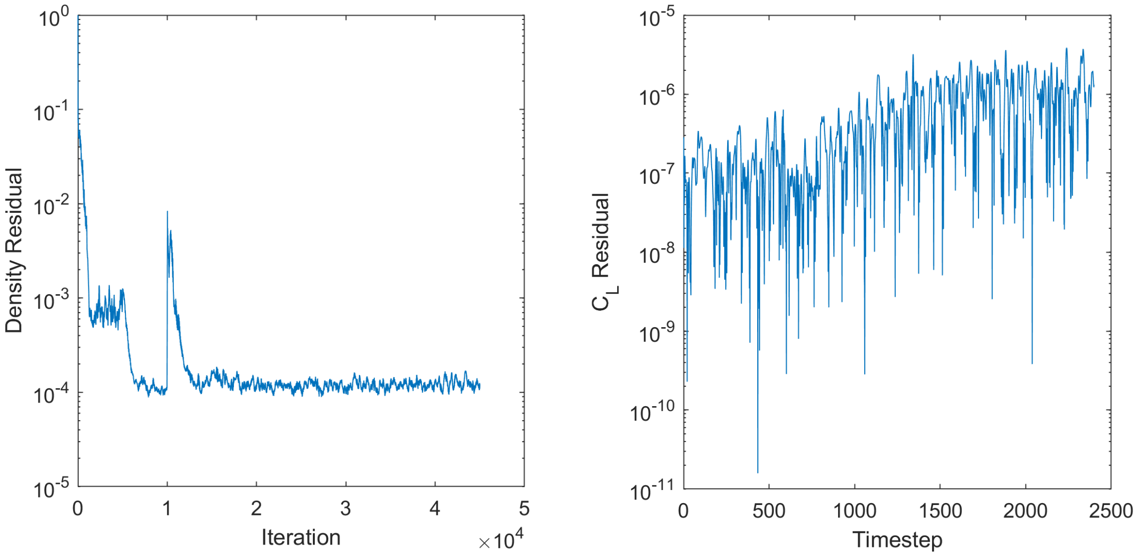

(a) Density Residual in steady-state simulations **(b)** Value of C_L Residual at the end of each timestep

Fig. 6.3 Monitoring the residuals to determine the numerical accuracy of the simulations

Steady-state validation

To validate the mathematical and numerical models, the steady-state results obtained at $M = 0.85$, $Re_{mac} = 5.0$ million, and $\alpha = 4.0°$ are compared with experimental data from NASA AMES. It is worth mentioning that at this flight condition, a significant shock-induced boundary layer separation is present, some experiments concluded that small fluctuations in surface pressure are present at this flight condition. Still, the simulation converged reasonably to a steady-state value, when the URANS mode was turned on, the simulation did not present any sustained unsteadiness. It is an indication that with the current approach, shock-buffet onset was not well predicted.

The C_P distributions computed with DLR-Tau are given in comparison with experimental data from NASA AMES [87]. The two spanwise locations inboard of the trailing-edge break ($\eta = 0.131 - 0.283$) show near identical match with the experimental results. In the mid-wing region ($\eta = 0.502 - 0.727$), the suction peaks, supersonic plateaus and pressure recoveries downstream of the shockwave are in good agreement with the experimental data. Some discrepancies are observed in the strength of the shockwave which is observed to be computed as stronger than what the experiments show. The indication is given by the more abrupt and sudden change in pressure at the shock location. Towards the wingtip ($\eta = 0.846 - 0.950$) similar observations can be made.

Overall, features of interest are well captured and reveal yet again the complex transonic aerodynamics on this transonic wing.

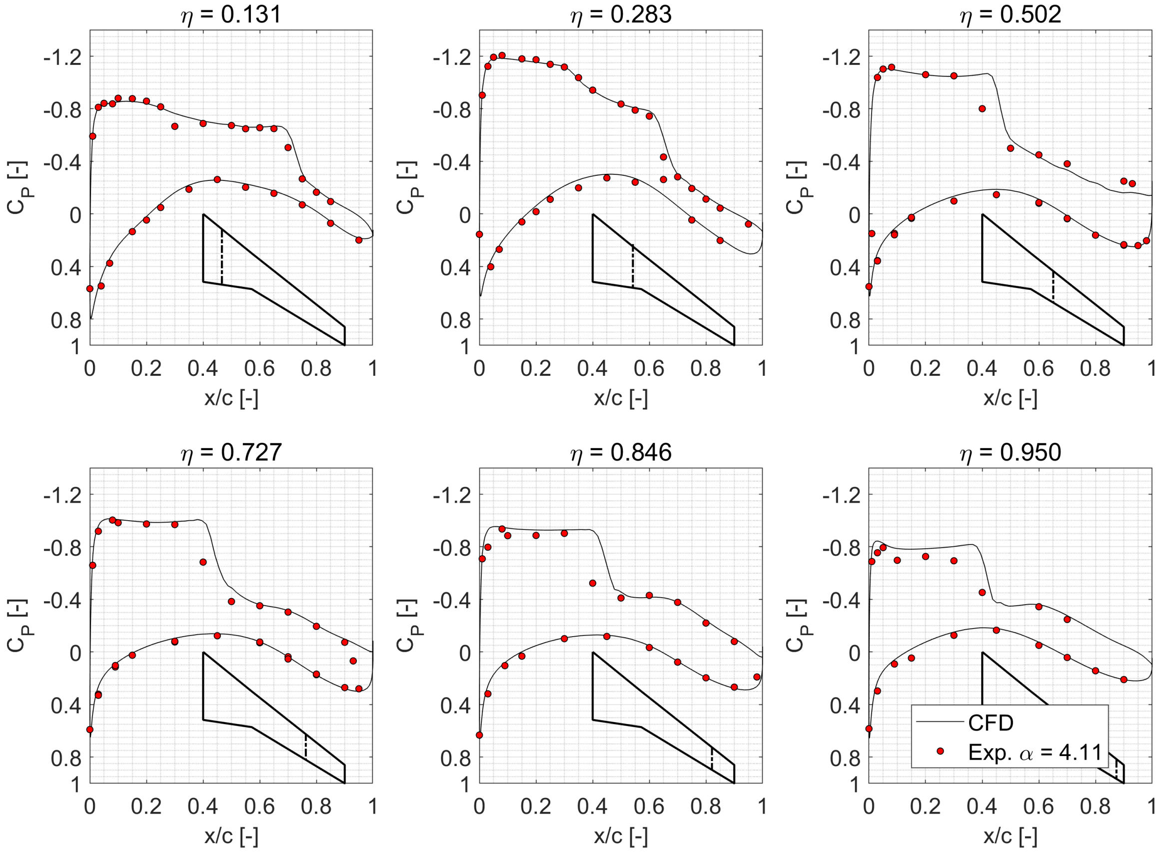

Fig. 6.4 Comparison of computed C_P at 6 η locations with experimental data from NASA AMES

Influence of timestep size

An important factor contributing to the validation of the current studies is the effect of timestep size on the computed shock-buffet response. The current timestep, Δt was set as 0.5 ms based on two key properties of the flow. Firstly, the convection time of a molecule of air, at freestream velocity, over the c_{mac} was calculated. The selected timestep results in approx. 50 timesteps per convection time. Secondly, the experimental shock-buffet St were used to compute the maximum expected frequency of the shock-buffet response. Again, the selected timestep resulted in 50 timesteps per highest expected buffet frequency. All of the time-marching simulations have been performed with a timestep $\Delta t = 0.5$ ms. The influence of the timestep is assessed by suddenly decreasing the timestep size to $\Delta t = 0.1$ ms. and running a portion of the simulation with this timestep. The two different buffet responses are investigated.

The effect of the timestep is shown in Fig. 6.5 by computed unsteady C_P signals at $M_\infty = 0.85$, $Re_{mac} = 5$ millions and an incidence α = 6°; and collected at the spanwise location of η =0.5. The two signals are nearly identical. The right hand side plot which shows the value of the standard deviation from the mean, C'_{Prms}, with respect to the x/c location, reveals similar patterns obtained with both timesteps. The insignificant change in amplitude of C'_{Prms} is local and does not impact the global dynamics of the flow. As a result, it was determined that the higher timestep was sufficient for the purpose of shock-buffet prediction since the project was time-constrained and limited resources were made available.

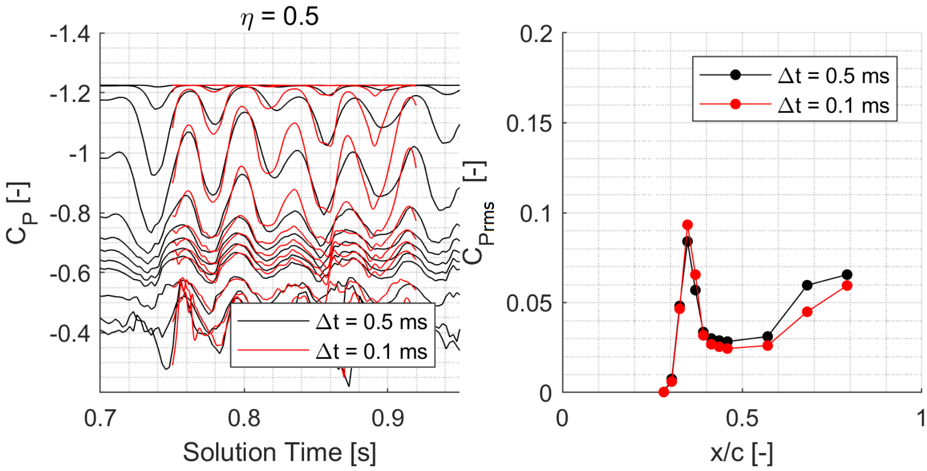

Fig. 6.5 The effect of Δt on the surface C_P signals

6.2.2 Prediction of shock-buffet at $Re_{mac} = 5$ million

In this section the results obtained at $Re_{mac} = 5$ million are introduced. The experiments conducted by Balakrishna and Acheson [30] revealed that, at these flight conditions, the NASA CRM exhibits buffet onset at an incidence $\alpha = 3°$. However, the fluctuations, then detected through wing root strain gauges remained small until the incidence was further increased to $\alpha = 5°$. Thus the authors concluded that the NASA CRM exhibits two shock-buffet regimes. A small amplitude fluctuation regime ($\alpha = 3$ to $5°$) and a deep shock-buffet penetration regime ($\alpha > 5°$). Similar observations were made by Koike *et. al.* and Sugioka *et. al.* at lower Re_{mac} [33][34]. This section introduces an analysis of simulations performed for the deep shock-buffet penetration regime.

Four time-marching simulations at incidences $\alpha = 4$, 5, 6 and 6.5° have been produced. No flow unsteadiness was captured in time-marching simulations at $\alpha = 4°$ or other attempts (not shown herein) at $\alpha = 3.5$ and 3.75°. This is a potential sign that our current approach as a dissipative characteristic and is unable to capture shock-buffet onset without further modification of numerical parameters.

Time-accurate aerodynamic coefficients

Time-accurate C_L, C_M and C_D are output. Figure 6.6 shows the evolution of C_L in time for incidences $\alpha = 5$, 6 and 6.5°. A comparison of computed mean C_L with mean experimental data is also included.

Knowing that each URANS simulation had a partly-converged RANS simulation as initialization, Fig. 6.6a reveals a transition between RANS and URANS solutions to occur in the first 0.2 - 0.3 seconds of simulated time. For the three incidences shown, steady-state RANS solution converged to a lower C_L than the mean of URANS solution. This observation is important as it shows that in this particular flight regime, computing the aerodynamics via steady RANS will result in lower values of C_L which may not reflect well the actual physics.

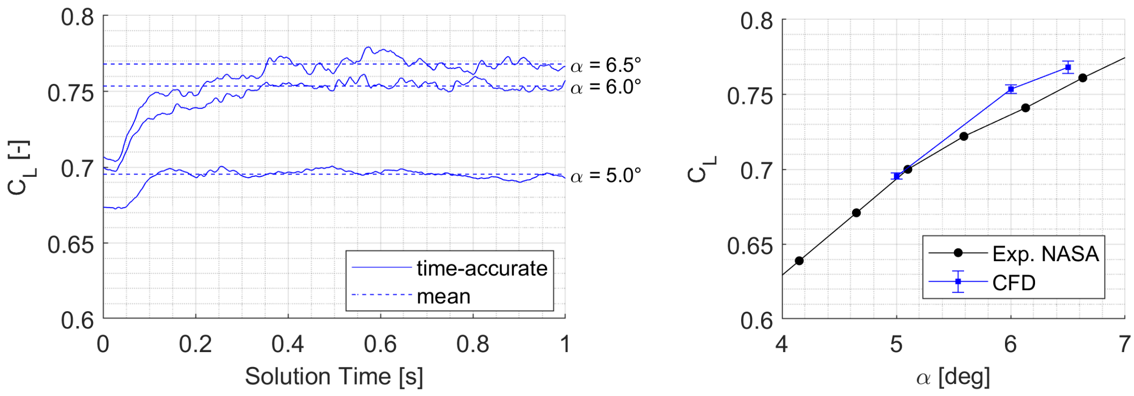

(a) time-accurate C_L **(b)** mean and fluctuation of C_L

Fig. 6.6 Evolution of NASA CRM C_L with incidence at $M_\infty = 0.85$, $Re_{mac} = 5$ million

After the transition stage, the time-accurate C_L shows significant unsteadiness at all three incidences. The unsteadiness is not easily identified as periodic such as previous shock-buffet results on other aircraft configurations (e.g. see Sartor and Timme [56]). Therefore, unsteady C_L is not a viable way of identifying shock-buffet on this aircraft.

In Fig. 6.6b a comparison between computed mean C_L and experimental mean C_L values from [88] is given. Error bars indicate the fluctuation,C'_{Lrms}, computed using a root-mean-square (RMS) approach. At $\alpha = 5°$, computed lift coefficient is in good agreement with the experimental value. The fluctuation in C_L is insignificant. At $\alpha = 6$ and 6.5°, the mean lift coefficient is overpredicted by about 1 to 2 lift counts. We define 1 lift count = 0.01 in C_L. The amplitude of fluctuation is visibly increasing with incidence. To put things into perspective, at $\alpha = 6.5°$, the $C'_{Lrms} = 0.01$ can translate in approximately 50 kN of force if we consider an aircraft the size of the CRM flying at 10,000 m altitude and $M_\infty = 0.85$.

C_D and C_M are plotted in Figs. 6.7 and 6.8. The transition stage in the first 0.2 seconds of simulated time is visible here too. Both quantities exhibit similar chaotic fluctuations. Note that a quantitative comparison between computed an experimental C_M is should not be performed because of wind-tunnel sting effects which are known to have an impact on the values of C_M recorded in the experiments [87].

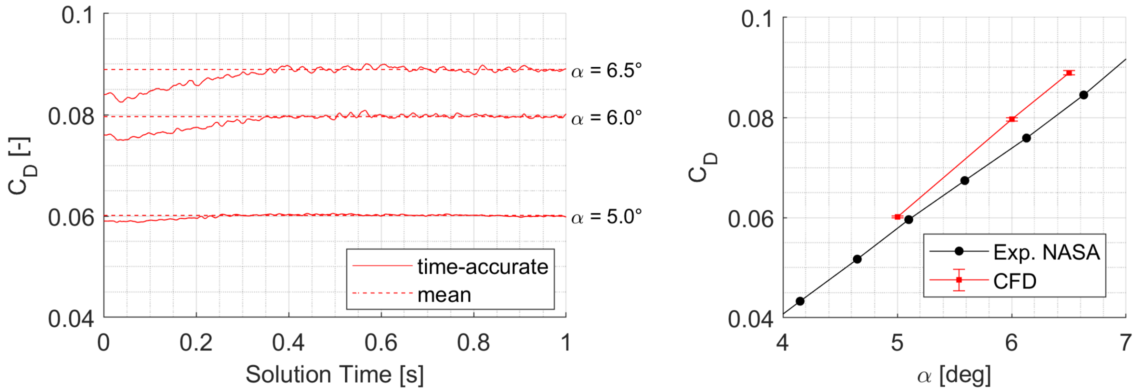

(a) time-accurate C_D **(b)** mean and fluctuation of C_D

Fig. 6.7 Evolution of NASA CRM C_M with incidence at $M_\infty = 0.85$, $Re_{mac} = 5$ million

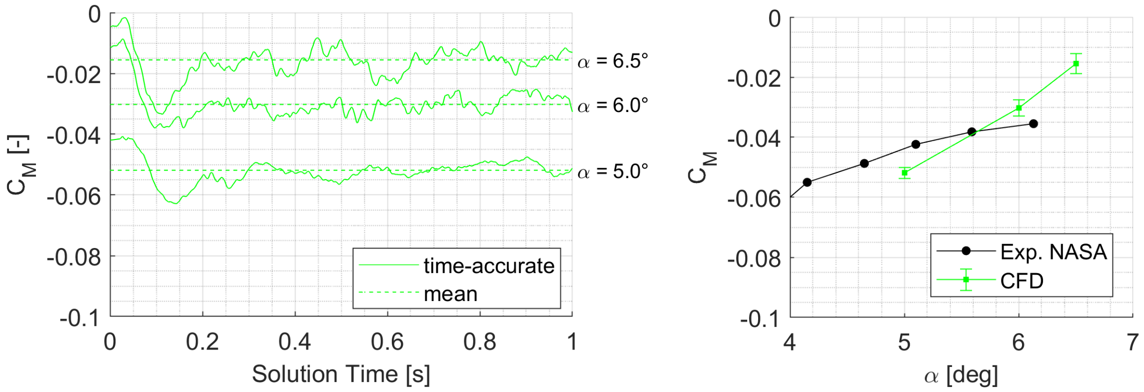

(a) time-accurate C_M **(b)** mean and fluctuation of C_M

Fig. 6.8 Evolution of NASA CRM C_M with incidence at $M_\infty = 0.85$, $Re_{mac} = 5$ million

Unsteady surface pressures

The numerical surface pressure probing described in Section 6.1.5 is used for on-the-fly monitoring of the simulations. It creates an opportunity to look for local signs of shock buffet while the simulation is still running: e.g. periodic oscillations in C_P at shock-location or specific frequencies expected during shock-buffet.

Figure 6.9 shows computed time-accurate surface C_P signals sampled by the probes located at $\eta = 0.6$. The results for incidences $\alpha = 5 - 6.5°$ are included. On the left hand side of Fig. 6.9, the C_P signals recorded in the last 0.5 seconds of simulated time are shown. This data is used to compute $C'_{P_{rms}}$ shown on the right hand side and the PSD maps given in Fig. 6.10.

At all three incidences similar patterns are present. A region in which C_P is steady is captured by the probes at the locations closest to the leading edge (e.g. $x/c = 0.186$). High amplitude fluctuations are present at $x/c = 0.335$ for $\alpha = 5°$; $x/c = 0.285$ for $\alpha = 6°$; and $x/c = 0.235$ for $\alpha = 6.5°$. The high amplitude fluctuation coincides with the location of the shock wave. Downstream the fluctuation dissipates. The frequency content is visibly composed of multiple frequencies. As shown in Fig. 6.10, at $\alpha = 5°$ a $St < 0.1$ is dominant; at $\alpha = 6$ and $6.5°$, multiple frequencies are present, of which $St = 0.6$ is also carried downstream towards the trailing-edge. The frequency content indicates that although there is one dominant frequency which is transmitted in the downstream direction, there is more than one frequency that contributes to the oscillation that occurs at the shock location. This is a typical characteristic of shock-buffet which is known to occur over a broadband of frequencies between $St = 0.1 - 0.6$.

Compared with the unsteadiness observed in the C_L, C_D and C_M, the unsteady C_P gives a better indication of shock-buffet presence. The evolution of C'_{Prms} with incidence (or C_L) plotted into one figure next to C'_P evolution captured on an early experiment by Roos [18] in Fig. 6.11. There is a similarity in both.

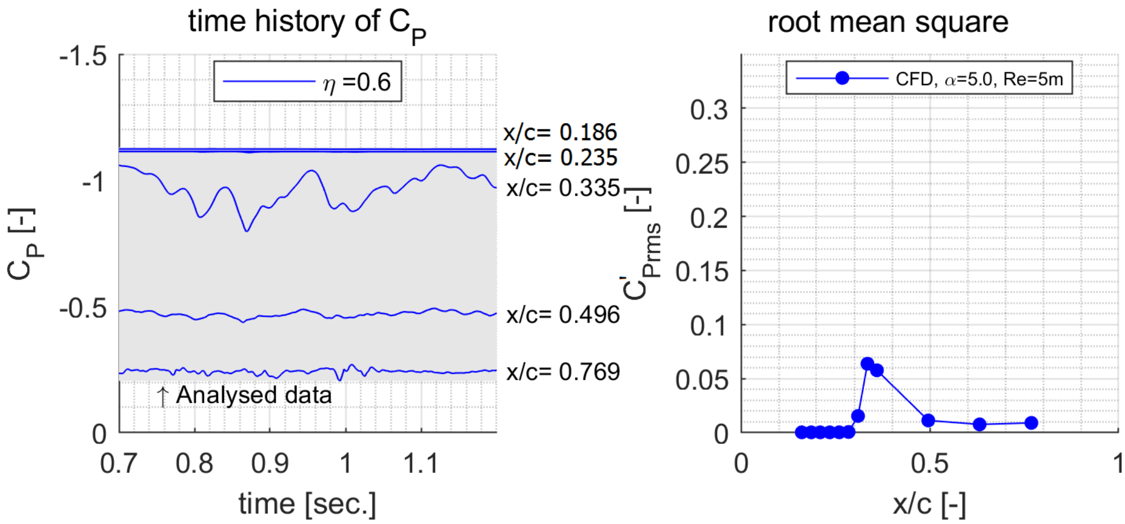

(a) $\alpha = 5.0\,^\circ$

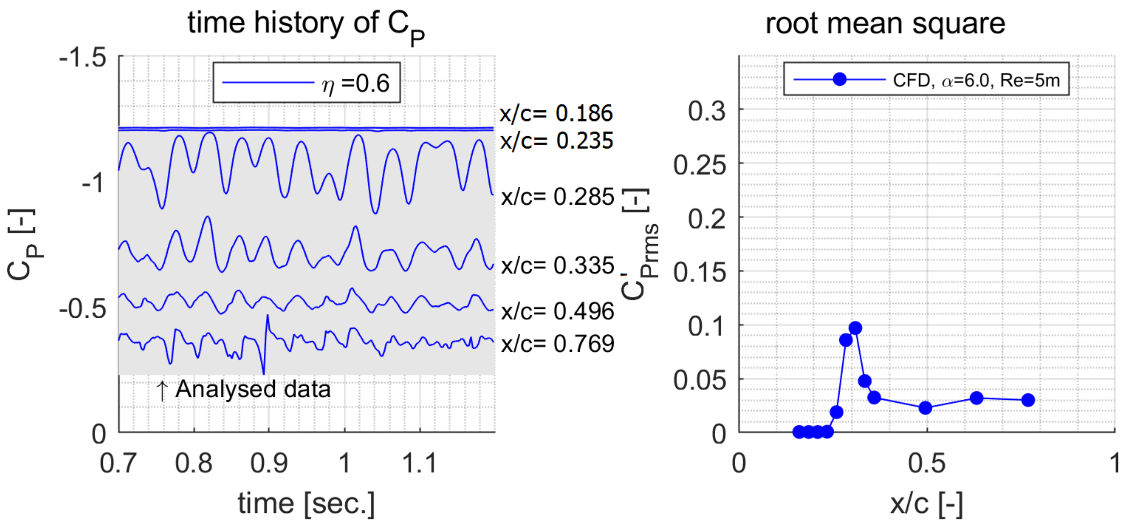

(b) $\alpha = 6.0\,^\circ$

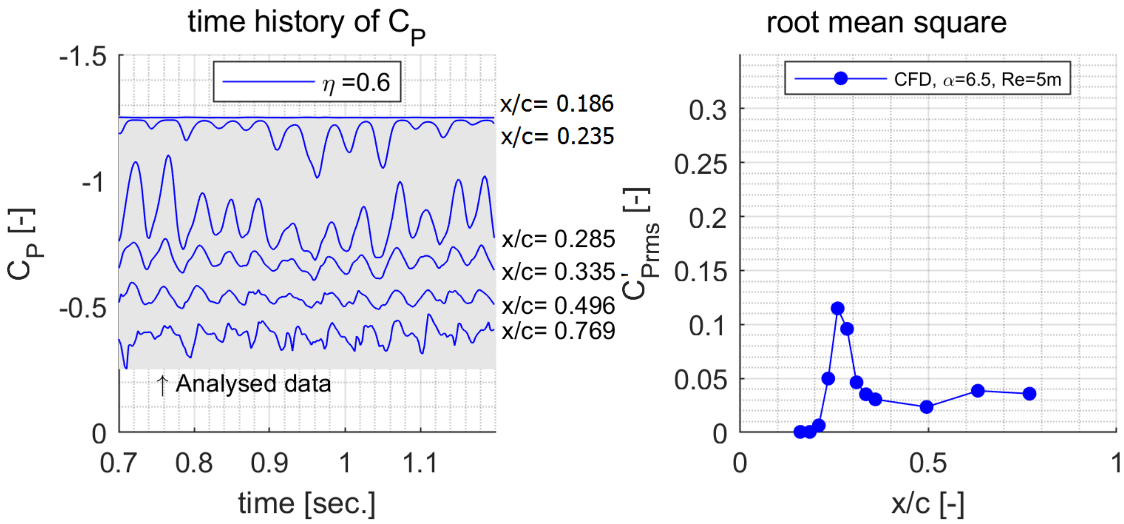

(c) $\alpha = 6.5\,^\circ$

Fig. 6.9 Surface C_P response at η = 0.6, and various incidences

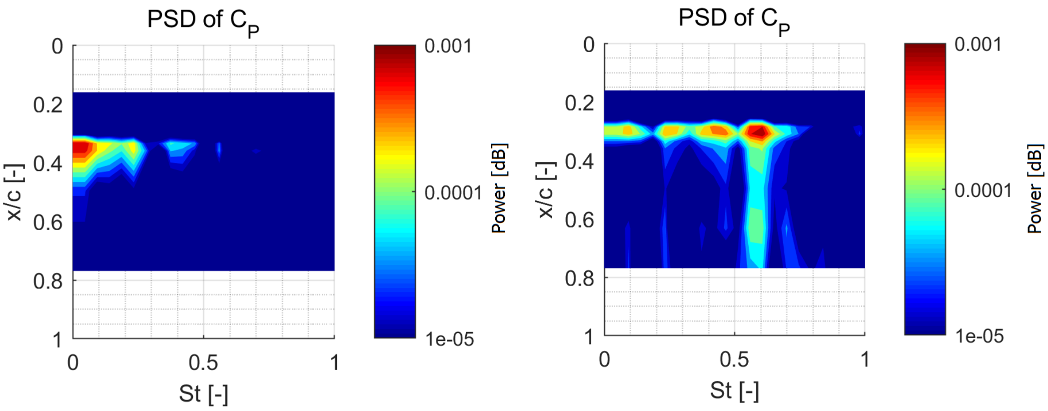

(a) α = 5.0 °　　**(b)** α = 6.0 °

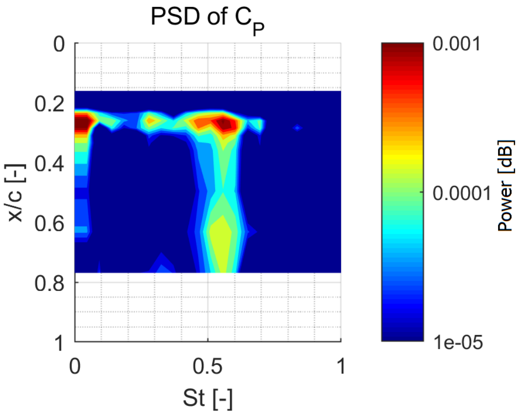

(c) α = 6.5 °

Fig. 6.10 Surface C_P response at η = 0.6, and various incidences

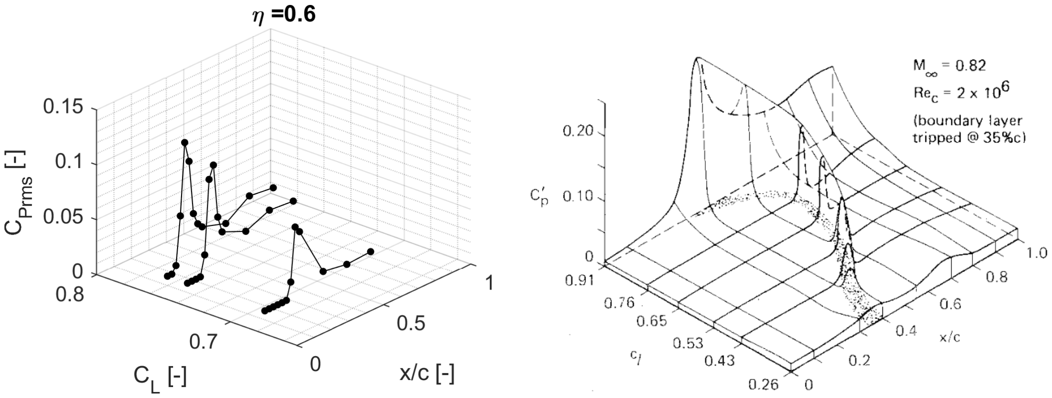

(a) present study　　**(b)** Roos' [18] observation

Fig. 6.11 Comparison between computed C'_{Prms} and an early epxerimental observation

Surface characteristics shock-buffet

The surface data is output every 5 time steps (*f = 400 Hz; St = 9.5*) for a period of 0.5 seconds of simulated time. The results obtained for an incidence $\alpha = 6°$ are used to determine the surface characteristics of the shock-buffet phenomenon exhibited by this aircraft configuration.

Figure 6.12 shows computed surface C_P at 9 instances over one period of the $St = 0.6$ oscillation. Isolines of $C_{Fx} = 0$ are superimposed. C_{Fx} is a measure of the shear stress on the surface and correlates to the direction of the flow. The area inside the $C_{Fx} = 0$ isoline shows the location where air flows in the direction opposite of the freestream flow, hence an indication of boundary layer separation. The contours reveal typical characteristics of transonic aerodynamics. An area of low C_P is present towards the leading edge of the wing where the air forms supersonic pocket. This area terminates in a shock which is interpreted on the surface as a sudden increase in pressure. The shock front can then be easily visualised.

In each of the 9 time snapshots shown, the shock front (the line across which pressure increases suddenly) is observed to be wavy. This result is qualitatively similar with the numerical results of Iovnovich and Raveh [35] who first numerically captured observed the wavy three-dimensionality of shock-buffet and pioneered the term *buffet cell* to describe this waviness (please refer to Section 2.4.5, Fig. 2.29).

The C_{Fx} isoline indicates that separated flow is present from the shock foot and propagates downstream over a significant part of the wing where the adverse pressure coefficient across the shock are the largest. It too varies in time with no distinctive feature.

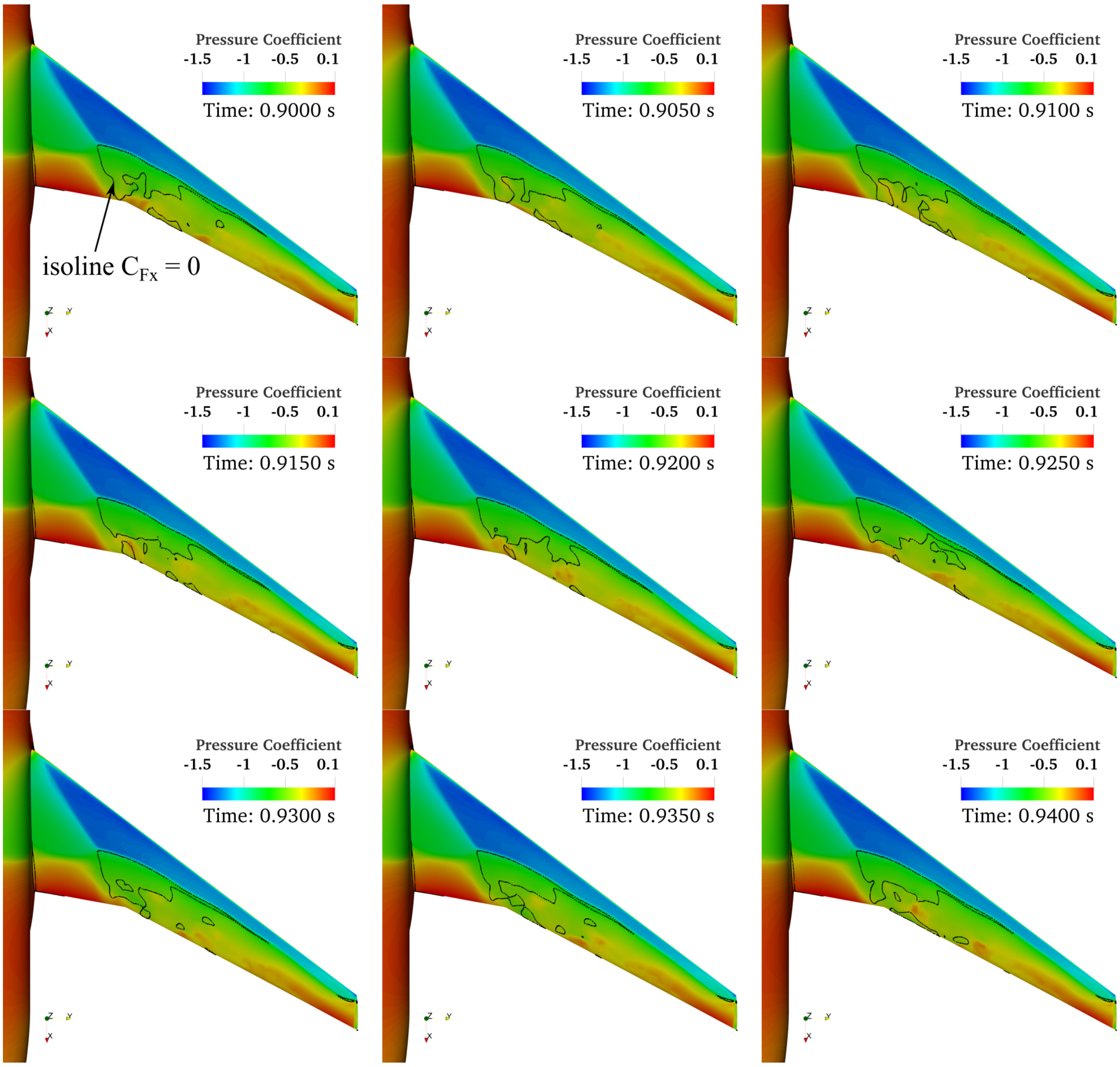

Fig. 6.12 Time-accurate computed surface C_P at M = 0.85, Re_{mac} = 5m, α = 6.0 °

Figure 6.13 gives contours of $C'_P = C_P - C_{Pmean}$. Alternating values of C'_P at the shock front location give birth to *buffet cells* and indicate if the local shock position is upstream ($+ve$ C'_P) or downstream ($-ve$ C'_P) when compared to its mean location. The spanwise convection of the shock is more visible in this form of visualisation. Moreover, it is clear that the region inboard of the trailing-edge break is not affected by shock buffet, fluctuations are present mainly in the mid-wing region. Significant unsteadiness is visible downstream of the shock front where flow separation occurs. Alternating C'_P signs in the chordwise direction is a possible hint of periodic separation bubbles that form behind the shock, travel downstream and then shed from the trailing-edge in the form of vortices.

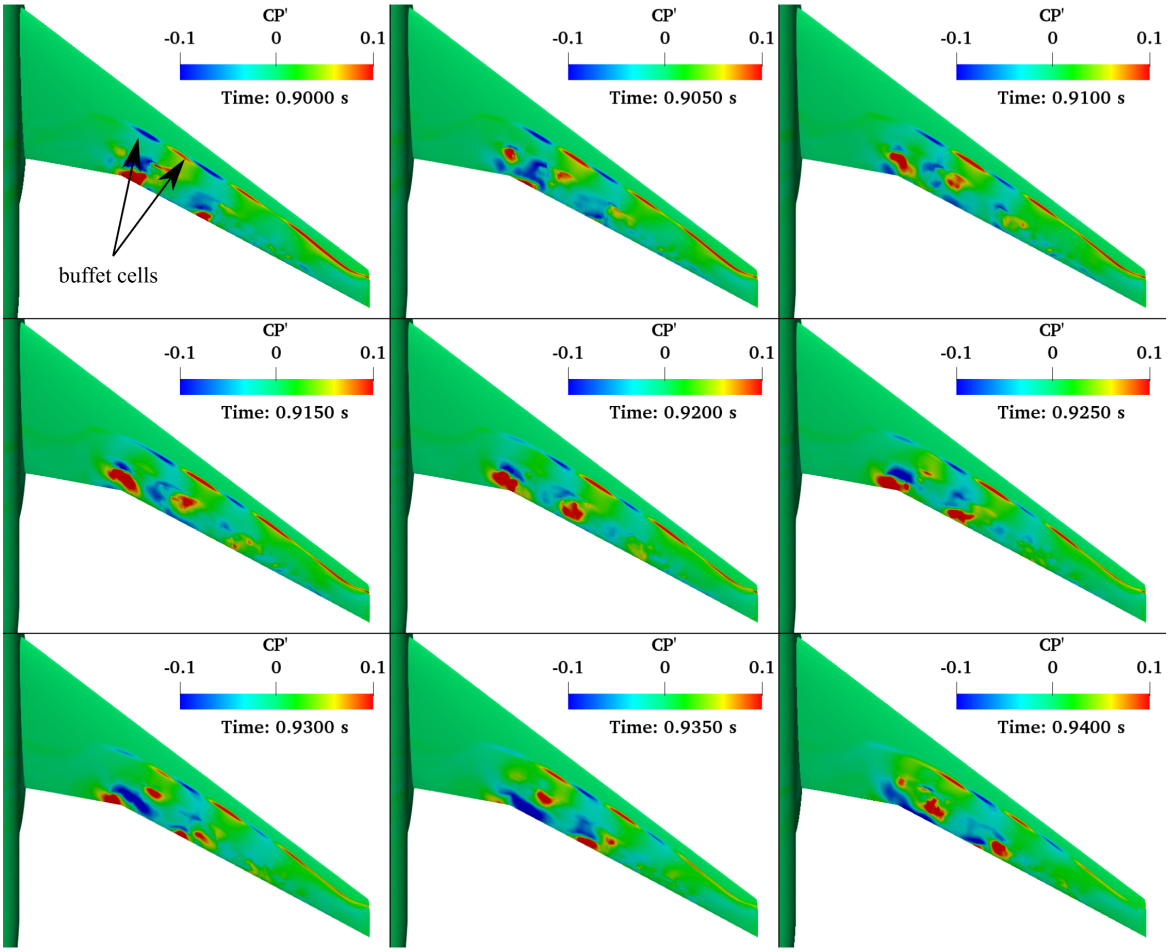

Fig. 6.13 Computed buffet cells ($C_P' = C_P - C_{Pmean}$) at M = 0.85, Re_{mac} = 5m, α = 6.0 °

Analysis of the buffet cells from Fig. 6.13 confirms that the dominant frequency of oscillation is $St = 0.5 - 0.6$, which is at the higher spectrum of shock-buffet frequencies observed in previous experiments and numerical investigations. The wavelength of the spanwise convection is $\lambda = 0.2\, b/2$ and the convection speed $U_c = \lambda f = 0.4 - 0.5 U_\infty$.

At this value of Re_{mac} no detailed experimental shock-buffet data exists. A more in-depth comparison with experiments will be performed in a subsequent section with the results obtained at $Re_{mac} = 1.5$ and 0.95 million. However, time-accurate and mean C_P slices at 6 location outboard of the trailing-edge break are compared with mean C_P experimental values in Fig. 6.14. With regards to the mean C_P, Fig. 6.14 shows a reasonably good agreement. Shock location is only minimally upstream at $\eta = 0.727 - 0.846$, the suction peaks, pressure recoveries and pressure sides are well captured. The time-accurate lines reveal that at $\eta = 0.502 - 0.95$ the shock oscillates. Significant fluctuations are also captured in the pressure recoveries region at $\eta = 0.397 - 0.272$ just like Fig. 6.13 revealed too. Interestingly, the oscillations that occur on the suction side of the wing also give birth to oscillations on the pressure side. Most significantly, at $\eta = 0.502 - 0.603$, some form of fluctuation in the trailing-edge loading on the pressure side of the wing is observed.

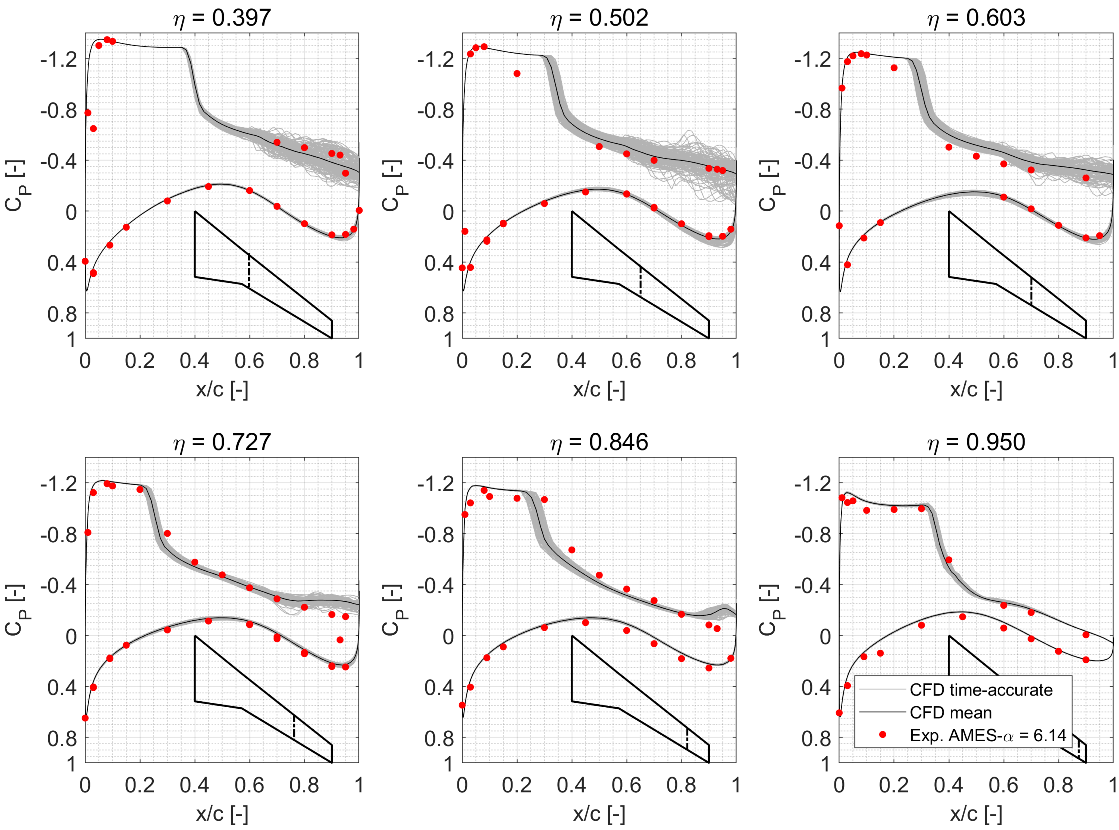

Fig. 6.14 Computed time-accurate and mean C_P at $M = 0.85$, $Re_{mac} = 5\text{m}$, $\alpha = 6.0°$ in comparison with mean experimental values from [88]

Flow field characteristics shock-buffet

The benefit of using CFD over experimental methods is that detailed flow field data is easily extracted and can help produce new insights that cannot always be observed in the experiments. For this purpose, flow field data, computed at an incidence $\alpha = 6°$, is output every 5 time steps (*f = 400 Hz; St = 9.5*) for a period of time of 0.1 seconds (2.5 periods of highest St identified). This section analyses the shock buffet characteristics that can be observed in the flow field and how they correlate with those found in the previous section (Section 6.2.2).

Shock information is extracted using isosurface of $M_{normal} = 1$ criterion developed by Lovely and Haines [93]. M_{normal} is defined as the dot product between the pressure gradient and Mach vectors: $M_{normal} = \vec{M} \cdot \nabla P$. The reasoning behind this criterion is that, in transonic flow, the air decelerates from supersonic to subsonic velocity when it crosses a shock. Therefore, at some location, M_{normal} across the shock will be 1. Although this method is not perfect, it is still well received as one of the most popular algorithms for shock extraction and is widely used [94].

Figure 6.15 shows multiple views of the extracted $M_{normal} = 1$ isosurface coloured by the local value of M. The top and front views (Figs. 6.15b and 6.15c) offer an insight into the characteristics of the shock.

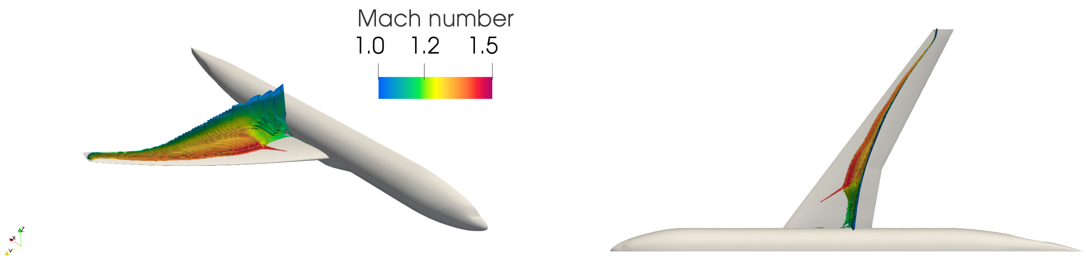

(a) 3D **(b)** top view

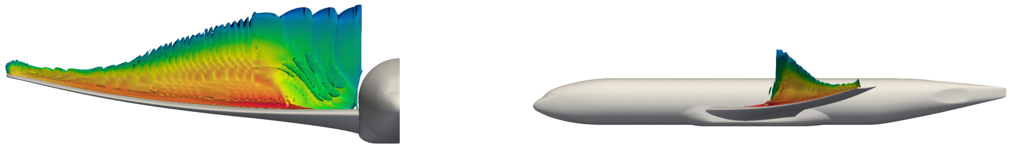

(c) front view **(d)** side view

Fig. 6.15 Computed isosurface of $M_{normal} = 1$ shock detection criterion coloured by Mach number magnitude, freestream conditions of M = 0.85, Re_{mac} = 5m, α = 6.0°

In Fig. 6.15b, the shock is visible to be present across the whole span of the wing. Nearer the wing root, two shocks are identified that merge into one, giving the shock-front a λ shape. The M contours give information about the strength of the shock. Since air must decelerate from supersonic M to subsonic, the higher the M before the shock, the more the air must decelerate and the stronger the adverse pressure gradient. From Fig. 6.15c the shock is observed to be stronger outboard the trailing-edge break and near the surface of the wing. Local M exceed 1.5 at some locations. By putting together the information from Figs. 6.12 and 6.15, the boundary layer separation is related to the strength of the shock, as it appears where the shock is strongest.

However, all mentioned above are common characteristics of transonic aerodynamics of aircraft wings. For the purpose of analysing the flow field dynamics of shock-buffet, 6 slices of the shock isosurface are shown, for two time steps, in Fig. 6.16.

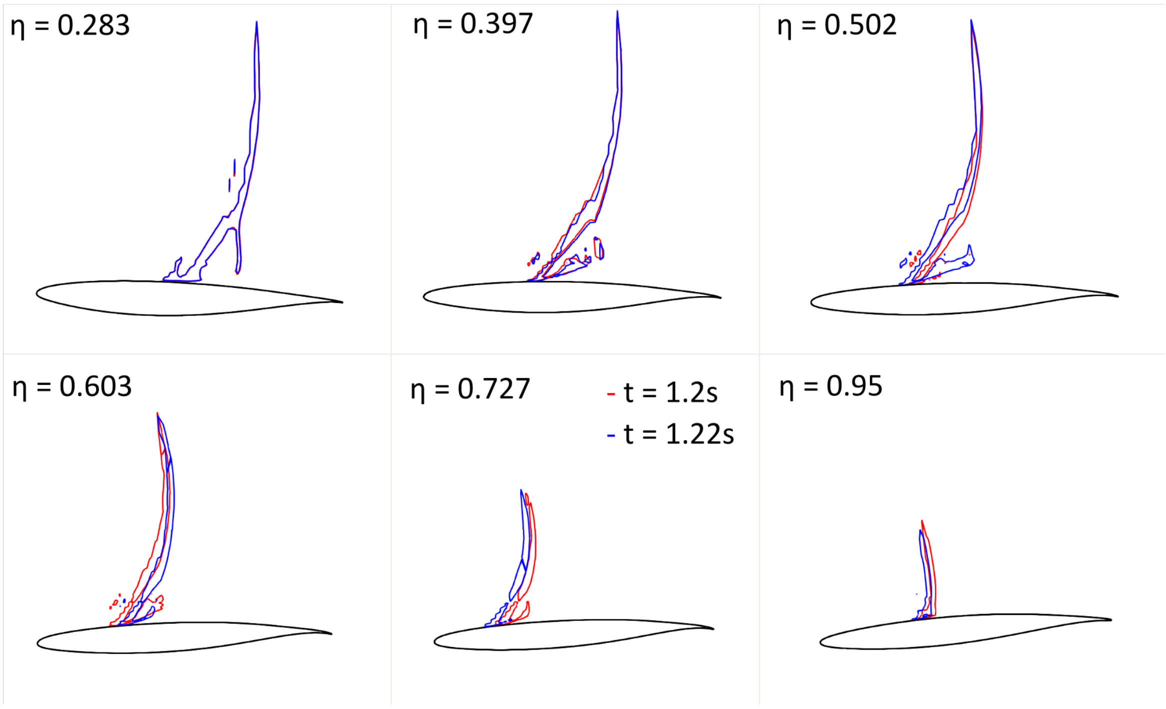

Fig. 6.16 Spanwise slices of the shock isosurface at two points in time

The images are separated in time by half a period of the $St = 0.6$ frequency. This figure gives a new insight into local shock dynamics. Focusing on $\eta = 0.397$ and 0.603, the shock at $t = 1.22$s appears to be downstream compared to its location at $t = 1.2$s. However, for $\eta = 0.502$ and 0.727, the opposite is true. The shock, which can be said to be in anti-phase at different spanwise locations correlates well with the buffet cells we observed in Fig. 6.13. Although the displacement of the shock varies along the span, at all locations, the shock moves entirely, and not only near the surface of the wing. The shape of the shock is also singificantly different at different locations. Inboard of the trailing-edge break ($\eta = 0.283$) The shock foot has a λ shape. At $\eta = 0.397 - 0.727$, the foot of the shock is displaced from the surface, possibly due to a local thickening of the separated boundary layer. At $\eta = 0.95$, the shock appears to be normal to the wing surface.

A final aspect of shock-buffet dynamics that has not been discussed yet is the behaviour of the shock-induced separation that was first identified through C_{Fx} isolines in Fig. 6.12. Isosurfaces of Q criterion (second invariant of the velocity gradient tensor) are used to visualise vortical structures in Fig. 6.17. Two vortices with core spanning in the X direction are identified: one forming at the wingtip and one at the trailing-edge break. In between successive vortex shedding appears to occur, spanning a significant portion of the wing. Compared to the study in Chapter 4, the flow remains partially or fully separated at all time, and does not fully reattach.

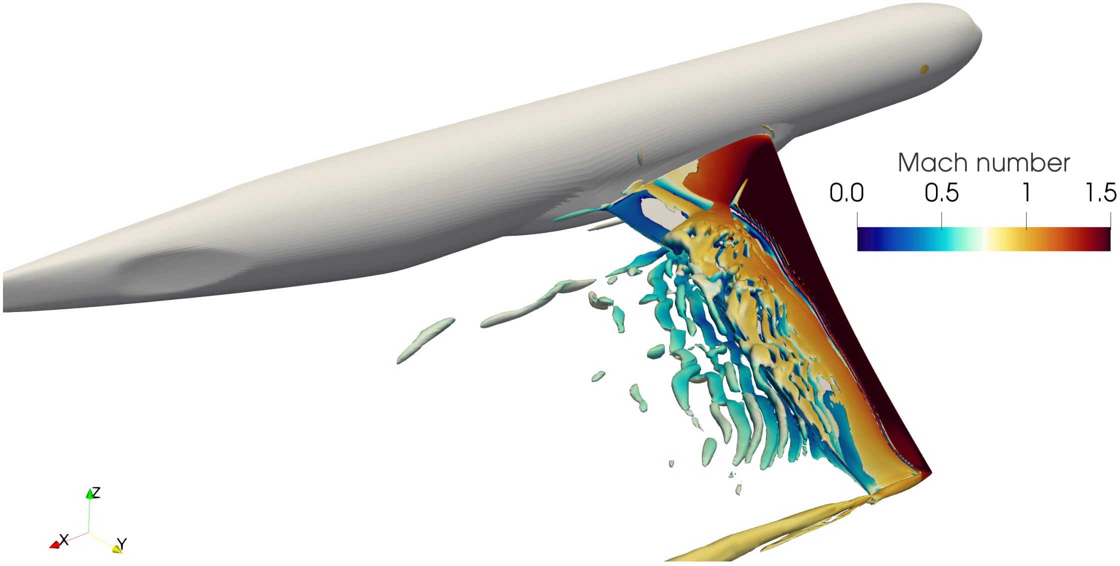

Fig. 6.17 Isosurfaces of $Q = 10,000$ coloured by M. Computed for $M = 0.85$, $Re_{mac} = 5$ million and $\alpha = 6°$; $t = 1.2$s

6.2.3 Reynolds number effects on shock-buffet

The value for Re_{mac} is reduced to 1.5 and 0.95 million to replicate experimental conditions from the JAXA wind tunnel campaigns published in [33] and [34]. The aim is to produce an analysis of the Re effects on shock-buffet over this particular configuration. Koike *et. al.* [33] found in their experiments that a decrease in Re_{mac} resulted in a shock displacement towards the leading edge and a reduction in surface pressure fluctuation measured. However, in their study, the wind tunnel model deformed differently at the tested Re. As such, it is unclear which of the two effects identified were caused by a change in Re or by model deformations.

The current CFD study assumes a rigid model, eliminating any aerodynamic effects due to wing deformations. In a recent 2019 study, Masini *et. al.* [58] similarly simulated the RBC12 aircraft (See section 2.4.5) at $Re_{mac} = 3.75$ and 27 million. They identified the shock displacement coupled with a change in fluctuation levels of C_L. However, their study was limited to shock-onset region and did not address the aerodynamics during deep penetration into shock-buffet.

Three simulations are compared in this section. The NASA CRM is simulated at $M_\infty = 0.85$, $\alpha = 6°$, and $Re_{mac} = 0.95$, 1.5, and 5 million. For the lower Re_{mac} values of 0.95 and 1.5 million, a thicker boundary layer is expected. The grid, presented in Section 6.1.2 is modified by increasing the height of the cells nearest to the aircraft surface from $2.83 \cdot 10^{-5}$ to $9.83 \cdot 10^{-5}$ meters. Therefore a similar $y^+ = 0.85$ distribution is maintained.

Computed time-accurate lift coefficients, their mean, and RNS values are given in Fig. 6.18.

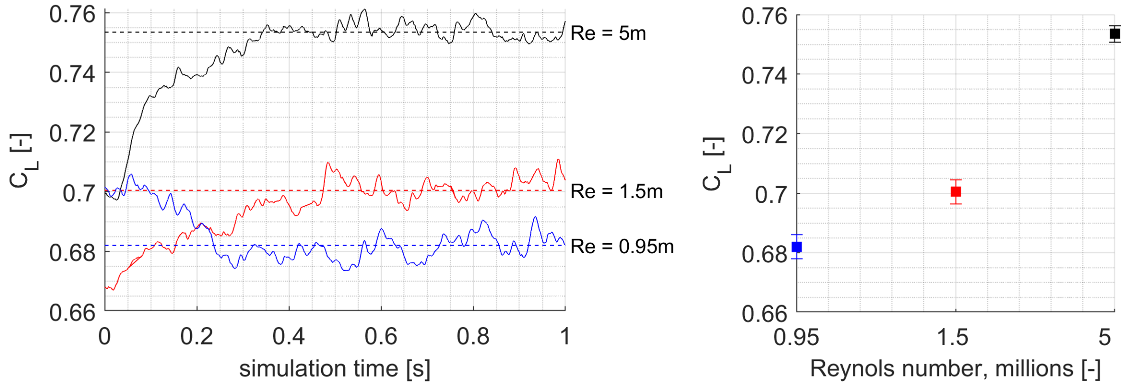

(a) time-accurate C_L

(b) mean and fluctuation of C_L

Fig. 6.18 Evolution of NASA CRM C_L with change in Re_{mac} at $M_\infty = 0.85$ and $\alpha = 6°$

The mean C_L values decrease with Re_{mac}. The mean value at $Re_{mac} = 0.95$ million is of approximatively 8 lift counts lower than its equivalent at the highest Re_{mac} simulated. The opposite is seen in the RMS of fluctuation values (error bars in Fig. 6.18b). At lower Re_{mac}, the $C'_{L_{rms}}$ values increase by up to 40% when compared to their values at $Re_{mac} = 5$ million. The lower value of C_L is attributed to a forward displacement of the shock that results in a lower loading over the wing. This can be observed in Fig. 6.19 which gives contours of computed mean C_P at the three Re_{max} simulated. The topologies are similar at all three Re_{mac}, however a clear displacement of the shock towards the leading-edge is visible.

To analyse shock-buffet dynamics, $C'_{P_{rms}}$ contours are shown in Fig. 6.20. At $Re_{mac} = 0.95$ and 1.5 million, the fluctuations along the shock seem higher and over an extended portion of the wing's span and chord than those computed at $Re_{mac} = 5$ million. Figure 6.20 essentially shows that at lower Re_{mac}, the shock wave fluctuates over a longer chordwise extent, resulting in a higher fluctuation in aerodynamic loads, which explains why C_L fluctuates more as Re_{mac} is reduced.

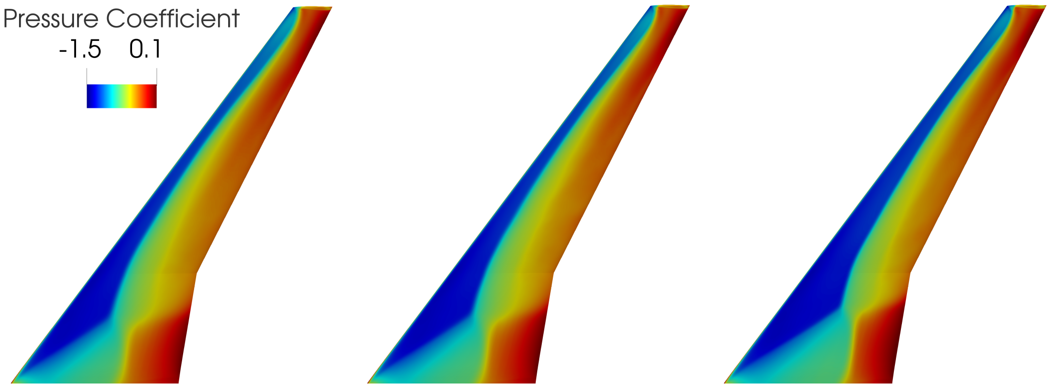

(a) $Re_{mac} = 0.95$ million **(b)** $Re_{mac} = 1.5$ million **(c)** $Re_{mac} = 5$ million

Fig. 6.19 Reynolds number effect on computed mean C_P

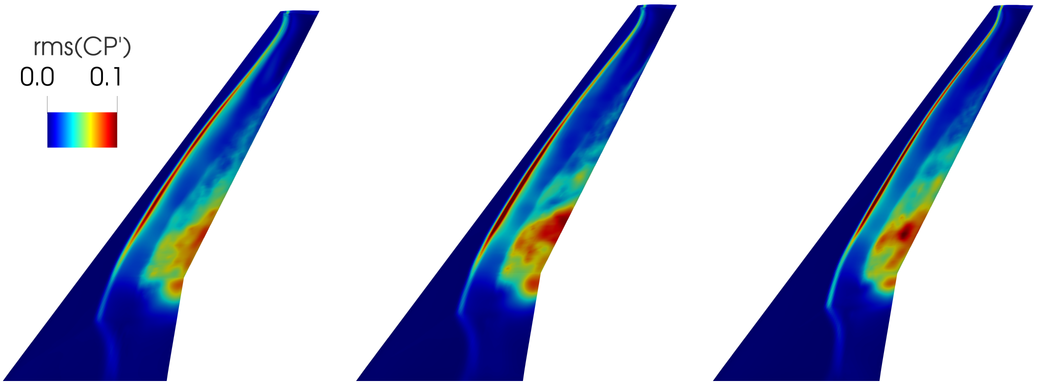

(a) $Re_{mac} = 0.95$ million **(b)** $Re_{mac} = 1.5$ million **(c)** $Re_{mac} = 5$ million

Fig. 6.20 Reynolds number effect on computed $C'_{P_{rms}}$

The effect of Re_{mac} on surface pressure fluctuations is summarised in Fig. 6.21 which shows, superimposed for all Re_{mac}, the location and magnitude of maximum pressure fluctuation along the shock front. The results computed at $Re_{mac} = 0.95$ and 1.5 million are almost identical. The results computed for $Re_{mac} = 5$ million are visibly located further downstream from wing root to $\eta = 0.7$. These results confirm the experimental observation that a reduction in *Re* will result in a shock displacement towards upstream, however, they show that it is not necessarily coupled with a reduction in pressure fluctuation. On the contrary, at higher *Re*, the shock is observed to fluctuate less. Similar observations were made by other computational results presented in Section 2.4.5.

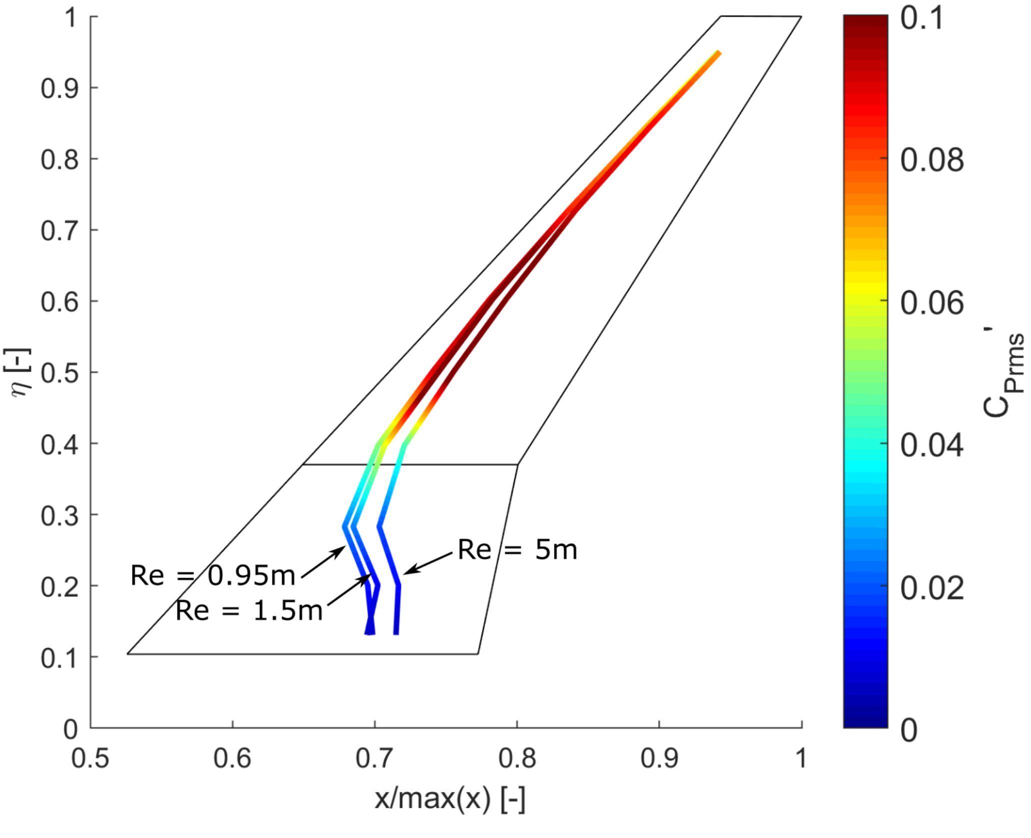

Fig. 6.21 Position of shock-front at different Re

Surface C_P is also sampled in the fashion described in Section 6.1.5 and analysed at $\eta = 0.5, 0.6$, and 0.7. The PSD of C_P at the location of maximum fluctuation are shown in Fig. 6.22. The results do not show any trends with regards to frequency changes due to *Re*. At $Re_{mac} = 1.5$ million, the shock fluctuates with the dominant frequency of St = 0.46. The highest frequency recorded is at $Re_{mac} = 5$ million and is equal to St = 0.6. At $Re_{mac} = 0.95$

million, the dominant shock fluctuation frequency is St = 0.5, in between the other two recorded values. Thus, this numerical study cannot provide any conclusive results other than the fact that at lower values of Re, a lower frequency of oscillation can be expected.

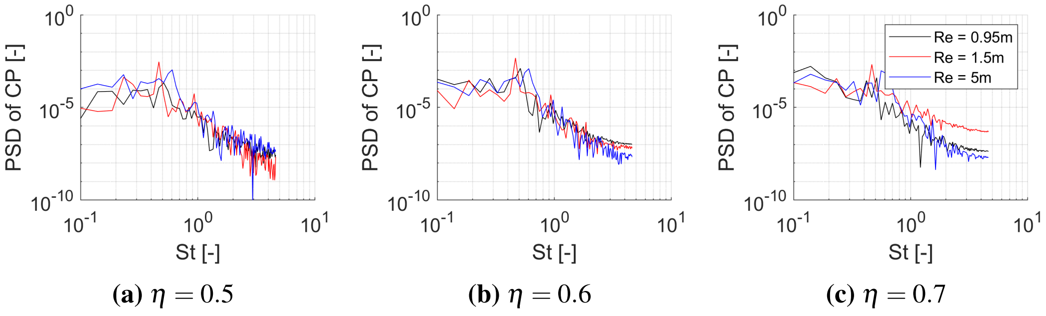

(a) $\eta = 0.5$ **(b)** $\eta = 0.6$ **(c)** $\eta = 0.7$

Fig. 6.22 Reynolds number effect on buffet frequency

6.3 Lessons learnt and conclusions

This chapter presented a numerical study focused on the prediction of the shock-buffet phenomenon on the NASA CRM aircraft. The DLR-Tau solver was used to produce time-marching simulations by solving the URANS equations closed with the SSG/LRR-g RSM turbulence model. New insights into the shock dynamics were developed, a fair qualitative and quantitative comparison with experimental data was performed. The effects of Reynolds numbers have been alalysed.

The aircraft was first simulated at $M = 0.85$, $Re_{mac} = 5$ million, and incidences $\alpha = 4 - 6.5°$. The aerodynamics during deep penetration into shock-buffet regime were investigated. Unsteady surface sampling provided information with regards to local shock-buffet characteristics. Pressure fluctuations, characterised by multiple dominant frequencies, between $St = 0.1 - 0.6$, were present at shock-front location. Buffet cells contours revealed that the shock oscillates in the spanwise direction, giving birth to a waviness in the shock-front. Flow field data was analysed and provided new insights into the movement of the shock near and far from the wing surface. A good correlation between the findings in the surface and flow field was found.

The Reynolds number effects were analysed by reducing Re_{mac} to 1.5 and 0.95 million to replicate experimental conditions from [33] and [34]. The results from the present study confirmed that at lower values of Re_{mac}, the shock was displaced towards the leading-edge, however, contrary to the experimental observations, the fluctuations were seen to increase at lower Re. This is possibly explained by the fact that lower values of Re coincide with lower momentum of the travelling fluid. Thus, viscous interactions, including boundary layer separation, are stronger.

Chapter 7

Conclusions

This thesis presented an in-depth analysis of the ability to predict shock-buffet using Computational Fluid Dynamics (CFD). The shock-buffet phenomenon is an unsteady shock wave/boundary-layer interaction (SWBLI) characterised by self-sustained, periodic shock movement in transonic flow. It can be present at all Reynolds numbers (Re) at combinations of high Mach number (M) and/or incidence (lift). It was shown in previous research to result in significant aerodynamic load fluctuations. Since, unlike CFD and stiff wind tunnel models, real aircraft have an elastic structure, the load fluctuation associated with shock-buffet could result in airframe vibrations that directly translate in passenger discomfort, poor handling qualities or risk of structural failure. Shock-buffet was found to be an industrially relevant phenomenon, since the majority of today's commercial aircraft have their design point in transonic flight. Thus, regulatory authorities (e.g. *Civil Aviation Authority* in the UK) require aircraft manufacturers to provide evidence that shock-buffet will not compromise the integrity of their airplanes at any point within their design flight envelopes.

The status quo in this field revealed that there is a great uncertainty with regards to prediction of shock-buffet onset and characteristics by Unsteady Reynolds-averaged Navier-Stokes-based (URANS)simulations, particularly when using eddy-viscosity turbulence models. Since RANS-based simulations are most commonly used in the industry, the current project investigated alternative turbulence modelling approaches. This thesis evaluated the use of second-moment closures, the full Reynolds Stress Models (RSM), in this particular fluid flow scenario. Although known to provide advanced modelling of turbulence, the RSM is still not widely used due to increased cost, poor convergence, and stability issues.

This project was be divided into three key investigations:

1. **Chapter 4. Performance of the RSM closures in 2D shock-buffet prediction:** the OAT15A was simulated at $M_\infty = 0.73$ and chord $Re_c = 3$ million. Accuracy of two RSM variants was investigated by comparison with experimental data.
2. **Chapter 5. Prediction of design point aerodynamics and shock-induced separation on the NASA Common Research Model (CRM) wing-body aircraft:** the wing-body NASA CRM was simulated using a steady RANS approach at $M_\infty = 0.85$, chord $Re_{mac} = 5$ million, and incidences between 2.5 and 6°. The results were compiled to complement those from the AIAA CFD Drag Prediction Workshops (DPW).
3. **Chapter 6. Characterisation of shock-buffet on the NASA CRM:** the wing-body NASA CRM was simulated using unsteady RANS approach at $M_\infty = 0.85$, three chord $Re_{mac} = 0.9$, 1.5 and 5 million, and incidences higher than 4°. Computed shock-buffet characteristics were compared with experimental observations.

The key outcomes are given in more detail in the sections below.

7.1 Performance of the RSM closures in 2D shock-buffet prediction

Based on the test case conducted experimentally by Jacquin *et. al.* [23]. The OAT15A supercritical aerofoil, shown in Fig. 7.1, was simulated at $M_\infty = 0.73$ and $Re_c = 3$ million. The objectives were to identify whether any variant of RSM available in ANSYS Fluent CFD code can be used to accurately and reliably capture shock-buffet.

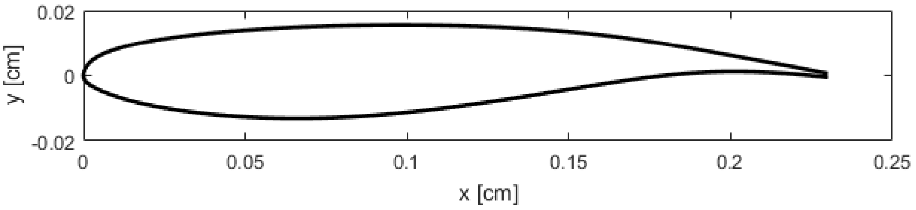

Fig. 7.1 The OAT15A aerofoil geometry

In [23], shock buffet was documented at incidences, α between 3.1 and 3.9°, with emphasis on the results obtained at 3.5° of incidence.

Block-structured grids were generated, a turbulence modelling study at $\alpha = 3.5°$ discarded the use of $k - \omega$ *SST* as shock-buffet was not captured. Two variations of the RSM were tested: the *Linear Pressure-Strain* [74][73] and the *Stress-Omega* [75] RSM. Computed results showed that both variations of RSM predicted the self-sustained shock-buffet phenomenon, however, only the Stress-Omega RSM accurately predicted the shock location. Both predictions had overpredicted frequency of oscillation by 10-20% when compared to experimental data. Figure 7.2 gives a an overview of current predictions, other numerical predictions from literature and original experimental data by comparing mean pressure coefficients and amplitude of fluctuation on the suction side of the aerofoil.

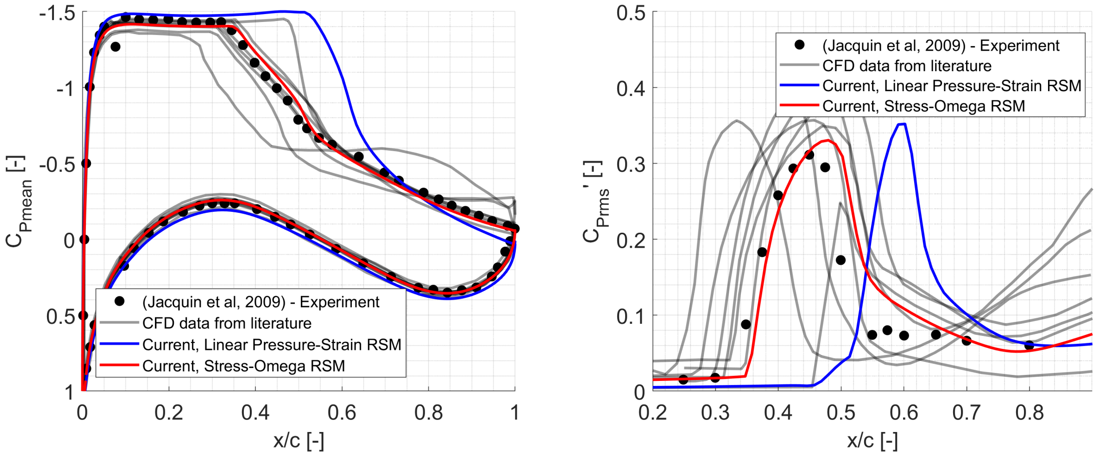

(a) mean pressure coefficient **(b)** RMS of fluctuation

Fig. 7.2 Comparison of current predictions, literature numerical predictions and experimental pressure coefficients on the OAT15A aerofoil at $M_\infty = 0.73$, $Re_c = 3$ million, and $\alpha = 3.5°$.

The robustness of the two RSM variants was tested by simulating the aerofoil at incidences $\alpha = 3.1$, 3.25, and 3.9°. Both predictions had computed shock-buffet at all incidences. The results obtained with Stress-Omega RSM compared well with the experiments. Those obtained with the Linear Pressure-Strain RSM consistently predicted the shock location further downstream than observed in the experiments. Qualitatively, both sets of results correlated well over the range of incidences chosen. The overall trends were well captured, including an increase in amplitude of fluctuation.

Aside the results reported, this study helped understand the challenges associated with using RSM as a turbulence closure. The Stress-Omega RSM, although more accurate, was challenging to converge, and was found to be very sensitive to numerical parameters and meshing strategy. On the other hand, the Linear Pressure-Strain RSM had less stability issues, almost always converging to the same solution on grids of similar size. None of the issues encountered in the simulations ran with the RSM turbulence closures were found in the simulations ran with the $k-\omega$ SST turbulence model.

7.2 Prediction of design point aerodynamics and shock-induced separation on the NASA CRM wing-body aircraft

The *NASA Common Research Model* (CRM), shown in Fig. 7.3 in its wing-body/nacelle-pylon/horizontal-tail WBNPT configuration, was chosen as a test bed representative of modern transport aircraft. The wing-body (WB) was used within this project. The objectives of this study were threefold: first, to produce a block-structured grid family; second, to complement the AIAA Drag Prediction Workshop results by assessing the performance of two turbulence modelling approaches; and third, to assess the behaviour of the steady RANS during off-design (high incidence/lift) transonic flight.

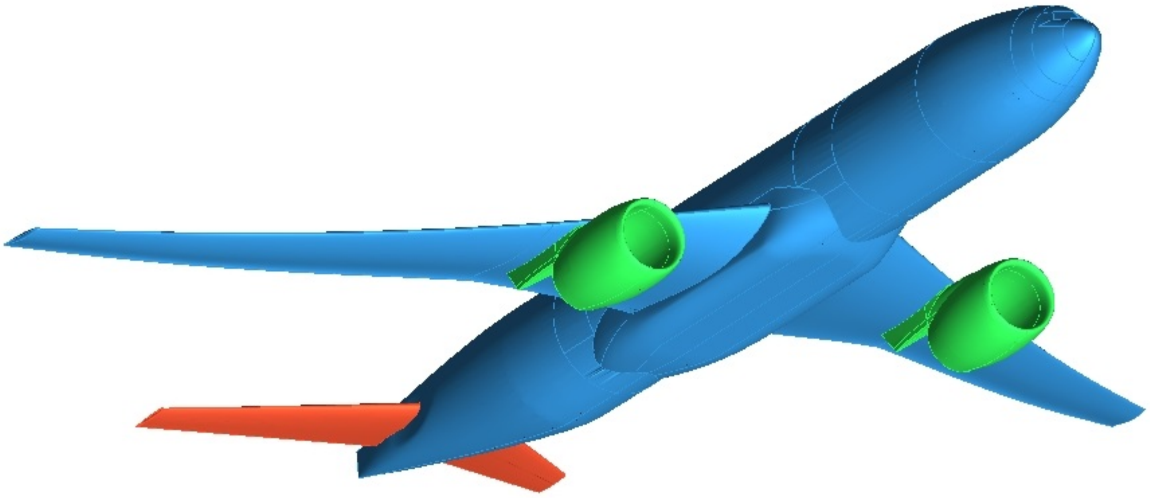

Fig. 7.3 The NASA CRM aircraft configuration: WBNPT

A three-level family of block-structured grids was built following the AIAA CFD Drag Prediction Workshop (DPW) guidelines. Producing structured grids around this configuration presented its own difficulties. First of all, the blocking-structure contained more than 200 blocks which were used to guide the distribution of elements on the surface and volume of the grid. Secondly, the geometry was found not to be watertight which resulted in difficulties in meshing the wing-fuselage junction, and the belly fairing geometry. Simulations at different incidences were performed on corresponding aeroelastically deformed CRM geometries available on the AIAA CFD DPW webpage. Grid deformations were produced manually herein by translating and rotating the blocks around the wing accordingly.

Two turbulence modelling approaches: Menter's $k-\omega$ *SST* [43] and a *Linear Pressure-Strain RSM* were assessed according to the 6^{th} AIAA DPW test cases. The *Stress-Omega RSM,* which was found to give superior accuracy in the 2D shock-buffet test case, was discarded as the CFD solver could not be converged when it was used. The aeroelastically deformed WB CRM was simulated at $M = 0.85$, chord $Re = 5$ million, and incidence (α) between 2.5 and 4°. A mesh-sensitivity study at fixed lift coefficient, C_L, of 0.5 was performed with the RSM only. A drag overprediction of up to 10 drag counts (1 drag count = 10^{-4} in drag coefficient) was observed due to overprediction of the viscous drag component. The turbulence model study revealed that at flight conditions closer to design point the SST outperformed the version of RSM used. In off-design flight, the SST simulations predicted an excessively large side-of-body separation. In literature, the side-of-body separation was attributed to the isotropic turbulence assumption which does not stand true in the case of corner flows present at the junction between the wing and the fuselage.

Thus, the *Linear-Pressure Strain RSM* turbulence closure was found more appropriate to investigate off-design transonic aerodynamics. The incidence was then further increased up to stall. The results revealed an overprediction of shock-induced separation development at incidences higher than 5°. This resulted in an early stall of the aircraft when compared to experiments.

In hindsight, it was later found that past 5° incidence, the aircraft is known to experience large amplitude shock fluctuations, thus a steady approach should not have been used. The fact that steady RANS simulations converged even in this flight conditions might reveal the way the code used was built to remain stable and produce results even in inappropriate scenarios.

7.3 Characterisation of shock-buffet on the NASA CRM

The wing-body NASA CRM was simulated in the unsteady shock-buffet regime. Previous experimental observations by Balakrishna and Acheson[30], Koike *et. al.* [33], and Sugioka *et. al.*[34] at $M_\infty = 0.85$, chord $Re_{mac} = 0.95$, 1.5, and 5.0 million determined shock-buffet onset with low amplitude pressure fluctuation at incidences higher than 3°; and large fluctuations at incidences higher than 5°. This study aimed to determine if URANS-based simulations could accurately capture the shock-buffet phenomenon, particularly the large amplitude fluctuations at high incidence.

A grid was produced based on the medium-sized grid generated for the study summarised in the section above. The URANS equations were closed with the *Speziale-Sarkar-Gatski / Launder-Reece-Rodi* (SSG/LRR-g)[70] RSM variant. The choice was based on lessons learnt from previous two studies as well as experience of research engineers at DLR. The SSG/LRR-g RSM was developed to tackle poor stability of the Stres-Omega RSM, whilst maintaining good accuracy of results by blending between the SSG and LRR models in the farfield and boundary layer area respectively. Thus, this variant of RSM was believed to be more robust and had previously produced accurate aerodynamic predictions in transonic flight.

Simulations were first computed at $Re_{mac} = 5$ million to assess the characteristics of the phenomenon on this aircraft. Surface data revealed high amplitude fluctuations occur at the shock location, resulting in a spanwise oscillation of the shock-front. This oscillation was visualised through buffet cells, a characteristic of shock-buffet that was observed also in experimental investigations. To further produce new insights into the shock-buffet phenomenon, the volume data was also analysed. Shock isosurfaces were extracted and used to determine the movement of the shock near and far from the wing surface. It was found that the observations made based on the surface oscillations were in good agreement with the movement of the shock in the volume.

Figure 7.4 shows shock-buffet dynamics on the NASA CRM. Flow field slices of density gradient reveal shock position and the presence of boundary layer separation. Surface contours of pressure coefficient reveal the waviness of the shock-front on the wing surface.

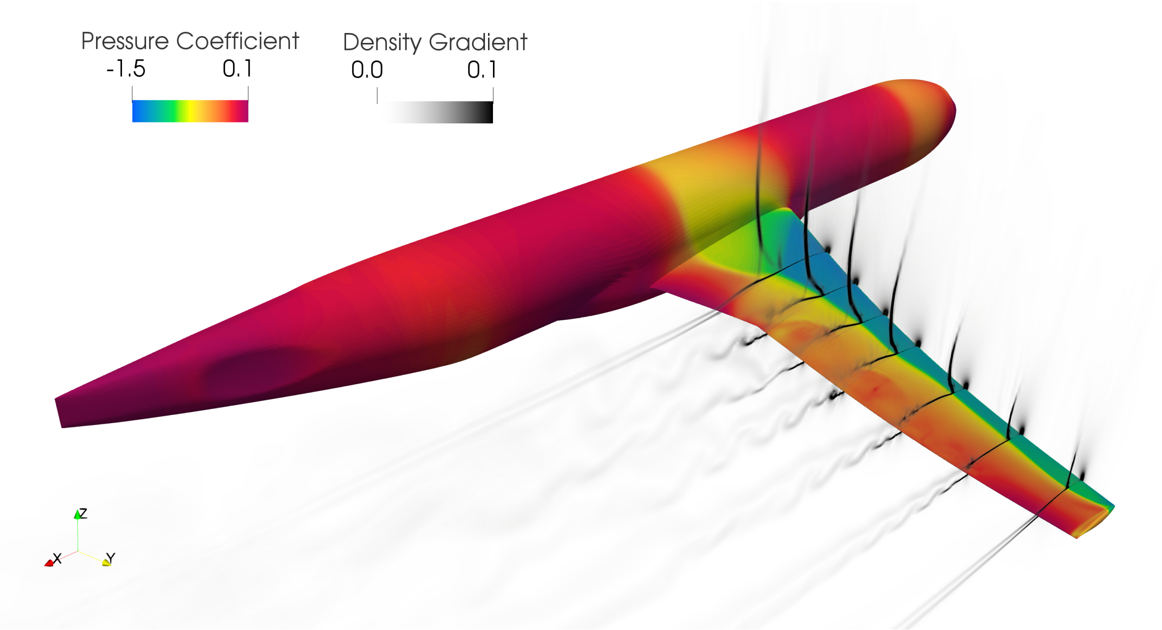

Fig. 7.4 Computed instantaneous flow field around the NASA CRM during shock-buffet. The surface contours give pressure coefficient; volume slices show density gradient values to highlight shock and boundary layer separation locations

Reynolds number effects on shock-buffet were analysed by reducing the value of Re_{mac} down to 1.5 and 0.95 million. The numerical study revealed that at lower Re, a shock displacement was present. This is undoubtedly attributed to thicker boundary layers which change the apparent shape of the wing to the freestream flow. At lower Re however, the shock fluctuations occurred over a larger extent of the wing's chord and span, resulting in higher fluctuations of the lift coefficient, a measure of the load on the wing.

7.4 Further work

It is worth noting here that all of the above required more resources (time and computational power) to be completed than initially expected.

One of the initial author's desire was to perform a fluid-structure interaction (FSI) assessment of shock-buffet. Unfortunately, this was not possible within the time frame of this project and remains possibly the main activity that should compliment the current work. An FSI study of shock-buffet would provide additional insight into the coupling of aerodynamic load fluctuation and structural properties of aircraft wings.

A second path that would be suitable for further investigations is the application of passive and/or active control strategies for shock buffet. Some brief research was already published into the application of shock bumps, vortex generators (VG) and air jet VGs to delay shock-induced separation and shock-buffet. None of those studies have completed this assessment on an industrially relevant configuration. Furthermore, different control strategies, including the use of control surfaces (e.g. ailerons, spoilers) as well as morphing wing technologies, could be analysed in the context of shock-buffet control.

It became clear towards the end of this project that although some early studies mentions the presence of a hysteresis in shock-buffet regime, no recent investigations were performed to verify this. If hysteresis is present, then shock-buffet onset cannot be defined any more as a precise incidence. Instead, aircraft manufactures must account for the direction from which the aircraft is approaching that incidence.

Finally, to somebody passionate about numerics, an interesting path would be investigatin the effect of numerical parameters on shock-buffet predictions. Throughout the current work, it was found that different numerical parameters, including discretization schemes, can have an impact on the stability, convergence and accuracy of the results. Different authors prefer different approaches which might not be applicable in all cases. A thorough investigation of this is highly recommended.

7.5 General lessons learnt

From an industrial perspective, accurate prediction of shock-buffet onset and evolution with incidence is critical. Not only should the aircraft manufacturers comply with authorities' requirements, but also guarantee a safe flight to all passengers and flight crew. When I first started this project, the literature regarding shock-buffet prediction using industrially-relevant simulation methods was limited and presented uncertain conclusions. URANS-based simulations and the use of eddy-viscosity turbulence models were not a certain approach for the problem at hand. The use of RSM was limited still due to increased cost, although the RSM could provide a turbulence modelling advantage. I decided that providing an insight into the use of RSM for shock-buffet prediction was an interesting research topic, with potential value for the industry.

2D simulations were straight-forward and the Stress-Omega variant of the RSM presented the advantage of not only qualitative but also good quantitative comparison with experimental data, however further investigation revealed that solver instabilities and grid sensitivity made this variant undesirable as robustness could not be guaranteed over a range of test cases. For the 3D test case, an advanced variant of the RSM, the SSG/LRR-g, that combines the advantages of the SSG and the LLR variants, whilst eliminating instabilities by using the $g = 1/\sqrt{\omega}$ equation instead of ω for the turbulence scale, was used. Numerical instabilities were eliminated, shock-buffet prediction compared well, qualitatively, with experimental observations. An underprediction of pressure fluctuation levels and inability to accurately predict small fluctuation shock-buffet onset incidence indicate a dissipative behaviour, the source of which could not be identified.

To conclude, it is my belief that shock-buffet can be predicted by means of URANS-based simulations closed with the full RSM, though the user of such methods should expect to be faced with difficulties associated with the use of RSM.

References

[1] A. Abbas-Bayoumi and K. Becker, “An industrial view on numerical simulation for aircraft aerodynamic design,” *Journal of Mathematics in Industry*, vol. 1, no. 1, pp. 1–14, 2011.

[2] E. N. Tinoco, O. P. Brodersen, S. Keye, K. R. Laflin, E. Feltrop, J. C. Vassberg, M. Mani, B. Rider, R. A. Wahls, J. H. Morrison, D. Hue, M. Gariepy, C. J. Roy, D. J. Mavriplis, and M. Murayama, “Summary of Data from the Sixth AIAA CFD Drag Prediction Workshop: CRM Cases 2 to 5,” *55th AIAA Aerospace Sciences Meeting*, pp. 1–43, 2017.

[3] Mario Asselin, *An Introduction to Aircraft Performance*. Reston: AIAA, 1997.

[4] A. Jameson, “Paul Garabedian ’ s Contributions to Transonic Airfoil and Wing Design,” in *Note of the Aerospace Computing Laboratory, Department of Aeronautics and Astronautics, Stanford University*, 2010.

[5] EASA, “Certification Specifications and Acceptable Means of Compliance for Large Aeroplanes,” Tech. Rep. November, 2018.

[6] USAF, “Flight Manual: Models U-2C and U-2F Aircraft,” tech. rep., USAF, 1967.

[7] A. R. G. Mundell and D. G. Mabey, “Pressure Fluctuations Caused by Transonic Shock/Boundary Layer Interaction,” *The Aeronautical Journal*, vol. 90, no. 897, pp. 274–282, 1986.

[8] H. H. Pearcey, J. Osborne, and H. A. B, “The Interaction Between Local Effects at the Shock and Rear Separation - A Source of Significant Scale Effects in Wind-Tunnel Tests on Aerofoils and Wings,” *AGARD*, vol. AGARD-CP-3, no. Transonic Aerodynamics, 1968.

[9] H. Tijdeman, “investigations of the transonic flow around oscillating airfoils,” tech. rep., NRL, 1977.

[10] F. Hilton and R. Fowler, “Photographs of Shock Wave Movement,” *National Physical Laboratories*, vol. R&M 2692, 1947.

[11] J. B. McDevitt, L. L. Levy Jr, and G. S. Deiwert, “Transonic flow about a thick circular-arc airfoil,” *AIAA Journal*, vol. 14, no. 5, pp. 606–613, 1976.

[12] L. L. Levy Jr., "Experimental and Computational Steady and Unsteady Transonic Flows about a Thick Airfoil," *AIAA Journal*, vol. 16, no. 6, pp. 564–572, 1978.

[13] H. L. Seegmiller and J. G. Marvin, "Steady and Unsteady Transonic Flow," *AIAA Journal*, vol. 16, no. 12, pp. 1262–1270, 1978.

[14] J. G. Marvin and H. L. Seegmiller, "Turbulence Modeling for Unsteady Transonic Flows," *AIAA Journal*, vol. 18, no. 5, pp. 489–496, 1980.

[15] D. G. Mabey, "Oscillatory Flows from Shock-Induced Separation on Biconvex Airfoils of Varying Thickness in Ventilated Wind Tunnels," tech. rep., AGARD, 1980.

[16] D. G. Mabey, B. L. Welsh, and B. E. Cripps, "Periodic Flows on a Rigid 14% Thick Biconvex Wing at Transonic Speeds," tech. rep., Royal Aircraft Establishment, 1981.

[17] J. Gibb, "The Cause and Cure of Periodic Flows at Transonic Speeds," in *Proceedings of the 16th Congress of the International Council of the Aeronautical Sciences*, 1988.

[18] F. W. Roos, M. D. Corporation, and S. Louis, "Some Features of the Unsteady Pressure Field in Transonic Airfoil Buffeting," *Journal of Aircraft*, vol. 17, no. 11, 1980.

[19] B. H. K. Lee and L. H. Ohman, "Unsteady Pressures and Forces During Transonic Buffeting of a Supercritical Airfoil," *Journal of Aircraft*, no. June, 1984.

[20] B. H. K. Lee, F. A. Ellis, and J. Bureau, "Investigation of the Buffet Characteristics of Two Supercritical Airfoils," *Journal of Aircraft*, vol. 26, no. 8, 1989.

[21] B. H. K. LEE, "Oscillatory shock motion caused by transonic shock boundary-layer interaction," *AIAA Journal*, vol. 28, no. 5, pp. 942–944, 1990.

[22] A. Feldhusen-Hoffmann, V. Statnikov, M. Klaas, and W. Schröder, "Investigation of shock–acoustic-wave interaction in transonic flow," *Experiments in Fluids*, vol. 59, no. 1, pp. 1–13, 2018.

[23] L. Jacquin, P. Molton, S. Deck, B. Maury, and D. Soulevant, "Experimental Study of Shock Oscillation over a Transonic Supercritical Profile," *AIAA Journal*, vol. 47, no. 9, pp. 1985–1994, 2009.

[24] F. ROOS, "The buffeting pressure field of a high-aspect-ratio swept wing," *18th Fluid Dynamics and Plasmadynamics and Lasers Conference*, 1985.

[25] J. Dandois, "Experimental study of transonic buffet phenomenon on a 3D swept wing," *Physics of Fluids*, vol. 28, no. 1, 2016.

[26] P. Molton, J. Dandois, A. Lepage, V. Brunet, and R. Bur, "Control of Buffet Phenomenon on a Transonic Swept Wing," *AIAA Journal*, vol. 51, no. 4, pp. 761–772, 2013.

[27] J. Dandois, P. Molton, A. Lepage, A. Geeraert, V. Brunet, J.-B. Dor, and E. Coustols, "Buffet Characterization and Control for Turbulent Wings," *AerospaceLab*, no. 6, pp. 1–17, 2013.

[28] S. Lawson, D. Greenwell, and M. K. Quinn, “Characterisation of Buffet on a Civil Aircraft Wing,” in *54th AIAA Aerospace Sciences Meeting*, no. January, pp. 1–19, 2016.

[29] L. Masini, S. Timme, A. Ciarella, and A. Peace, “Influence of vane vortex generators on transonic wing buffet: futher analysis of the BUCOLIC experimental dataset,” in *52nd 3AF International Conference on Applied Aerodynamics*, (Lyon), La Societe Savante de L’ Aeronautique et de l’Espace, 2017.

[30] S. Balakrishna and M. Acheson, “Analysis of NASA Common Research Model Dynamic Data,” in *49th AIAA Aerospace Sciences Meeting*, no. AIAA 2011-1127, AIAA, 2011.

[31] T. Lutz, P. P. Gansel, A. Waldmann, D.-M. Zimmermann, and S. Schulte am Hülse, “Prediction and Measurement of the Common Research Model Wake at Stall Conditions,” *Journal of Aircraft*, vol. 53, no. 2, pp. 501–514, 2016.

[32] Y. Sugioka, K. Nakakita, and K. Asai, “Non-Intrusive Unsteady Psp Technique for Investigayion of Transonic Buffeting,” *30th congress of the International Concil of the Aeronautical Sciences*, 2016.

[33] S. Koike, M. Ueno, K. Nakakita, and A. Hashimoto, “Unsteady Pressure Measurement of Transonic Buffet on NASA Common Research Model,” in *34th AIAA Applied Aerodynamics Conference*, no. June, pp. 1–25, 2016.

[34] Y. Sugioka, S. Koike, K. Nakakita, D. Numata, T. Nonomura, and K. Asai, “Experimental analysis of transonic buffet on a 3D swept wing using fast-response pressure-sensitive paint,” *Experiments in Fluids*, vol. 59, no. 6, p. 108, 2018.

[35] M. Iovnovich and D. E. Raveh, “Numerical Study of Shock Buffet on Three-Dimensional Wings,” *AIAA Journal*, vol. 53, no. 2, pp. 449–463, 2015.

[36] E. Paladini, J. Dandois, D. Sipp, and J.-C. Robinet, “Analysis and Comparison of Transonic Buffet Phenomenon over Several Three-Dimensional Wings,” *AIAA Journal*, vol. 57, no. 1, pp. 379–396, 2019.

[37] V. Brunet, “Computational Study of Buffet Phenomenon,” in *21st AIAA Applied Aerodynamics Conference, Fluid Dynamics and Co-located Conferences*, (Orlando), AIAA, 2003.

[38] V. Brunet, S. Deck, P. Molton, and M. Thiery, “A complete Experimental and Numerical Study of the Buffet Phenomenon over the OAT15A Airfoil,” in *40ème Colloque Aérodynamique Appliquée*, no. March, (Toulouse), 2005.

[39] T.-H. Shih, J. Zhu, and J. L. Lumley, “A New Reynolds Equation Model Stress Algebraic,” Tech. Rep. August, 1994.

[40] M. Thiery and E. Coustols, “URANS computations of shock-induced oscillations over 2D rigid airfoils: Influence of test section geometry,” *Flow, Turbulence and Combustion*, vol. 74, no. 4, pp. 331–354, 2005.

[41] M. Thiery and E. Coustols, “Numerical prediction of shock induced oscillations over a 2D airfoil: Influence of turbulence modelling and test section walls,” *International Journal of Heat and Fluid Flow*, vol. 27, pp. 661–670, aug 2006.

[42] P. R. Spalart, W. H. Jou, M. K. Strelets, and S. R. Allmaras, “Comments on the feasibility of LES for wings and on a hybrid RANS/LES approach,” *Advances in DNS/LES*, vol. 1, no. JANUARY, pp. 4–8, 1997.

[43] F. R. Menter, “Two-equation eddy-viscosity turbulence models for engineering applications,” *AIAA Journal*, vol. 32, no. 8, pp. 1598–1605, 1994.

[44] T. Darris and H. Bezart, “Four-equations models for Reynolds stress and turbulent heat flux predictions,” in *Proceedings, 12th International Heat Transfer Conference*, (Grenole, France), 2002.

[45] S. Deck, “Numerical simulation of transonic buffet over an airfoil,” *AIAA journal*, vol. 43, no. 7, pp. 1556–1566, 2005.

[46] F. Grossi, M. Braza, and Y. Hoarau, “Prediction of Transonic Buffet by Delayed Detached-Eddy Simulation,” *AIAA Journal*, vol. 52, no. 10, pp. 2300–2312, 2014.

[47] J. B. Huang, Z. X. Xiao, J. Liu, and S. Fu, “Simulation of shock wave buffet and its suppression on an OAT15A supercritical airfoil by IDDES,” *Science China: Physics, Mechanics and Astronomy*, vol. 55, no. 2, pp. 260–271, 2012.

[48] M. L. Shur, P. R. Spalart, M. K. Strelets, and A. K. Travin, “A hybrid RANS-LES approach with delayed-DES and wall-modelled LES capabilities,” *International Journal of Heat and Fluid Flow*, vol. 29, no. 6, pp. 1638–1649, 2008.

[49] D. Szubert, F. Grossi, A. Jimenez Garcia, Y. Hoarau, J. C. Hunt, and M. Braza, “Shock-vortex shear-layer interaction in the transonic flow around a supercritical airfoil at high Reynolds number in buffet conditions,” *Journal of Fluids and Structures*, vol. 55, pp. 276–302, 2015.

[50] Y. Fukushima and S. Kawai, “Wall-Modeled Large-Eddy Simulation of Transonic Airfoil Buffet at High Reynolds Number,” *AIAA Journal*, vol. 56, no. 6, pp. 2372–2388, 2018.

[51] F. Grossi, *Physics and modeling of unsteady shock wave / boundary layer interactions over transonic airfoils by numerical simulation.* Phd thesis, Universite de Toulouse, 2014.

[52] N. F. Giannelis, O. Levinski, and G. A. Vio, “Influence of Mach number and angle of attack on the two-dimensional transonic buffet phenomenon,” *Aerospace Science and Technology*, vol. 78, pp. 89–101, 2018.

[53] M. Zauner, N. De Tullio, and N. D. Sandham, “Direct Numerical Simulations of Transonic Flow Around an Airfoil at Moderate Reynolds Numbers,” *AIAA Journal*, vol. 57, no. 2, pp. 597–607, 2019.

[54] J. R. Edwards and S. Chandra, "Comparison of eddy viscosity-transport turbulence models for three-dimensional, shock-separated flowfields," *AIAA Journal*, vol. 34, no. 4, pp. 756–763, 1996.

[55] F. Sartor and S. Timme, "Reynolds-Averaged Navier-Stokes Simulations of Shock Buffet on Half Wing-Body Configuration," in *53rd AIAA Aerospace Sciences Meeting*, (Kissimmee, Florida), AIAA, 2015.

[56] F. Sartor and S. Timme, "Mach number effects on buffeting flow on a half wing-body configuration," *International Journal of Numerical Methods for Heat & Fluid Flow*, vol. 26, no. 7, pp. 2066–2080, 2016.

[57] F. Sartor and S. Timme, "Delayed Detached–Eddy Simulation of Shock Buffet on Half Wing–Body Configuration," *AIAA Journal*, vol. 55, no. 4, pp. 1230–1240, 2017.

[58] L. Masini, S. Timme, and A. J. Peace, "Reynolds Number Effects on Wing Shock Buffet Unsteadiness," *AIAA Aviation 2019 Forum*, no. June, 2019.

[59] T. Ishida, A. Hashimoto, Y. Ohmichi, T. Aoyama, and K. Takekawa, "Transonic Buffet Simulation over NASA-CRM by Unsteady-FaSTAR Code," in *55th AIAA Aerospace Sciences Meeting*, no. January, pp. 1–12, 2017.

[60] A. Hashimoto, T. Ishida, T. Aoyama, Y. Ohmichi, T. Yamamoto, and K. Hayashi, "Current Progress in Unsteady Transonic Buffet Simulation with Unstructured Grid CFD Code," in *2018 AIAA Aerospace Sciences Meeting*, no. January, pp. 1–14, 2018.

[61] Y. Ohmichi, T. Ishida, and A. Hashimoto, "Modal Decomposition Analysis of Three-Dimensional Transonic Buffet Phenomenon on a Swept Wing," *AIAA Journal*, vol. 56, pp. 3938–3950, aug 2018.

[62] S. Timme, "Global Shock Buffet Instability on NASA Common Research Model," *AIAA Scitech 2019 Forum*, no. January, 2019.

[63] J. D. Crouch, A. Garbaruk, and D. Magidov, "Predicting the onset of flow unsteadiness based on global instability," *Journal of Computational Physics*, vol. 224, no. 2, pp. 924–940, 2007.

[64] B. H. Lee, "Self-sustained shock oscillations on airfoils at transonic speeds," *Progress in Aerospace Sciences*, vol. 37, no. 2, pp. 147–196, 2001.

[65] N. F. Giannelis, G. A. Vio, and O. Levinski, "A review of recent developments in the understanding of transonic shock buffet," *Progress in Aerospace Sciences*, vol. 92, pp. 39–84, 2017.

[66] DLR, "Technical Documentation of the DLR TAU-Code Release 2013.2.0," tech. rep., Institute of Aerodynamics and Flow Technology, DLR, Braunschweig, 2013.

[67] O. Reynolds, "On the Dynamical Theory of Incompressible Viscous Fluids and the Determination of the Criterion," *Philosophical Transactions of the Royal Society A: Mathematical, Physical and Engineering Sciences*, vol. 186, 1895.

[68] J. Boussinesq, “Theorie de l’ecoulement tourbillant,” *Mem. Presentes par Divers Savants Acad. Sci Inst. Fr*, vol. 23, 1877.

[69] B. Eisfeld, “Implementation of Reynolds stress models into the DLR-FLOWer code,” Tech. Rep. 0, Institute of Aerodynamics and Flow Technology, 2004.

[70] V. Togiti and B. Eisfeld, “Assessment of g -Equation Formulation for a Second-Moment Reynolds Stress Turbulence Model,” in *22nd AIAA Computational FLuid Dynamics Conference*, no. June, (Dallas), pp. 1–18, AIAA, 2015.

[71] B. Launder, G. Reece, and W. Rodi, “Progress in the Development of a Reynolds Stress Turbulence Closure,” *J. Fluid Mechanics*, vol. 68, pp. 537–566, 1975.

[72] C. G. Speziale, S. Sarkar, and T. B. Gatski, “Modeling the Pressure-Strain Correlation of Turbulence - an Invariant Dynamical Systems Approach,” *Journal of Fluid Mechanics1*, vol. 227, pp. 245–272, 1991.

[73] B. E. Launder, “Second-moment closure and its use in modelling turbulent industrial flows,” 1989.

[74] B. E. Launder, “Second-moment closure: present... and future?,” *International Journal of Heat and Fluid Flow*, vol. 10, no. 4, pp. 282–300, 1989.

[75] D. C. Wilcox, *Turbulence Modeling for CFD,*. La Canada CA: DCW Industries, Inc., 3rd editio ed., 2006.

[76] I. ANSYS, “FLUENT,” 2017.

[77] D. Schwamborn, T. Gerhold, and R. Heinrich, “The DLR-TAU-code: Recent Applications in Research and Industry,” in *ECCOMAS CFD*, (Delft), ECCOMAS, 2006.

[78] S. Illi, T. Lutz, and E. Krämer, “On the capability of unsteady RANS to predict transonic buffet,” in *Third Symposium Simulation of Wing and Nacelle Stall*, no. June, (Braunschweig), pp. 1–13, 2012.

[79] S. Jakirlic and K. Hanjalic, “A new approach to modelling near-wall turbulence energy and stress dissipation,” *Journal of Fluid Mechanics*, vol. 459, pp. 139–166, 2002.

[80] J. C. Vassberg, M. A. DeHaan, M. Rivers, and Richard A. Wahls, “Development of a Common Research Model for Applied CFD Validation Studies,” in *AIAA Paper*, pp. 1–22, 2008.

[81] J. Vassberg and E. M. Lee-Rausch, “Drag Prediction Workshop,” *Journal of Aircraft*, vol. 51, no. 4, pp. 1069–1331, 2014.

[82] J. Vassberg and E. M. Lee-Rausch, “Special Section on Sixth AIAA CFD Drag Prediction Workshop,” *Journal of Aircraft*, vol. 55, no. 4, pp. 1317–1509, 2018.

[83] J. C. Vassberg and Et.al, “Summary of the Fourth AIAA CFD Drag Prediction Workshop,” *AIAA Paper*, no. July, p. 4547, 2010.

[84] D. W. Levy, K. R. Laflin, E. N. Tinoco, J. C. Vassberg, M. Mani, B. Rider, C. L. Rumsey, R. A. Wahls, J. H. Morrison, O. P. Brodersen, S. Crippa, D. J. Mavriplis, and M. Murayama, “Summary of Data from the Fifth Computational Fluid Dynamics Drag Prediction Workshop,” *Journal of Aircraft*, vol. 51, no. 4, pp. 1194–1213, 2014.

[85] S. Keye, O. Brodersen, and M. B. Rivers, “Investigation of Aeroelastic Effects on the NASA Common Research Model,” *Journal of Aircraft*, vol. 51, no. 4, pp. 1323–1330, 2014.

[86] S. Keye and M. Gammon, “Development of Deformed CAD Geometries of NASA’s Common Research Model for the Sixth AIAA CFD Drag Prediction Workshop,” *Journal of Aircraft*, vol. 55, no. 4, pp. 1401–1405, 2018.

[87] M. Rivers, C. Hunter, and R. Campbell, “Further Investigation of the Support System Effects and Wing Twist on the NASA Common Research Model,” *30th AIAA Applied Aerodynamics Conference*, no. June, 2012.

[88] M. B. Rivers and A. Dittberner, “Experimental Investigations of the NASA Common Research Model in the NASA Langley National Transonic Facility and NASA Ames 11-Ft Transonic Wind Tunnel,” in *49th AIAA*, (Orlando), AIAA, 2011.

[89] V. Togiti, B. Eisfeld, and O. Brodersen, “Turbulence model study for the flow around the NASA common research model,” *Journal of Aircraft*, vol. 51, no. 4, pp. 1331–1343, 2014.

[90] J. Chen, Y. Zhang, H. Zhao, and G. Zhou, “Numerical Investigations of the NASA Common Research Model with Aeroelastic Twist,” *Journal of Aircraft*, no. May, pp. 1–13, 2017.

[91] J. Dandois, “Improvement of Corner Flow Prediction Using the Quadratic Constitutive Relation,” *AIAA Journal*, vol. 52, no. 12, pp. 2795–2806, 2014.

[92] M. Meinel and G. Einarsson, “The FlowSimulator framework for massively parallel CFD applications,” in *PARA 2010 conference: state of the art in Scientific and Parallel Computing*, (Reykjavik), 2010.

[93] D. Lovely and R. Haimes, “Shock detection from computational fluid dynamics results,” in *14th Computational Fluid Dynamics Conference*, (Norfolk), pp. 1–9, AIAA, 1999.

[94] Z. Wu, Y. Xu, W. Wang, and R. Hu, “Review of shock wave detection method in CFD post-processing,” *Chinese Journal of Aeronautics*, vol. 26, no. 3, pp. 501–513, 2013.